TWIST IN CORONAL MAGNETIC FIELDS

by

Anna Viktorovna Malanushenko

A dissertation submitted in partial fulfillment
of the requirements for the degree

of

Doctor of Philosophy

in

Physics

MONTANA STATE UNIVERSITY
Bozeman, Montana

May 2010

APPROVAL

of a dissertation submitted by

Anna Viktorovna Malanushenko

This dissertation has been read by each member of the dissertation committee and has been found to be satisfactory regarding content, English usage, format, citations, bibliographic style, and consistency, and is ready for submission to the Division of Graduate Education.

Dr. Dana Longcope

Approved for the Department of Physics

Dr. Richard J. Smith

Approved for the Division of Graduate Education

Dr. Carl A. Fox

STATEMENT OF PERMISSION TO USE

Anna Viktorovna Malanushenko

May, 2010

To Dad and Mom.
Your example has shown me the way.
Your encouragement has supported me along it.

ACKNOWLEDGEMENTS

I would like to thank my adviser, Dana Longcope, for teaching me physics and how to do research, for guiding me, for helping me, for making me see the big picture and teaching how to set up the goals. For knowing everything about everything. For showing me what a scientist ought to be with his own personal example. Thank you, Dana. I want to be like you one day.

I am grateful to all professors in the Physics department for valuable consultations and discussions. In particular, to Dave McKenzie for our weekly meetings on the project and for teaching me to work with raw data, and to Charles Kankelborg for proof-reading my projects and correcting my English.

Andrés. Thank you for your love, care and support that helped me along the way. For all the discussions on physics and programming that we had. And for teaching me English.

TABLE OF CONTENTS

TABLE OF CONTENTS – CONTINUED

LIST OF TABLES

LIST OF FIGURES

Figure Page

LIST OF FIGURES – CONTINUED

LIST OF FIGURES – CONTINUED

LIST OF FIGURES – CONTINUED

LIST OF FIGURES – CONTINUED

LIST OF FIGURES – CONTINUED

LIST OF FIGURES – CONTINUED

LIST OF FIGURES – CONTINUED

LIST OF FIGURES – CONTINUED

LIST OF FIGURES – CONTINUED

LIST OF FIGURES – CONTINUED

LIST OF FIGURES – CONTINUED

LIST OF FIGURES – CONTINUED

ABSTRACT

Twist of magnetic field is believed to play important role in driving instabilities that result in eruptive events on the Sun. This thesis provides different methods to measure twist in the solar corona.

First, given a model of coronal field, twist of a magnetic domain (i.e., a volume that contains all field lines connecting two regions of interest in the photosphere) is well studied for cases when the domain is a thin cylinder. For cases when such approximation is inapplicable a generalization of twist can be derived from a quantity called additive self-helicity. I develop explicit numerical methods to compute generalized twist. I also demonstrate that such a quantity sets a threshold on kink instability like the traditional twist does for thin cylinders.

In a more realistic scenario, coronal magnetic field is not known and so neither is its helicity. There are two principal methods to overcome this problem. The first is to integrate helicity flux across the photosphere (as helicity is believed to be approximately conserved in the corona) using magnetic field on Sun's surface. There is little published evidence as yet that coronal helicity indeed corresponds to its integrated photospheric flux. The second is to extrapolate the coronal magnetic field using surface measurements as boundary conditions and use this extrapolation for helicity computation; for fields with complicated structure such extrapolations are extremely challenging and suffer from major drawbacks.

I develop a method to estimate twist of coronal fields without attempting complicated extrapolations or studying helicity flux. The method builds a simple uniformly-twisted magnetic field and adjusts its properties until there is one line in this field that matches one coronal loop; this is repeated for all evident coronal loops resulting in twist measurements for each individual loop.

I use this method to demonstrate that the rate of change of twist in the solar corona is indeed approximately equal to the one derived from photospheric helicity flux.

The results of this dissertation are useful for better understanding of magnetic topology in general. They are also extremely promising for extrapolating coronal magnetic fields. Measurements of coronal twist might aid in predicting magnetic instabilities.

1. INTRODUCTION

1.1. Magnetic Field Lines and Their Properties

Non-relativistic and non-resistive plasma.

Magnetic tension. Frozen-in conditions.

A magnetic field line (hereafter a “field line”) $\mathbf{r}(b)$ of a field $\mathbf{B}$ is a solution of

$$\frac{d\mathbf{r}}{db} = \frac{\mathbf{B}}{B}, \tag{1.1}$$

obtained by integration in b in both directions from a given starting point $\mathbf{r}_0$. Equation (1.1) has a unique solution except for the points in which $\mathbf{B} = 0$ or $\mathbf{B} \to \infty$. As

$$\nabla \cdot \mathbf{B} = 0, \tag{1.2}$$

the field lines are curves, that have no starting or ending points (except at points where $\mathbf{B} = 0$ of $\mathbf{B} \to \infty$) and that with the same exception they do not cross.

When a magnetic field is present in plasma, field lines have a few more properties, relevant to this dissertation work.

I will further only consider a *non-relativistic* and *non-resistive* plasma. The first means that plasma velocity $|\mathbf{v}| \ll c$ and so Ampere’s law could be simplified to

$$\mathbf{J} = \frac{c^2}{4\pi} \nabla \times \mathbf{B} \tag{1.3}$$

in CGS-ESU system of units [Jackson, 1975].

When a plasma moves at a velocity $\mathbf{v}$ in electric field $\mathbf{E}$ and magnetic field $\mathbf{B}$, the electric field it experiences in its own rest frame is

$$\mathbf{E}' = \mathbf{E} + \mathbf{v} \times \mathbf{B}. \tag{1.4}$$

Ohm's law, $\mathbf{J} = \sigma \mathbf{E}'$, allows us to express $\mathbf{E}$ through $\mathbf{B}$ and $\mathbf{J}$ in the *induction equation.* The latter could be simplified using Equations (1.3) and (1.2) and vector identities:

$$\frac{\partial \mathbf{B}}{\partial t} = -\nabla \times \mathbf{E} = \nabla \times (\mathbf{v} \times \mathbf{B}) - \frac{c^2}{4\pi\sigma} \nabla^2 \mathbf{B}, \tag{1.5}$$

where the first term describes convection and the second one describes diffusion with a diffusivity coefficient $\eta = c^2/4\pi\sigma$. The *non-resistive* approximation means that the conductivity σ is so high that the second term in Equation (1.5) can be neglected, i.e., the diffusivity $\eta \ll Lv$, where L is a typical length scale of the problem and v is a typical velocity. This is more commonly viewed by introducing a “magnetic Reynolds number”: $R_m = Lv/\eta$. $R_m \gg 1$ for most astrophysical plasmas. In particular, for solar corona $R_m \approx 10^8 - 10^{12}$ [Aschwanden, 2006].

In general, when a field line is curved, there is a restoring force, that tries to straighten it. This restoring force is similar to the *tension force* in elastic strings. Indeed, the plasma is subject to Lorentz force:

$$\mathbf{F}_L = \mathbf{J} \times \mathbf{B} = \frac{1}{4\pi} (\nabla \times \mathbf{B}) \times \mathbf{B}. \tag{1.6}$$

From basic vector identities it follows that

$$\mathbf{F}_L = -\frac{1}{8\pi} \nabla B^2 + \frac{1}{4\pi} (\mathbf{B} \cdot \nabla) \mathbf{B}. \tag{1.7}$$

Here the first term is a magnetic pressure term that acts in all directions. Let us take a closer look at the second term, representing $\mathbf{B}$ as $\mathbf{B} = B(b)\hat{\mathbf{b}}(b)$, where $|\hat{\mathbf{b}}| = 1$ and b is a natural parameter along a field line. Note that in these terms $B_x = Bdx/db$. Then, using Equation (1.1),

$$\begin{aligned} \frac{1}{4\pi}(\mathbf{B}\cdot\nabla)\mathbf{B} &= \frac{1}{4\pi}B\frac{d\mathbf{B}}{db} = \frac{1}{4\pi}B\hat{\mathbf{b}}\frac{dB}{db} + \frac{1}{4\pi}B^2\frac{d\hat{\mathbf{b}}}{db} \\ &= \frac{1}{8\pi}\hat{\mathbf{b}}\frac{dB^2}{db} + \frac{1}{4\pi}B^2\frac{d\hat{\mathbf{b}}}{db}. \end{aligned} \tag{1.8}$$

The first term in Equation (1.8) cancels out the magnetic pressure term from Equation (1.7) in $\hat{\mathbf{b}}$ direction[1]. The second term is exactly $\frac{1}{4\pi}B^2\mathbf{k}$, where $\mathbf{k}$ is a curvature vector, as it is commonly defined in analytic geometry; its length is equal to inverse of the curvature radius $1/R$ and it is directed towards the center of the curvature. Plugging the result of Equation (1.8) to Equation (1.7), we get

$$\mathbf{F}_L = -\frac{1}{8\pi}\nabla_\perp B^2 + \frac{1}{4\pi}B^2\mathbf{k}. \tag{1.9}$$

That means, the Lorentz force exerts magnetic pressure in directions perpendicular to $\mathbf{B}$ and a magnetic "tension" in the direction towards local curvature center.

Another important property of field lines in a non-resistive plasma are the *frozen-in conditions*, that relate the motions of plasma to the changes in magnetic field. The first part of this is that plasma moves along with field lines: if two elements of the plasma are on the same field line, they will stay on the same field line forever. The second is the conservation of magnetic flux: if plasma elements forming a curve C_1

---

[1] To see this, it is enough to introduce two more unit vectors $\hat{\mathbf{u}}$ and $\hat{\mathbf{v}}$ to make a orthonormal set with $\hat{\mathbf{b}}$ and express ∇B^2 in these coordinates.

have evolved and at later time form a curve C_2, the magnetic flux through both curves is the same. These are the basic results of low-resistive plasma physics, covered in most textbooks, e.g., [Aschwanden, 2006, Choudhuri, 1998, Priest & Forbes, 2000].

1.2. Coronal Loops

Flux tubes in the solar corona. Low-β plasma.

Importance of Lorentz force. Moving footpoints.

The frozen-in condition allows us to introduce an entity called *magnetic flux tube*, typically viewed as a tube-like volume, occupied by a bundle of field lines initiated within a closed contour. A common object of study is a *thin flux tube*, that has a well-defined axis and that has a diameter much smaller than all other length scales in the system (such as tube's length, curvature radius and so on). The magnitude of magnetic field and the tube's width could vary along the flux tube. However, as magnetic flux across the "walls" of the tube is zero, the magnetic flux along the axis of the tube should be constant, so that for any arbitrary subsection of the tube the total magnetic flux across the surface of the subsection is zero, as demanded by Equation (1.2).

Because of the frozen-in condition, an ideal plasma cannot leave or enter a flux tube, but can only move along it. It is also recognized that magnetized plasma has a highly anisotropic thermal conductivity: along the magnetic field it is many orders of magnitude higher than across the field [Ireland et al., 1992]; the reason for that is the difference in the mean free path of particles along and across the field lines. So a localized heating event effectively heats the entire flux tube it is embedded in, but not its surroundings. Observations of solar corona in Soft X-Ray (SXR) and Extreme Ultraviolet (EUV) indeed reveal thin emitting strands, called *coronal loops* (see Figure 1).

The above mentioned properties allow to address coronal loops in many senses as distinct isolated structures [Rosner et al., 1978].

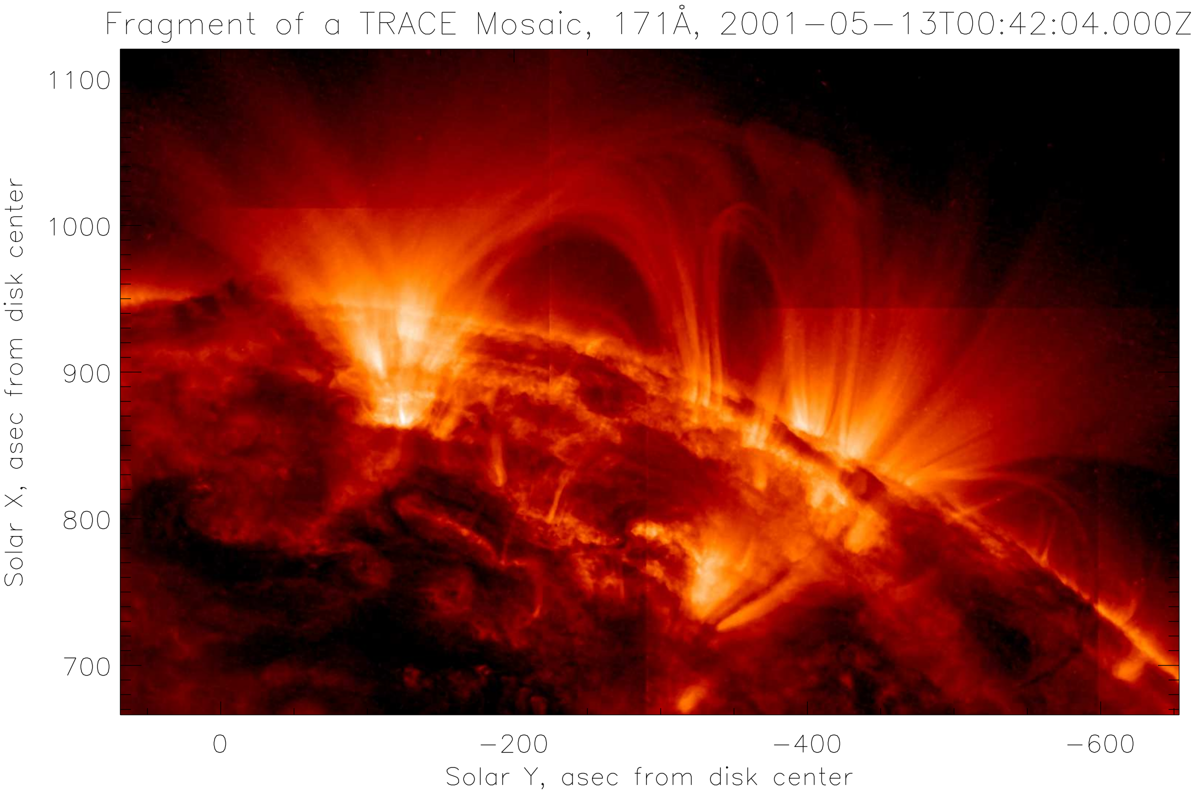

Figure 1. Coronal loops, as seen in Extreme Ultraviolet (EUV) by TRACE [Handy et al., 1999].

Within this thesis I will consider flux tubes, that are in equilibrium, that is, the total force acting on them is zero. The latter is in general a sum of gravity force, pressure gradient force, Lorentz force and viscosity force:

$$\mathbf{F}_{tot} = -\nabla p + \frac{1}{4\pi}(\nabla \times \mathbf{B}) \times \mathbf{B} + \rho g + \rho\nu\nabla^2\mathbf{v}. \tag{1.10}$$

If loops are not moving, the viscosity term vanishes. It also turns out that in the quiescent solar corona the gas pressure and the gravity terms are negligibly small compared to the Lorentz force term. The ratio of pressure force to the magnetic pressure is commonly referred as plasma β:

$$\beta = \frac{p/L}{B^2/8\pi L} = 8\pi\frac{p}{B^2}. \tag{1.11}$$

In solar corona, for at least up to the heights of $\sim$ 100Mm, $\beta \ll 1$ [Gary, 2001] and the magnetic pressure dominates over the gas pressure. Now, the ratio of the pressure force to the gravity force could be obtained using the fact that $p = k_B T\rho/\mu$ (where μ is a mean particle mass, for solar corona $\mu \approx 1.27m_H$ [Aschwanden, 2006]) and introducing the pressure scale height $H = k_B T\mu g$:

$$\frac{\nabla p}{\rho g} \propto \frac{p}{L\rho g} = \frac{H}{L}, \tag{1.12}$$

where L is a typical length scale of the system. Pressure scale height is a function of temperature, and for temperatures typically found in the corona, $H \propto 100$Mm [Aschwanden, 2006]. So in low-β plasma for loops of height $L \leq H$ the gravity term in Equation (1.10) could be neglected along with the pressure term.

Summarizing the aforementioned, coronal loops are in equilibrium if the Lorentz force vanishes. Of course, $\mathbf{F}_L = 0$ does *not* mean that both terms in Equation (1.9) vanish. In general it means that the magnetic pressure balances the magnetic tension.

In particular, magnetic tension could be expected to be larger in flux tubes in which field lines have in some sense stronger "bend", or smaller curvature radius, e.g., *twisted* and *entangled* flux tubes. They become so due to the plasma motions in the photosphere they are "anchored" to. While in rarefied low-β corona magnetic field drives the plasma motion, the opposite happens in the dense high-β photosphere and Sun's interior. Plasma flows that take place in the photosphere move around and spin the footpoints of coronal flux tubes. In the non-resistive corona flux tubes cannot cross or penetrate into each other, so a few tubes might become entangled due to braiding motions or an isolated tube might develop inner twist due to spinning motions. If such motions happen sufficiently slowly, flux tubes might relax to a new equilibrium state, in which magnetic pressure would again balance magnetic tension. An obvious question to ask is whether such equilibrium would be stable. Apparently, in certain cases it would definitely be *un*stable. I will further concentrate on only one scenario, the so-called *kink instability.*

1.3. Kink Instability in Thin Flux Tubes

Twisted flux tubes. Kink instability.

Practical applications.

Kink instability is typically described in flux tubes that carry *twisted* magnetic field, that is, which has a non-zero azimuthal component[2]. A classical example of such is a straight uniformly twisted and axially symmetric flux tube [Aschwanden, 2006, Gold & Hoyle, 1960], with the field

$$\mathbf{B} = B_z(\rho)\hat{\mathbf{z}} + B_\varphi(\rho)\hat{\boldsymbol{\varphi}}, \tag{1.13}$$

where $B_z = B_0/(1 + b^2\rho^2)$, $B_\varphi = b\rho B_z$ and $b = const = 2\pi Tw/L$ (note that this b is different from the arc-length used before). It could be easily verified that for such field $\mathbf{F}_L = (\nabla \times \mathbf{B}) \times \mathbf{B} = 0$ and thus the field is in equilibrium. Its field lines are described by equation

$$\varphi(z) = bz = 2\pi Tw\frac{z}{L} \tag{1.14}$$

and make Tw full revolutions about the axis[3] per length L. For a finite cylinder of length L the quantity

$$\Psi = bL = 2\pi Tw \tag{1.15}$$

has the meaning of total twist angle the field lines make about the axis.

---

[2] In the sense of it being perpendicular to the axis of the tube.

[3] Note that Tw is not in general a natural number.

As was shown in [Hood & Priest, 1979], such equilibrium is unstable to the $m = \pm 1$ mode in the normal mode decomposition of the displacement

$$\boldsymbol{\xi} = Re\left[(\xi_\rho, \xi_\varphi, \xi_z)e^{i(m\phi+kz)}\right] \tag{1.16}$$

(Figure 2), known as *kink mode*, if $\Psi = 2\pi Tw \geq \Psi_{crit}$. [Hood & Priest, 1979] estimated

$$\Psi_{crit} \simeq 3.3\pi \tag{1.17}$$

for a thin[4] uniformly twisted flux tube. This result was obtained by minimizing the energy perturbation with respect to $\boldsymbol{\xi}$ and performing a numerical integration of the resulting Euler-Lagrange equation. [Hood & Priest, 1979] found that for $\Psi \geq \Psi_{crit}$ the field would be unstable to a certain range of wavenumbers k in Equation (1.16). For $\Psi < \Psi_{crit}$ the field is stable to perturbation of *any* wavenumber and thus is in general stable.

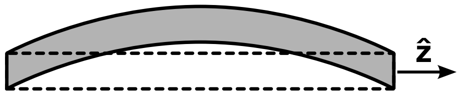

Figure 2. Kink mode displacement.

The studies of kink instability have practical applications in solar physics. Twisted flux tubes are believed to exist in the solar corona, as sunspots, the footpoints of the flux tubes with the strongest magnetic fields, are sometimes observed rotating

---

[4] In the sense of it having a definite axis and the diameter being negligibly small compared to the pressure gradients, so that the only force acting on the flux tube is the Lorentz force.

(see [Yan et al., 2008], [Brown et al., 2003] and references therein). Sunspot rotation is associated with the formation of S-shaped structures in the corona, observed in EUV and SXR, called *sigmoids.* The latter are indeed found to be likely to erupt [Canfield et al., 1999] and in the modern paradigm kink instability is thought to be one of the possible drivers for such eruptions [Canfield et al., 2000]. Existing numerical simulations demonstrate remarkable morphological correspondence between sigmoids and twisted flux tubes [Fan & Gibson, 2003] and between some eruptions and simulations of kink instability of twisted flux tubes, see [Rust, 2003, Török & Kliem, 2004, Rust & LaBonte, 2005, Gibson & Fan, 2008] and Figures 3 and 4.

The thin axisymmetric flux tube approximation, that is discussed above, is not always applicable for real and simulated structures. An example is shown in Figure 5, right panel. For a "thick" structure without a definite axis, Tw in the sense of Equations (1.14) and (1.15) could not be defined. Yet, in numerical simulations discussed above such structures are "twisted" in some sense and definitely undergo an instability. Apparently, there is a way of quantifying twist in an arbitrary-shaped structure through a quantity called *magnetic helicity.* In Chapter 2 I demonstrate that a generalization of Tw has an instability threshold in a manner similar to Tw for thin flux tubes. Please refer to this chapter for more information in Figures 3, 4 and 5.

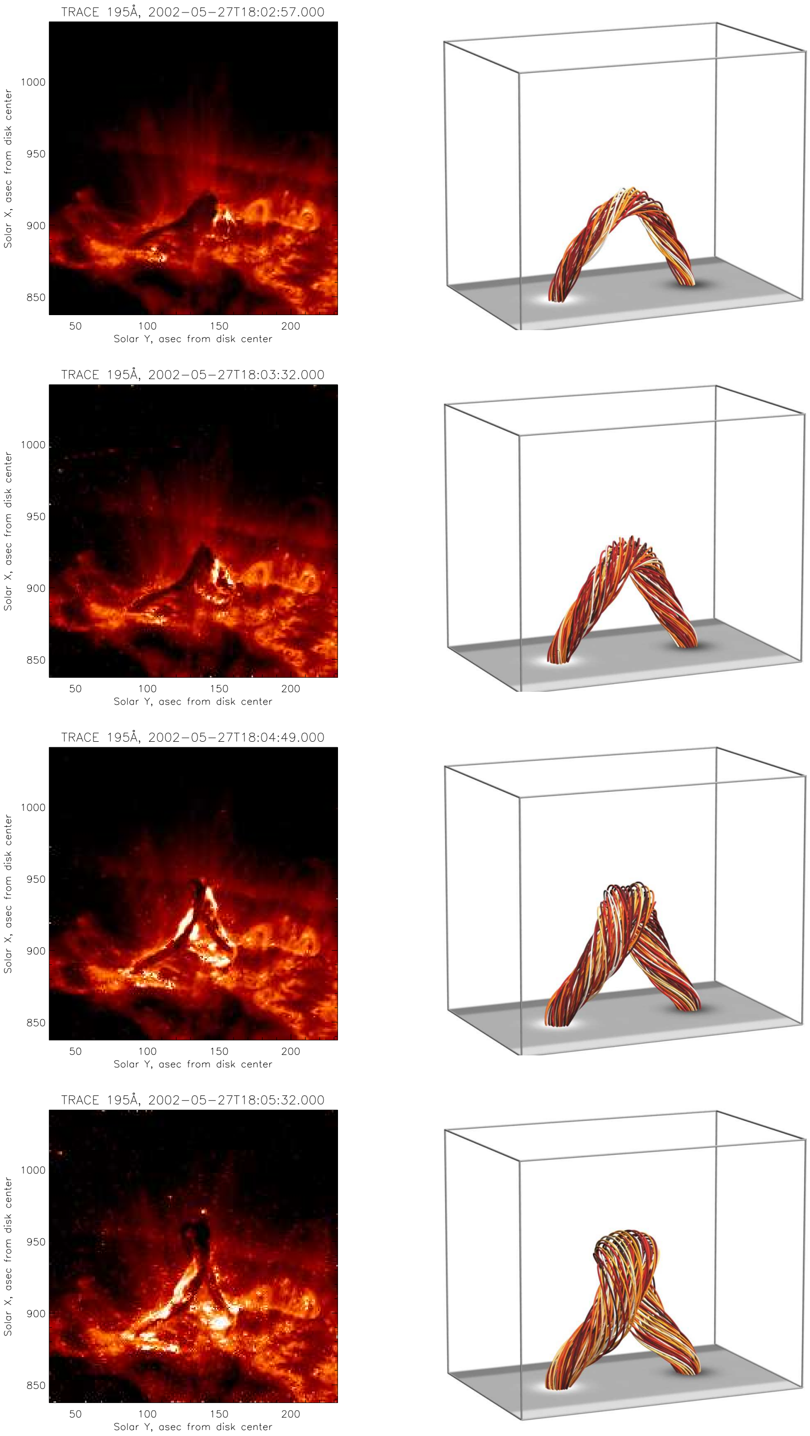

Figure 3. An example of a solar eruptive event that might have been caused by kink instability and a simulation of kink instability, using data from [Fan & Gibson, 2003]. The two columns represent time sequence of TRACE 195Å observations (the same event was mentioned in [Ji et al., 2003, Rust, 2003, Török & Kliem, 2004, Gibson & Fan, 2008]) and the simulation data; time increases from top to bottom and the sequence continues in Figure 4. TRACE images were rotated 90° counterclockwise and then reflected about vertical axis to enhance the similarity between the data and the simulations. For more details on the simulation data, see Chapter 2.

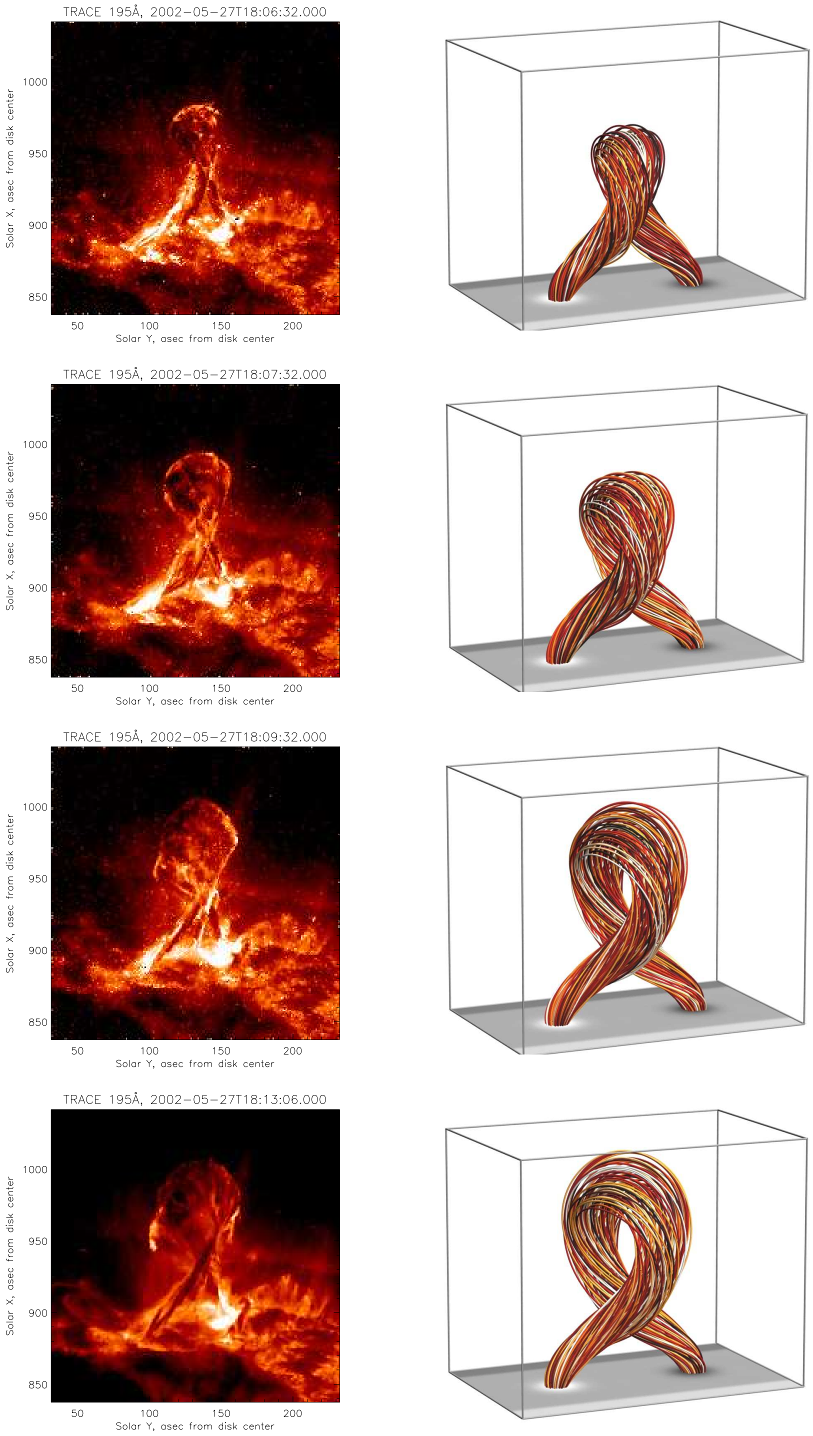

Figure 4. Continuation of Figure 3.

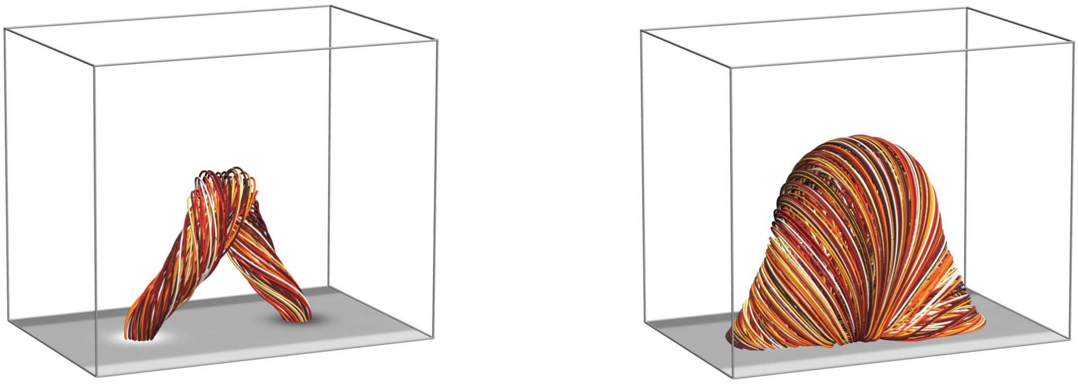

Figure 5. While the structure on the left could to some extent be modeled as a thin flux tube with a definite axis, the structure on the right definitely could not be. So for the structure on the right, Tw in the classical sense of an angle field lines wind about the axis, could not be estimated. Yet, such a structure can undergo an instability triggered by excessive twist of its field lines. The image on the left is in fact a subportion of the image on the right, simulation data which was designed as a set of twisted coaxial tubes and in this sense it indeed had an axis. In general no such assumption about the axis could be made. Simulation data adapted from [Fan & Gibson, 2003]; for more details on it, see Chapter 2.

1.4. Magnetic Helicity

Topological meaning of helicity.

Twist and writhe. Relative helicity.

Generalization of twist number.

Magnetic helicity of a field **B** in volume $\mathcal{V}$ is defined as

$$H(\mathbf{B},\mathcal{V}) = \int\limits_{\mathcal{V}} \mathbf{B}\cdot\mathbf{A}dV, \tag{1.18}$$

where **A** is a vector potential. Helicity defined this way is only gauge-independent if **B** is *fully confined* in $\mathcal{V}$, that is, if there is no magnetic flux across the boundary of $\mathcal{V}$: $\mathbf{B}\cdot\hat{\mathbf{n}}|_{\partial\mathcal{V}} = 0$ (in other words, no field lines enter or leave this volume). To see this, consider a gauge transformation $\mathbf{A}' = \mathbf{A} + \nabla\psi$. Then, using Equation (1.2) and the divergence theorem, Equation (1.18) would change by

$$\int\limits_{\mathcal{V}} \mathbf{B}\cdot\nabla\psi dV = \int\limits_{\partial\mathcal{V}} \psi\mathbf{B}\cdot\hat{\mathbf{n}}dS, \tag{1.19}$$

which would vanish if **B** is fully confined to $\mathcal{V}$.

It turns out [Berger & Field, 1984, Moffatt & Ricca, 1992] that magnetic helicity has a physical meaning related to the topology of the field. For example, let us consider **B** vanishing everywhere in the volume, except within two toroidal thin volumes $\mathcal{V}_1$ and $\mathcal{V}_2$, that carry fluxes Φ_1 and Φ_2 along axes L_1 and L_2; suppose at first that the field within these two tubes is untwisted in the sense described above. Suppose also that these two tubes are linked like the links in a chain, as in Figure 6, middle panel. The helicity of such a configuration is then

$$H(\mathbf{B}) = \int\limits_{\mathcal{V}_1} \mathbf{B} \cdot \mathbf{A} dV + \int\limits_{\mathcal{V}_2} \mathbf{B} \cdot \mathbf{A} dV. \tag{1.20}$$

Now using $\mathbf{B} dV = \Phi d\mathbf{l}$ and noticing that the flux along the tube has to be constant, we get

$$H(\mathbf{B}) = \Phi_1 \int\limits_{L_1} \mathbf{A} \cdot d\mathbf{l} + \Phi_2 \int\limits_{L_2} \mathbf{A} \cdot d\mathbf{l} = \pm 2\Phi_1\Phi_2, \tag{1.21}$$

provided the flux tubes are "untwisted", that is, there is no azimuthal flux of each tube across the contour of its own axis, because then the only flux across the surface bounded by L_1 is Φ_2 and the same is true for L_2 and Φ_1 (the sign would depend on the direction of one curve with respect to the surface normal of the other one, but would be the same for both terms of the sum). The result is easily generalized as

$$H(\mathbf{B}) = 2L\Phi_1\Phi_2, \tag{1.22}$$

where L is the total number of times one tube crosses the surface bound by the axis of the second tube. Note that such crossings can be either positive or negative, depending on the direction of the magnetic field compared to the direction of the normal to the surface. L, called the *Gauss linking number*, is a topological invariant that can't be changed *without breaking the tubes or making them penetrate into each other.* This is true in non-resistive plasma: two flux tubes do not reconnect or penetrate into each other. That means, their linkage number and thus helicity is a quantity preserved under any evolution of frozen-in plasma[5].

---

[5] In low-resistive plasma helicity is not conserved in general. When the diffusive term in Equation (1.5) is small, but not negligible, both energy and helicity dissipate. However, in this case helicity typically dissipates slower than magnetic energy [Berger, 1984].

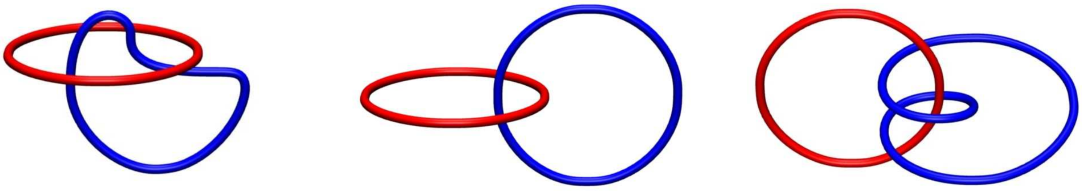

Figure 6. Examples of two interlinked circles with linking number, left to right: $L = 0$, $L = \pm 1$, $L = \pm 2$.

The result in Equation (1.22) was made assuming the flux tubes were untwisted. Let us now consider helicity of a *twisted* flux tube. A simple example of such is a uniformly twisted torus that carries flux Φ and twist Tw in the sense of Equation (1.15). Its helicity could be calculated by considering different thin tubes within the torus, as shown in Figure 7, if the tubes are sufficiently thin so that we can neglect their inner twist. Every pair of such tubes with fluxes $d\Phi_1$ and $d\Phi_2$ has helicity of $2d\Phi_1 d\Phi_2 Tw$, as in Equation (1.22) and the helicity of the torus as a whole is $H = Tw\Phi^2$ (the factor 1/2 ensures that each pair is not counted twice).

The result obtained in the previous paragraph *does* change with continuous deformations of the torus. Indeed, consider a torus with $Tw = 1$, as on the top row of Figure 8[6]. The axis of the torus could be deformed in such a way that the field inside it would appear untwisted[7], as shown in Figure 8, bottom row. The two subtubes,

---

[6] Of course, the sign of Tw would depend on the direction of the field lines. In this example let us suppose they are directed in such a way that $Tw > 0$.

[7] It is not obvious how to define an “untwisted” field within a shape like in the bottom row of Figure 8. [Berger & Field, 1984] adopt a following definition: when viewed from a plane projection, a line can be drawn on “top” of the tube along its entire length, that sets the zero of the azimuthal coordinate. We will further in Chapter 2 adopt a more rigorous definition: the zero of the azimuthal coordinate is to be transferred along the tube with parallel transport.

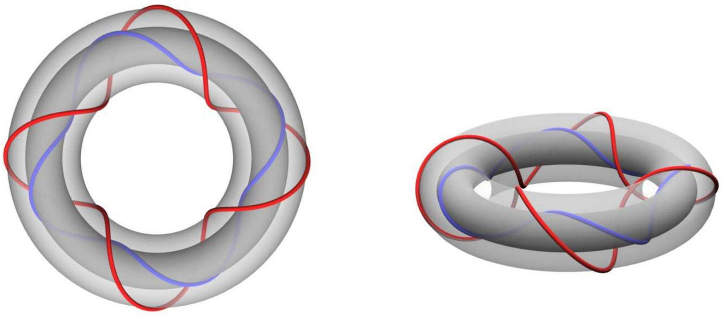

Figure 7. Two views of the same uniformly twisted torus. Two thin "subtubes", red and blue, are located on two different toroidal shells. If we neglect inner twist of both subtubes, their mutual linking number is $L = Tw = \pm 4$ (depending on the direction of the field lines), equal to the number of turns each tube makes about the minor axis of the torus.

however, would keep their linking number unchanged and the helicity of the field would remain constant.

In general it is accepted that linkage number for an arbitrary set of structures is

$$L = Tw + Wr. \tag{1.23}$$

This might be used to define *writhe number* Wr, but it could also be defined rigorously through integrals, so as Tw and L [Berger & Field, 1984, Moffatt & Ricca, 1992]. While Tw and L depend on mutual properties of *two* curves (e.g., an axis and a field line winding about it or two interlinked circles), Wr is a property of a *single* curve, that could be viewed as an amount of self-crossings in a planar projection of such curve, averaged over all possible viewing angles [Berger & Field, 1984, Moffatt & Ricca, 1992].

Helicity, by analogy with Equation (1.23), could be decomposed into *twist helicity* and *writhe helicity*. They could be defined in thin flux tubes as $Tw\Phi^2$ and $Wr\Phi^2$.

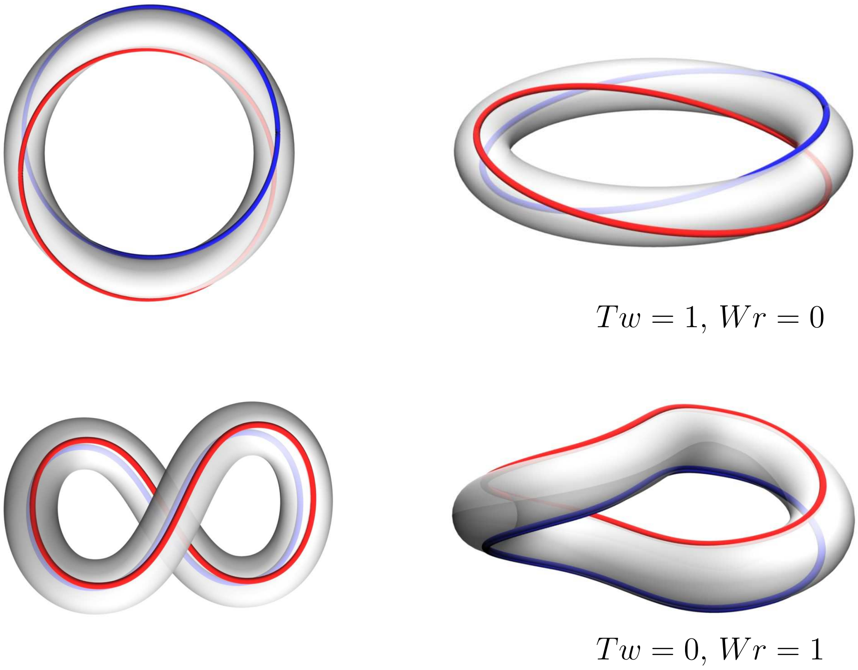

$Tw = 1,\, Wr = 0$

$Tw = 0,\, Wr = 1$

Figure 8. A uniformly twisted torus (top row) and an untwisted figure-8 tube (bottom row), that such torus could be deformed into, illustrate that Tw and Wr could convert into one another, however, keeping the topological invariant $L = Tw + Wr$ constant.

We will further explore ways to generalize these concepts on arbitrary magnetic configurations.

In these terms the scenario of kink instability, described above and illustrated by Figures 3 and 4, could be viewed as a *transformation of* Tw *into* Wr, subject to constant L.

The concept of helicity in the form described by Equation (1.18) could not, in general, be applied to the solar corona. Magnetic flux present at the lower boundary of the corona makes helicity not gauge-invariant, that is, a gauge transformation term like that in Equation (1.19) does not vanish at all boundaries of $\mathcal{V}$. [Berger & Field, 1984] first introduced *relative helicity* as a difference of two helicities:

$$H(\mathbf{B}_1, \mathbf{B}_2, \mathcal{V}) = H(\mathbf{B}_1, \mathcal{V}) - H(\mathbf{B}_2, \mathcal{V}) = \int\limits_{\mathcal{V}} \mathbf{B}_1 \cdot \mathbf{A}_1 dV - \int\limits_{\mathcal{V}} \mathbf{B}_2 \cdot \mathbf{A}_2 dV \tag{1.24}$$

provided the two fields have the same normal components everywhere on the boundary of the volume, and proved that *relative helicity is gauge-independent* if

$$\hat{\mathbf{n}} \times \mathbf{A}_1|_{\partial\mathcal{V}} = \hat{\mathbf{n}} \times \mathbf{A}_2|_{\partial\mathcal{V}} \,. \tag{1.25}$$

An alternative form for relative helicity was proposed by [Finn & Antonsen, 1985]:

$$H(\mathbf{B}_1, \mathbf{B}_2, \mathcal{V}) = \int\limits_{\mathcal{V}} (\mathbf{B}_1 - \mathbf{B}_2) \cdot (\mathbf{A}_1 + \mathbf{A}_2) dV, \tag{1.26}$$

which is fully equivalent to Equations (1.24) and (1.25) but places no restrictions on the vector potentials $\mathbf{A}_1$ and $\mathbf{A}_2$.

Relative helicity is defined on *a magnetic domain*, that could be viewed as a generalization of a thin flux tube concept. Within this dissertation a domain is a volume, bounded by magnetic surfaces (i.e., surfaces with no magnetic flux across them) except at the “footpoints” at the photospheric boundary, in which the magnetic flux is allowed to enter or leave.

Physically, relative helicity has the following meaning. It is the helicity of a composite field in the volume, that is a composition of $\mathcal{V}$ and a mirror reflection of $\mathcal{V}$ “underneath” the photosphere. The composite field is $\mathbf{B}_1$ in $\mathcal{V}$ and a mirror reflection of $\mathbf{B}_2$ in the reflection of $\mathcal{V}$. Such a field in such a volume is fully bounded by magnetic surfaces, so classical definition of helicity, as in Equation (1.18), could

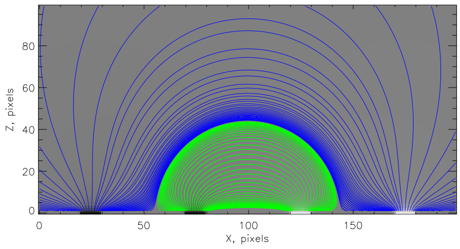

Figure 9. A side view on two *magnetic domains* (see text for description). $z = 0$ is the photosphere. Green and blue lines are field lines belonging to different domains. White and black dots at $z = 0$ locate $B_z \neq 0$ in the footpoints, negative and positive respectfully. Hereafter we will assume that the modeled piece of the corona is small enough so that the photosphere could be approximated as a plane, the coordinate system is Cartesian and z is the height above the photosphere.

be applied to it. Equation (1.25) ensures that field lines in this composite volume are still continuous curves and the resulting field still satisfies Equation (1.2).

For a given coronal field $\mathbf{B}$, its helicity is well-defined relative to a *reference field.* A popular choice of such reference field is a *potential field* $\mathbf{B}_P$, defined as a solution of $\nabla \times \mathbf{B}_P = 0$ (and it is called "potential" because there is a scalar function such that $\mathbf{B}_P = \nabla\phi$). There are several reasons for this choice. First, for a given set of boundary conditions $\mathbf{B}_P$ is *unique*, as ϕ is a solution of Laplace's equation (see Chapter 2). Second, $\mathbf{B}_P$ has *minimal magnetic energy* for given boundary conditions (see next section and [Taylor, 1974]), so a non-zero relative helicity would imply an energy above the minimal possible state. Third, a potential field has in a sense *the least possible twist* (the reasons for that will be clear in the next section and in Chapter 3).

Relative helicity is a quantity, that is well conserved in the corona, it was shown that even for low-resistivity plasma (but not of a zero resistivity) changes of $\mathbf{B}$ at the photosphere are much more effective for changing helicity than internal currents [Berger, 1984]. For a non-resistive plasma the only changes of relative helicity are due to changes in magnetic flux at the photosphere.

All the discussed theory of relative helicity was initially intended and has received a wide use for $\mathcal{V}$ being a half-space, $\mathcal{V} = Z_+$. But suppose the magnetic domain of interest is smaller than that, $\mathcal{D} \subset Z_+$, for example, the inner domain in Figure 9 (or a structure shown in Figure 5, either left or right panels). Suppose that the magnetic field vanishes outside of $\mathcal{D}$. Then, strictly speaking, every volume that contains $\mathcal{D}$ and is contained in Z_+, would be a magnetic domain. A potential field, however, would depend on the shape of such domain and so will relative helicity. Figure 10 shows two different potential fields, one considers $\mathbf{B}_P$ in a reflection of $\mathcal{D}$ for computing $H(\mathbf{B}, \mathbf{B}_P(\mathcal{D}), \mathcal{D})$ and the other one uses Z_- for computing $H(\mathbf{B}, \mathbf{B}_P(Z_+), Z_+)$. [Longcope & Malanushenko, 2008] have pointed out that the two relative helicities are different by $H(\mathbf{B}_P(Z_+), \mathbf{B}_P(\mathcal{D}), Z_+)$ and that $H(\mathbf{B}, \mathbf{B}_P(\mathcal{D}), \mathcal{D})$ has an "additive" property, that is, such helicity, called *additive self helicity* or H_A, of a composition of two domains would be equal to the sum of additive self helicities of the individual domains.

[Longcope & Malanushenko, 2008] have also mentioned, that $H_A = H_{Tw}$ for thin flux tubes and argued that H_A might be analogous to twist helicity in more complex configurations. In Chapter 2 I will further develop this analogy. I will present explicit numerical methods to compute additive self helicity. I will apply these methods to the simulation of kink instability from Figures 3, 4 and 5 to demonstrate that the quantity

$$Tw_{gen} = H_A/\Phi^2 \tag{1.27}$$

behaves like Tw in kink instability of a structure, that could not be approximated as a thin flux tube. That is, the instability happens when Tw_{gen} *exceeds certain threshold*, close to the threshold found for thin flux tubes, as in Equation (1.17). I also extract a “core” portion of the studied structure, that can be viewed as a thin flux tube and demonstrate that for this subdomain $Tw_{gen} = Tw$.

I thus conclude, that Tw_{gen}, given by Equation (1.27), could indeed be treated as a generalization of Tw from Eqution (1.15). This allows quantitative studies of kink instability in the structures of arbitrary shape.

1.5. Measurements of Twist in Solar Corona

Force-free fields and coronal α.

(N)LFFF. Relation between α and Tw.

Evolution of Tw for a rotating active region.

The results achieved in Chapter 2 allow one to study kink instability quantitatively, *provided* the coronal magnetic field $\mathbf{B}$ is known. The existing instruments, however, routinely provide observations of the magnetic field only at the photosphere.

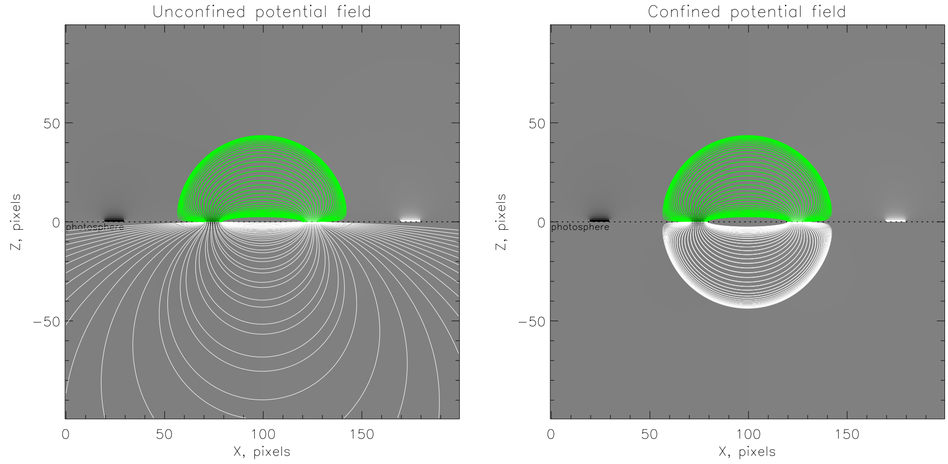

Figure 10. Two different potential fields that can be used to compute relative helicity for the same domain: the field confined to the volume of the domain and the field confined to half space.

Most of instruments, such as SOHO/MDI [Scherrer et al., 1995] and KPNO/Vacuum, provide the line-of-sight component of the magnetic field, which approximately equals to B_z close to the disk center. Such observations of B_{LOS} on the solar disk are called *magnetograms*. More modern instruments, such as KPNO/SOLIS and SDO/HMI are capable of observing all three components of $\mathbf{B}$, providing with *vector magnetograms*.

Magnetograms can be used to *extrapolate* magnetic field to the corona, assuming certain properties of the field. For example, for *force-free fields* Lorentz force, given by Equation (1.6), should vanish, what immediately leads to

$$\mathbf{J}||\mathbf{B}, \tag{1.28}$$

or that there is such a scalar constant $\alpha(\mathbf{r})$, that

$$\nabla \times \mathbf{B} = \alpha \mathbf{B}. \tag{1.29}$$

By taking divergence of both sides of Equation (1.29) with Equation (1.2) one could immediately verify, that

$$\mathbf{B} \cdot \nabla \alpha = 0, \tag{1.30}$$

meaning that while α might vary in space, it should be *constant along each field line*. Then by taking curl of both sides of Equation (1.29) and keeping Equation (1.2) in mind, Equation (1.29) can be transformed to

$$\nabla^2 \mathbf{B} + \alpha^2 \mathbf{B} = \mathbf{B} \times (\nabla \alpha). \tag{1.31}$$

If $\nabla \alpha = 0$, Equation (1.31) becomes a Helmholtz equation and its solution is called a *linear force-free* of a *constant-α field.* If $\nabla \alpha \neq 0$, Equation (1.31) remains a non-linear system and the solution is called *non-linear force-free field* (hereafter NLFFF).

While in general α is not constant, a coronal field is believed to try to relax to a constant-α field. This is because for a constant helicity (and unless there are changes at the photosphere, the ideal corona evolves in such a way to keep relative helicity constant) constant-α field has the smallest possible energy [Taylor, 1974]. If for a given configuration several constant-α fields are possible, the one with the smaller α has less energy. However, the study of [Burnette et al., 2004] found, by visually comparing lines of constant-α fields with visible coronal loops, that some solar active regions definitely can not be approximated with linear field.

There are many methods for solving the non-linear system (1.31), e.g., [Metcalf et. al., 2008, Schrijver et. el., 2008, DeRosa et. al., 2009] and references therein.

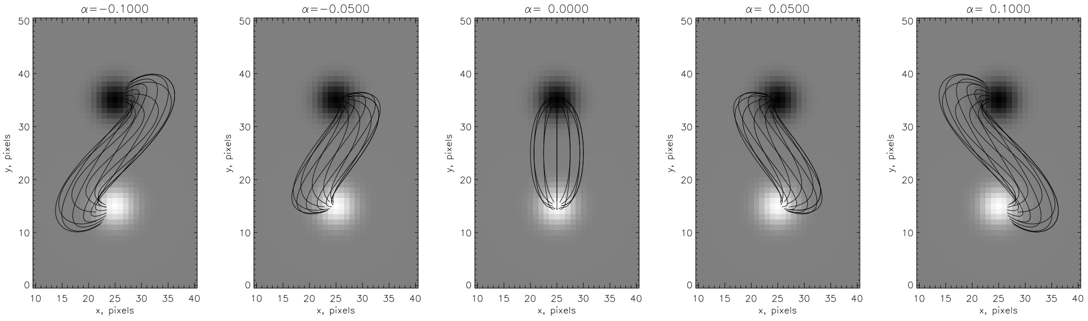

Figure 11. Constant-α fields, with α increasing from left to right and $\alpha = 0$ for the middle image. Gray scale is B_z at the photosphere and the lines are the projections of several of the field lines on XY plane. The lines are chosen to "outline" a flux tube with circular cross-section at $y = 0$ and some height z above the photosphere.

However, obtaining a NLFFF has proven to be an extremely challenging problem on its own. In the beginning of Chapter 3 I outline basic problems that ultimately lead to the fact that different methods, when applied to the same data, may give significantly different results, as was found in [DeRosa et al., 2009].

In this dissertation I develop a way of estimating Tw_{gen} in the solar corona *without* the aid of NLFFF models. The similarity between field lines of a NLFFF and the coronal loops is usually treated as an important measure of success or failure of the result. The method presented in this dissertation *works backwards* in this scheme. It *uses coronal loops* to construct field lines of a constant-α field, that best match coronal loops in the projection onto the plane of the sky. Figure 11 illustrates how field lines of different constant-α fields have noticeably different shapes. α is allowed to vary from loop to loop, so every field line, "reconstructed" this way, belongs to a different constant-α field in Z_+.

Strictly speaking, a composition of two force-free fields would not in general be a force-free field. To verify this, it is enough to consider two pairs: $\mathbf{B}_1$, α_1 and $\mathbf{B}_2$, α_2, each obeying Equation (1.29) and verify that $\mathbf{B}_1+\mathbf{B}_2$ would only obey Equation (1.29), if $\alpha_1(\mathbf{r}) = \alpha_2(\mathbf{r})$.

It is also not possible in general to obtain a force-free field by combining subdomains of different constant-α and confined to Z_+ fields. While the Lorentz force will vanish within each of such subdomain, it is not guaranteed to vanish on the boundaries between these domains.

I just tried to convince the reader that my method of estimating coronal α should not work. In Chapter 3 I try to convince the reader of the opposite. I make theoretical arguments and support them with thorough tests on many analytic NLFFF's. It turns out that such a method[8] *does work* under *certain* circumstances, that are relevant to solar corona.

The (N)LFFF procedure estimates the following quantities for each observed coronal loop:

- 3D shape $\mathbf{r}(l)$ of a field line, that was found to match the coronal loop.
- α_{found} of a constant-α field it belongs to. In Chapter 3 I show that this α_{found} correlates with α_{real} of the original synthetic "loop" in the non-linear field.
- The profile of (constant-α) magnetic field, $\mathbf{B}(l)$, along the field line. It was also found to correlate with the non-linear field that has produced such loop, when

---

[8] In Chapter 3 I refer to it as "α-h fit", but later Carolus Schrijver has suggested a better name: a (non)-linear force-free field, hereafter (N)LFFF.

> tried on synthetic examples. The correlation was the best at the photosphere. As (N)LFFF does not use vector magnetograms as an input, its outcome is in a sense an independent measure of horizontal components of $\mathbf{B}$.

Figure 12 shows the result of one such reconstruction for real solar data, shapes of field lines and their α.

Such an outcome cannot *per se* be plugged in Equation (1.24). This is because the latter involves a volume integral and the result of (N)LFFF is not volume-filling data. It turns out, however, that α by itself is *closely related* to Tw.

For example, for a uniformly twisted cylinder, described by Equation (1.13), it can be easily verified, that

$$\alpha = \frac{2b}{1 + b^2\rho^2}, \tag{1.32}$$

and if the cylinder is *thin*, i.e., $\rho/L \ll 1$, then

$$2\pi Tw \approx \alpha L/2. \tag{1.33}$$

For a domain in a constant-α field, [Longcope & Malanushenko, 2008] demonstrated that

$$2\pi H_A/\Phi^2 \approx \alpha \langle L_i \rangle /2, \tag{1.34}$$

where $\langle L_i \rangle$ is the average length of field lines in that domain. Equations (1.33) and (1.34), along with Tw_{gen} given in Equation (1.27) and supported with results from Chapter 2, *establish a connection* between Tw_{gen} and α via H_A as a bridge between them. The (N)LFFF method, developed in Chapter 3, allows to estimate α.

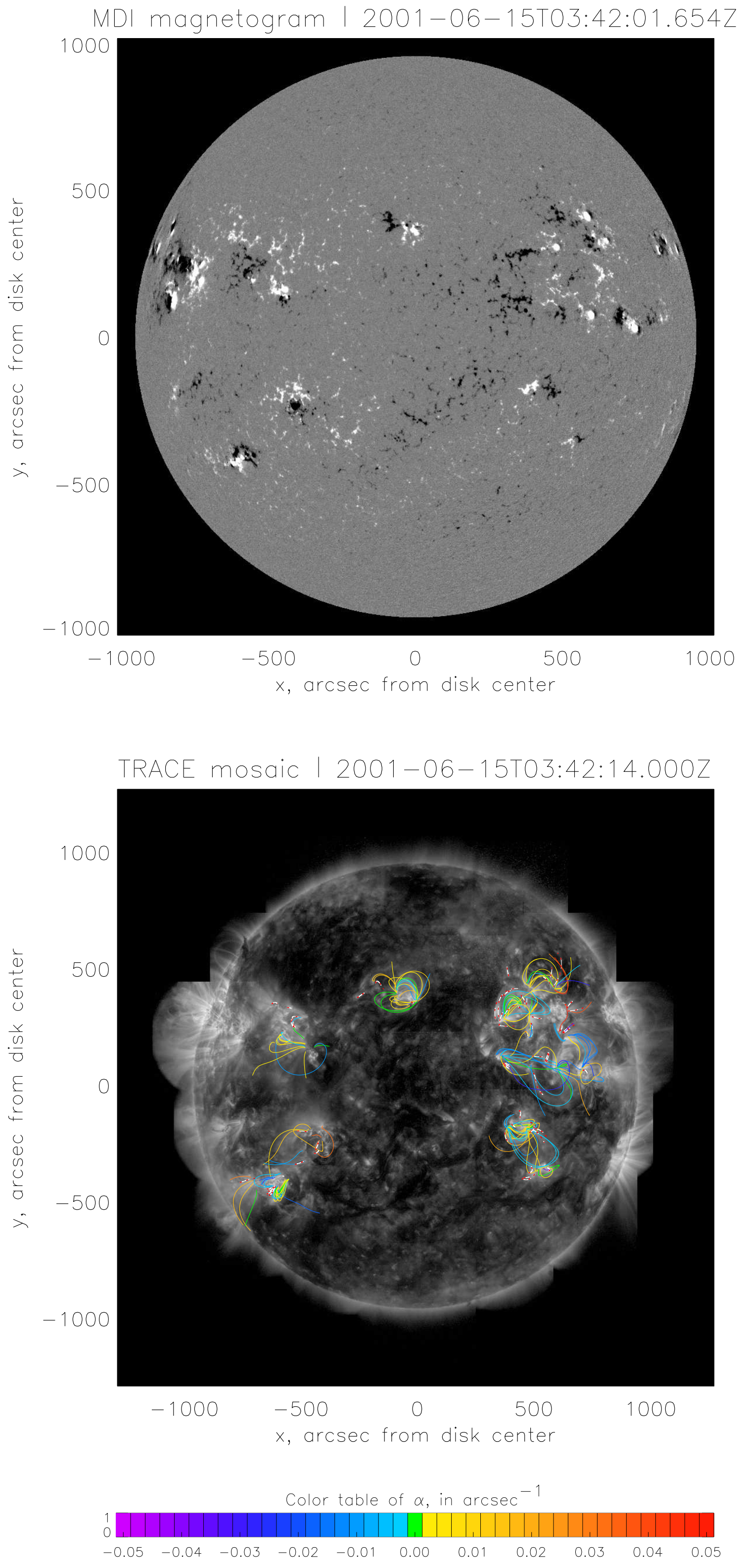

Figure 12. A magnetogram (top panel) and EUV image (bottom panel). The field lines, reconstructed by (N)LFFF, are plotted over the EUV image. Different colors correspond to different values of α. The few loops for which the procedure has failed, are plotted as dashed white-red lines.

In Chapter 4 I use (N)LFFF method to study evolution of twist in a rotating active region. Its footpoints were observed rotating at a well-measurable rate [Longcope et al., 2007] and its Tw_{gen}, measured *in the corona* should change accordingly to its change at the photosphere. I observe that the rate of change of Tw_{gen} in the corona matches its rate of injection in the photosphere. This gives observational evidence of how helicity flows into the corona through photospheric motion.

In Chapter 5 I give an overview of possible impact of this work and plan the future research on this topic.

2. ADDITIVE SELF HELICITY AS A KINK MODE THRESHOLD

2.1. Abstract

In this chapter we propose that additive self helicity, introduced by [Longcope & Malanushenko, 2008], plays a role in the kink instability for complex equilibria, similar to twist helicity for thin flux tubes [Hood & Priest, 1979, Berger & Field, 1984]. We support this hypothesis by a calculation of additive self helicity of a twisted flux tube from the simulation of [Fan & Gibson, 2003]. As more twist gets introduced, the additive self helicity increases, and the kink instability of the tube coincides with the drop of additive self helicity, after the latter reaches the value of $H_A/\Phi^2 \approx 1.5$ (where Φ is the flux of the tube and H_A is additive self helicity).

We compare additive self helicity to twist for a thin sub-portion of the tube to illustrate that H_A/Φ^2 is equal to the twist number, studied by [Berger & Field, 1984], when the thin flux tube approximation is applicable. We suggest, that the quantity H_A/Φ^2 could be treated as a generalization of a twist number, when thin flux tube approximation is not applicable. A threshold on a generalized twist number might prove extremely useful studying complex equilibria, just as twist number itself has proven useful studying idealized thin flux tubes. We explicitly describe a numerical method for calculating additive self helicity, which includes an algorithm for identifying a domain occupied by a flux bundle and a method of calculating potential

magnetic field confined to this domain. We also describe a numerical method to calculate twist of a thin flux tube, using a frame parallel transported along the axis of the tube.

2.2. Introduction

According to a prevalent model coronal mass ejections (CMEs) are triggered by current-driven magnetohydrodynamic (MHD) instability related to the external kink mode [Hood & Priest, 1979, Török et al., 2004, Rachmeler et al., 2009]. The external kink mode, in its strictest form, is a helical deformation of an initially symmetric, cylindrical equilibrium, consisting of helically twisted field lines. The equilibrium is unstable to this instability if its field lines twist about the axis by more than a critical angle, typically close to 3π radians [Hood & Priest, 1979, Baty, 2001]. The helical deformation leads to an overall decrease in magnetic energy, since it shortens many field lines even as it lengthens the axis.

Equilibria without symmetry can undergo an analogous form of current-driven instability under which global motion lowers the magnetic energy [Bernstein et al., 1958, Newcomb, 1960]. Such an instability implies the existence of another equilibrium with lower magnetic energy. The spontaneous motion tends to deform the unstable field into a state resembling the lower energy equilibrium. Indeed, it is generally expected that there is at least one minimum energy state from which deformation cannot lower the the magnetic energy without breaking magnetic field lines; its energy is the absolute minimum under ideal motion.

Linear stability and instability are determined by the energy change under infinitesimal motions. An equilibrium will change energy only at the second order since first order changes vanish as a requirement for force balance. Ideal stability demands that no deformation decrease the energy at second order, while instability will result if even one energy-decreasing motion is possible. The infinite variety of possible motions make it impractical to establish stability in any but the simplest and most symmetric equilibria.

Based on analogy to axisymmetric systems it is expected that general equilibria, including those relevant to CMEs, are probably unstable when some portion of their field lines are twisted about one another by more than some critical angle. This expectation was mentioned in a study by [Fan & Gibson, 2003] of the evolution of a toroidal flux rope into a pre-existing coronal arcade. They solved time-dependent equations of MHD in a three-dimensional, rectangular domain. Flux tube emergence was simulated by kinematically introducing an isolated toroidal field through the lower boundary. The toroidal field was introduced beneath a pre-existing arcade slowly enough that the coronal response never approached the local Alfvén speed. Fan and Gibson concluded that the system underwent a current-driven instability after a critical amount of the torus had been introduced. They bolstered this claim by performing an auxiliary run where the kinematic emergence was halted and the system allowed to evolve freely; it settled into an equilibrium.

While twist angle has proven useful in a few cases, it is difficult to demonstrate its utility as a threshold in general, asymmetric equilibria. Indeed, in any but a few very symmetric cases there is no simple, obvious way to define the angle by which the field lines wrap about one another. The local rate of twist is given by the current density, which is after all the source of free energy powering the instability. On the other hand, excessive local current density is not sufficient to drive instability. This fact is illustrated by numerous examples of discontinuous field which are minimum energy states.

It has been suggested that a threshold exists, in general equilibria, for some global quantity such as free magnetic energy or helicity [Zhang et al., 2006, Low, 1994]. If this is the case then we expect the instability to lower the value of this global quantity so that it falls below the threshold value in the lower-energy, stable equilibrium. Magnetic helicity is a logical candidate to play this role since it is proportional to total twist angle in cylindrical fields. Relative helicity in particular is a proxy for currents. Helicity is, however, conserved under ideal motion and therefore will not be reduced to a sub-threshold value by an ideal instability.

The total helicity of a thin, isolated flux tube can be written as a sum of two terms called twist and writhe [Berger & Field, 1984, Moffatt & Ricca, 1992],

$$H = H_T + H_W .$$

The writhe depends on the configuration of the tube's axis while the twist depends on the wrapping of field lines about one another. A cylindrical tube has a perfectly straight axis and therefore zero writhe helicity. Any ideal motion which helically deforms the entire flux tube will increase the magnitude of the writhe helicity. Since the motion preserves total helicity the change in writhe must be accompanied by an offsetting change in twist helicity. If the writhe has the same sign as the initial twist, then the motion will decrease the twist helicity. In cases where the magnetic energy depends mostly on twist, this motion will decrease the magnetic energy [Linton & Antiochos, 2002]. The straight equilibrium is therefore unstable to an external kink mode.

Topologically, the foregoing properties of magnetic field lines could be compared to the properties of thin closed ribbons. One may introduce *twist number*, *writhe number* and their combination, called *linkage* number, is a preserved quantity in the absence of reconnection [Berger & Field, 1984, Moffatt & Ricca, 1992],

$$L = Tw + Wr.$$

By analogy to the case of a thin isolated flux tube we consider the twist helicity, rather than the total helicity, to be the most likely candidate for a stability threshold. Indeed, within a thin flux tube it is possible to derive a net twist angle among field lines and $H_T = \Phi^2 Tw = \Phi^2 \Delta\theta / 2\pi$, where Φ is the total magnetic flux through a cross-section of the tube and $\Delta\theta$ is the net twist angle.

Twist and writhe are, however, defined only in cases of thin, isolated magnetic flux tubes, and can no more set the threshold we seek than the net twist angle can.

Recently [Longcope & Malanushenko, 2008] introduced two generalizations of relative helicity applicable to arbitrary sub-volumes of a magnetic field. They termed both generalized self-helicity, and the two differed only by the reference field used in their computation. The one called *additive self-helicity* (that we denote H_A) uses a reference field confined to the same sub-volume as the original field, and can be interpreted as a generalization of the twist helicity to arbitrary magnetic fields. The additive self-helicity of a thin, isolated flux tube is exactly the twist helicity.

Since the additive self-helicity can be computed for arbitrary magnetic fields we propose that it (normalized by the squared flux) is the quantity to which current-driven instability sets an upper limit, which could be considered a generalized twist number:

$$Tw_{(gen)} = H_A/\Phi^2. \tag{2.1}$$

The chapter is organized as follows. In Section 2.3, we describe a method for calculating additive self helicity and $Tw_{(gen)}$ numerically. There are two large and nontrivial parts of this calculation, that we describe in 2.3.1 and 2.3.2: locating a domain containing a given flux bundle and constructing a potential field in this domain by Jacobi relaxation. In Section 2.4, we apply the method to a simulation to support our hypothesis, the emerging twisted flux tube from [Fan & Gibson, 2003]. In 2.4.1 we briefly describe this simulation, and then in 2.4.2 we show different embedded domains defined by different subportions of the footpoints. In 2.4.3 we describe, how the twist of [Berger & Field, 1984] could be calculated for those of the domains for which thin flux tube approximation is applicable. In Section 2.5 we present the evolution of additive self helicity, unconfined self-helicity, twist (for "thin" domains) and the integrated helicity flux in the simulation. We demonstrate that $Tw_{(gen)}$ increases corresponding to helicity flux, that it drops after it reaches a certain value (about 1.5) and that this drop coincides with the rapid expansion of the tube due to the kink instability. We also demonstrate that the unconfined self helicity grows only when helicity flux is nonzero and that it stays constant when kink instability happens. We also show that $Tw_{(gen)}$ corresponds to Tw when thin flux tube approximation is applicable.

2.3. Numerical Solutions

The object of study is a magnetic field $\mathbf{B}(\mathbf{r})$ defined in a domain $\mathcal{D}$, $\mathbf{r} \in \mathcal{D}$, that lies on and above the photosphere, $z \geq 0$. By domain we understand a volume that encloses the field: $\mathbf{B} \cdot \hat{\mathbf{n}} = 0$ on all boundaries, $\partial\mathcal{D}$, except at the photosphere, where $\mathbf{B} \cdot \hat{\mathbf{n}} = B_z(x, y, z = 0)$. Figure 9 illustrates this concept. The self-helicity is given by

$$H_A\left(\mathbf{B}, \mathbf{B}_P\left(\mathcal{D}\right), \mathcal{D}\right) = \int\limits_{\mathcal{D}} \left(\mathbf{B} - \mathbf{B}_P\right) \cdot \left(\mathbf{A} + \mathbf{A}_P\right) dV, \tag{2.2}$$

as defined in [Longcope & Malanushenko, 2008]. Here $\mathbf{B}_P$ is the potential magnetic field, whose normal component matches the normal component of $\mathbf{B}$ on the boundary

$\partial\mathcal{D}$,

$$\mathbf{B}_P \cdot \hat{\mathbf{n}}|_{\partial\mathcal{D}} = \mathbf{B} \cdot \hat{\mathbf{n}}|_{\partial\mathcal{D}}, \tag{2.3}$$

$\mathbf{A}$ and $\mathbf{A}_P$ are the vector potentials of $\mathbf{B}$ and $\mathbf{B}_P$ respectively (as discussed in [Finn & Antonsen, 1985], helicity, defined this way is gauge-independent).

Once the self-helicity is known, the twist is given by Equation (2.1) with Φ being the total signed flux of the footpoints of the configuration:

$$\Phi = \int\limits_{z=0, B_z \geq 0} B_z dxdy = - \int\limits_{z=0, B_z \leq 0} B_z dxdy. \tag{2.4}$$

In the next two sections we discuss methods of numerically obtaining $\mathcal{D}$, from given footpoints, and $\mathbf{B}_P$.

2.3.1. Finding the Domain.

In order to describe the domain on a grid we introduce the support function:

$$\Theta(\mathbf{r}) = \begin{cases} 1, \text{ if } \mathbf{r} \in \mathcal{D} \\ \\ 0, \text{ if } \mathbf{r} \notin \mathcal{D}. \end{cases}$$

This is a function of the given magnetic field $\mathbf{B}$ and some photospheric area, called the boundary mask. By definition, every field line, initiated at any point on the boundary mask and having the other footpoint somewhere within the mask, is completely inside the domain $\mathcal{D}$. If the field line traced in both directions from some coronal point ends within the photospheric mask, then this point also belongs to the domain. In numerical computations we replace "point" with a small finite volume, voxel v_{ijk} (3-dimensional pixel). We define a voxel to be inside $\mathcal{D}$ (equivalent to saying $\Theta\left(v_{ijk}\right) = 1$), if there is *at least one* point inside it that belongs to $\mathcal{D}$.

The simplest method of constructing the support function would be to trace a field line in both direction from every voxel of the computational grid, set $\Theta = 1$ in the voxel if the footpoints both terminate in pixels from the boundary regions, and set $\Theta = 0$ otherwise. This, however, is a very time-consuming algorithm, especially for large arrays of data. Instead we use an algorithm which reduces the computational time by tracing field lines from a subset of voxels. It works by progressively adding voxels to Θ adjacent to those already known to belong to $\mathcal{D}$.

We add a voxel centered at $r_{i,j,k}$ to the domain under two different circumstances. 1. A field line initialized somewhere within the volume of the voxel $v_{i,j,k}$, centered at $r_{i,j,k}$, is found to have both footpoints within the boundary mask. 2. A field line initiated in some other voxel, and determined to belong to $\mathcal{D}$, passes through some portion of the volume $v_{i,j,k}$.

Initially, the domain consists only of footpoint voxels, so the initial step is to trace field lines *initiated at the footpoints*, assuming, that at least some of these lines will lie in the domain.

We illustrate the method on a simplistic case of a potential magnetic field, confined to a half-space, with $B_z = 0$ everywhere at the photosphere, except at four pixels, as shown in Figure 13. We have computed the magnetic field inside a small box of $15 \times 15 \times 15$ pixels, centered around the photospheric sources. The boundary mask consists of these four voxels at the photosphere with non-zero vertical magnetic field. In this simplistic example the initial guess would be four field lines, initiated at four footpoint voxels, as shown in Figure 13, left (note that in this particular example a field line, initiated at one voxel, ends at another voxel within the mask and thus is the same as the field line, initiated at that another voxel, so these four initial guesses are really two, not four field lines). The voxels of the initial guess are shown with crosses.

In an algorithm, this would be the first step:

Step 1: Make the initial guess: trace field lines from the footpoints.

As soon as an initial step is made, the next step is to assume, that the *immediate neighbourhood* of voxels known to be in $\mathcal{D}$ are likely to be also in the domain. Thus, in the next (iterative) search the following steps are performed:

Step 2: Locate voxels on the boundary of the current domain.

Step 3: For every voxel on the boundary: trace a field line and check whether it is in the domain.

If yes: Add the voxel to the domain. Add all voxels along the line to the domain. Exclude them from the boundary (there is no need to check them again).

If no: Mark the voxel as "questionable". (If there is a field line, which passes through the voxel and does not belong to the domain, then at least part of the voxel is outside of the domain. Since its immediate neighbourhood is in the domain, then it is possible that part of it is also in the domain.)

Loop: Repeat steps 2-3 until *all* the voxels in the boundary are "questionable" and no new voxels are added.

When the iterative search does not find any new voxels, we make the final check of the boundary voxels. The idea is to trace field lines from all corners of such "questionable" voxels to see, which corners (and thus which part of a voxel) belongs to the domain. We consider this to be optional check, which may improve the precision of the definition of the domain by at most one layer of voxels.

This last search may also give information about the normal to the domain surface. If it is known that some corners of a voxel are in the domain and some are not, it is possible to approximate the boundary as a plane separating those two groups of corners.

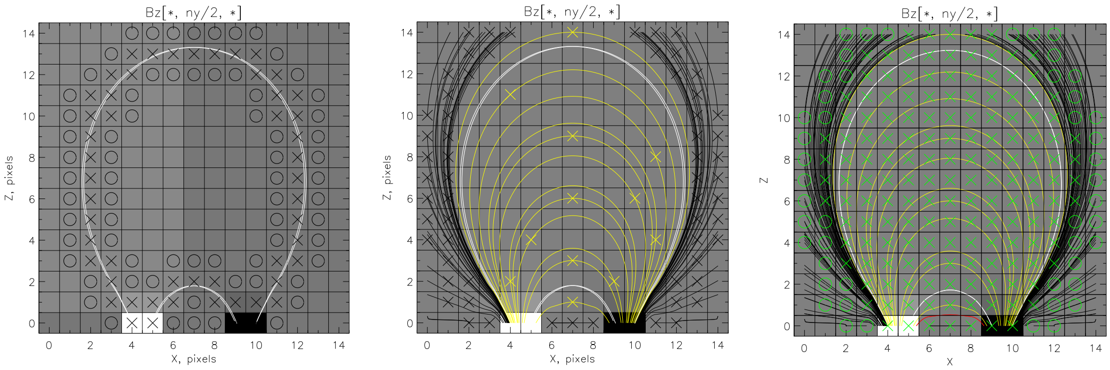

Figure 13. *(left)* — The first iteration of the iterative search: from the initially selected voxels (crosses), check those surrounding (circles) for membership in the domain. Repeat until no "surrounding" voxels can be added to the domain. *(middle)* — The voxels, checked on *all* iterations in the middle plane. For every field line, a cross shows where it was initialized. Yellow are "accepted" lines (and thus *all* voxels that contain them are "accepted") and black are "not accepted" lines (and thus *only* voxels where these lines were initializes from are "not accepted"). *(right)* – The end result. The green crosses mark voxels that are found to belong to the domain and the green circles are the neighbourhood of the domain. White (initial), yellow (iterative) and red (final) field lines are traced and found to be in the domain; black lines are found to be not in the domain. Note that the domain is "covered" by much fewer lines than an exhaustive search would do.

2.3.2. Constructing the Potential Field $\mathbf{B}_p$ Confined to the Domain

Once the domain has been determined, the next step is to construct the potential magnetic field confined to it. We use a common relaxation method on a staggered grid in order to account for the complex boundaries of $\mathcal{D}$.

We introduce a scalar potential $\mathbf{B}_p = \nabla\chi$ and look for the solution of the Laplace's equation for χ

$$\nabla \cdot \mathbf{B}_P = \nabla^2\chi = 0.$$

By the definition of $\mathcal{D}$, field lines never cross $\partial\mathcal{D}$, except at the lower boundary, $z = 0$. Thus, boundary conditions for $\mathbf{B}_p$ could be written as: $\mathbf{B}_p \cdot \hat{\mathbf{n}}|_{\partial\mathcal{D}, z\neq 0} = 0$ and $\mathbf{B}_p \cdot \hat{\mathbf{n}}|_{\partial\mathcal{D}, z=0} = \mathbf{B}_z(x, y)$. This is equivalent to Neumann boundary conditions for χ:

$$\begin{array}{rcl} \frac{\partial \chi}{\partial n}\Big|_{\partial\mathcal{D}, z\neq 0} & = & 0, \\ \frac{\partial \chi}{\partial z}\Big|_{\partial\mathcal{D}, z=0} & = & B_z(x, y). \end{array} \tag{2.5}$$

The Algorithm for the Relaxation Method

We use the Jacobi iterative method (see, for example, [LeVeque, 1955]) to solve for the potential field. Here we briefly summarize the algorithm and further explain in details. The $n + 1$-th iteration is

1. $\forall \mathbf{r} \in \mathcal{D}$: calculate a new iteration $\chi^{[n+1]}$ as a solution of the equation $\chi^{[n+1]} - \chi^{[n]} = Kh^2\nabla^2\chi^{[n]}$, where h is the grid spacing. The Laplacian $\nabla^2\chi^{[n]}(\mathbf{r})$, found using standard finite difference methods, is equivalent to an average over some stencil of neighbouring points minus the central value; K is a constant that depends on the exact shape of the stencil.

2. $\forall \mathbf{r}_b \in \partial\mathcal{D}$: set $\chi^{[n+1]}(\mathbf{r}_b)$ so as to satisfy boundary conditions (BCs).

3. Repeat steps 1–2, until the difference between $\chi^{[n]}(\mathbf{r})$ and $\chi^{[n+1]}(\mathbf{r})$ is sufficiently small in some sense (namely, until $||\chi^{[n+1]} - \chi^{[n]}|| < \epsilon$, where ϵ is pre-defined small number).

Staggered Mesh

The functions $B_x(x,y,z)$, $B_y(x,y,z)$ and $B_z(x,y,z)$ are defined on the same mesh points (x_i, y_j, z_k). If we are interested in finding $\chi(x,y,z)$, so that $B_x = \frac{\partial \chi}{\partial x}$, $B_y = \frac{\partial \chi}{\partial y}$ and $B_z = \frac{\partial \chi}{\partial z}$, it is advantageous to define χ *in between* the original mesh points and calculate the derivatives using finite difference as following:

$$B_x(x_i, y_j, z_k) = \frac{\chi(x_{i+1/2}, y_j, z_k) - \chi(x_{i-1/2}, y_j, z_k)}{x_{i+1/2} - x_{i-1/2}} ,$$

and so on for B_y and B_z. χ, then, would only be defined in the middle of *the faces* of cubic voxels, i.e., at points $(i \pm 1/2, j, k)$, $(i, j \pm 1/2)$ and $(i, j, k \pm 1/2)$.
Such a mesh, called a *"cartesian staggered mesh"*, is known to have better numerical properties, such as immunity from decoupling of variables and having a smaller numeric dispersion (see, for example, [Perot, 2000]).

The finite difference approximation of a Laplacian at one point can be interpreted as a weighted average over a stencil of several points minus the value at that point. For example, in the 2D case the second order approximation to $\nabla^2\chi(x,y)$ on a uniform Cartesian grid at the point (x_i, y_j) could be computed over a 5-point stencil:

$$\nabla^2\chi\left(x_i, y_j\right) \approx \frac{1}{h^2}\left(\chi\left(x_{i-1}, y_j\right) + \chi\left(x_{i+1}, y_j\right) + \chi\left(x_i, y_{j-1}\right) + \chi\left(x_i, y_{j+1}\right) - 4\chi\left(x_i, y_j\right)\right)$$

(here h is the spacing of the grid). It could be rewritten as

$$\chi\left(x_i, y_j\right) \approx \frac{1}{4}\left(\chi\left(x_{i-1}, y_j\right) + \chi\left(x_{i+1}, y_j\right) + \chi\left(x_i, y_{j-1}\right) + \chi\left(x_i, y_{j+1}\right)\right) - \frac{h^2}{4}\nabla^2\chi\left(x_i, y_j\right).$$

The Jacobi method uses this equation to iteratively update the value at the point, constantly assuming $\nabla^2\chi = 0$. In the case of the 5-points stencil the updated value would be

$$\chi^{[n+1]}\left(x_i, y_j\right) = \frac{1}{4}\left(\chi^{[n]}\left(x_{i-1}, y_j\right) + \chi^{[n]}\left(x_{i+1}, y_j\right) + \chi^{[n]}\left(x_i, y_{j-1}\right) + \chi^{[n]}\left(x_i, y_{j+1}\right)\right).$$

In our case of a 3D staggered mesh, choosing a stencil becomes more complicated. We propose a 13-point scheme, shown on the right of Figure 14 (black dots). To motivate this stencil, we derive it from the "unstaggered" one (Figure 14, left, gray dots). In an "unstaggered" finite differencing scheme the $[n+1]$-th iteration in Jacobi method would be expressed as

$$6\chi^{[n+1]}(O) = \chi^{[n]}(A_1) + \chi^{[n]}(A_2) + \chi^{[n]}(B_1) + \chi^{[n]}(B_2) + \chi^{[n]}(C_1) + \chi^{[n]}(C_2).$$

But for the staggered mesh χ is undefined at these nodes. This can be resolved by setting χ at each "gray" point to be equal to the *average* of its 4 closest neighbours,

$$\begin{array}{rcl}
\chi^{[n]}(A_1) & = & \frac{1}{4}\left[\chi^{[n]}(SA_1) + \chi^{[n]}(TA_1) + \chi^{[n]}(SA_1) + \chi^{[n]}(O)\right], \\
\chi^{[n]}(B_1) & = & \frac{1}{4}\left[\chi^{[n]}(SB_1) + \chi^{[n]}(TB_1) + \chi^{[n]}(SB_1) + \chi^{[n]}(O)\right], \\
\chi^{[n]}(C_1) & = & \frac{1}{4}\left[\chi^{[n]}(TA_1) + \chi^{[n]}(TA_2) + \chi^{[n]}(TB_1) + \chi^{[n]}(TB_2)\right]
\end{array}$$

and so on. Then we may substitute this in the original expression and get:

$$\begin{array}{rcl}
6\chi^{[n+1]}(O) & = & 2 \times \frac{1}{4}\left[\chi^{[n]}(TA_1) + \chi^{[n]}(TA_2) + \chi^{[n]}(BA_1) + \chi^{[n]}(BA_2)\right] + \\
 & + & 2 \times \frac{1}{4}\left[\chi^{[n]}(TB_1) + \chi^{[n]}(TB_2) + \chi^{[n]}(BB_1) + \chi^{[n]}(BB_2)\right] + \\
 & + & \frac{1}{4}\left[\chi^{[n]}(SA_1) + \chi^{[n]}(SA_2) + \chi^{[n]}(SB_1) + \chi^{[n]}(SB_2)\right] + \\
 & + & 4 \times \frac{1}{4}\chi^{[n]}(O),
\end{array}$$

which is eqivalent to

$$\begin{array}{rcl}
\chi^{[n+1]}(O) & = & \frac{1}{12}\left[\chi^{[n]}(TA_1)+\chi^{[n]}(TA_2)+\chi^{[n]}(BA_1)+\chi^{[n]}(BA_2)\right]+ \\
& + & \frac{1}{12}\left[\chi^{[n]}(TB_1)+\chi^{[n]}(TB_2)+\chi^{[n]}(BB_1)+\chi^{[n]}(BB_2)\right]+ \\
& + & \frac{1}{24}\left[\chi^{[n]}(SA_1)+\chi^{[n]}(SA_2)+\chi^{[n]}(SB_1)+\chi^{[n]}(SB_2)\right]+ \\
& + & \frac{1}{6}\chi^{[n]}(O).
\end{array}$$

With these weights th "farthest" nodes $S[AB]_{[12]}$ have half the influence on the laplacian, of the "closer" nodes. Note also, that the sum of the weights is one.

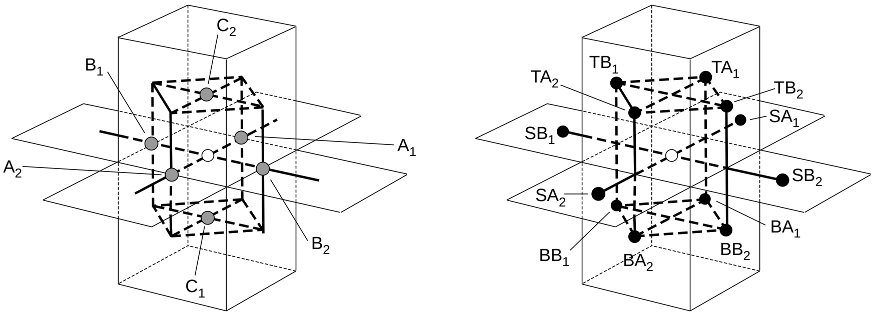

Figure 14. The averaging kernel for the laplace's equation on 3D staggered mesh (right) and the motivation for it (left). For example, the stencil for a face with normal vector $\hat{\mathbf{z}}$ would include five "$\hat{\mathbf{z}}$ faces" (including itself), four "$\hat{\mathbf{x}}$ faces" and four "$\hat{\mathbf{y}}$ faces" (two of each above and below).

Boundary Conditions

Boundary conditions (given by Equation (2.5)) in the staggered mesh are particularly easy if one assumes that the boundary surface passes *inside* of boundary voxels, rather than on their sides. Suppose, for example, that the boundary plane normal to $\hat{\mathbf{z}}$ passes through the center of the voxel v_{ijk}. Then the BC for this voxel would be that $B_z\left(i,j,k\right)=0$, or simply $\chi\left(i,j,k+\frac{1}{2}\right)=\chi\left(i,j,k-\frac{1}{2}\right)$.

To motivate such choice of the boundary, we note that boundary voxels, by definition, are the voxels *part of which is inside of $\mathcal{D}$ while part is outside.* Such a conclusion is made about voxels, some of whose corners are inside of $\mathcal{D}$, and some of the corners are outside of $\mathcal{D}$ (this information about the domain is obtained in the optional last step of the algorithm, described in section 2.3.1). We approximate the boundary inside of each boundary voxel as a plane, that passes through the center of the voxel and that separates its "exterior" part from its "interior" part. Such approximation will err by no more that $1/\sqrt{2}$ voxel's length off the real location of the boundary. We also find it easier to work in terms of faces rather than corners, since this is where χ is defined. (We say, that a face is "exterior" to the domain if more than two of its corners are not in the domain, i.e., for a voxel, we say, that if only one corner or only one edge are "exterior", we do not consider it subject to BC's).

There are several ways to orient such a boundary plane inside a voxel, based on the behavior of the boundary in the immediate surrounding of the voxel.

1. The voxel has only one face outside of the domain. Then we consider the boundary parallel to that face of the voxel (see Figure 15, left). If, say, the boundary is parallel to the face between faces A and A_1 (see Figure 15, bottom left), then the normal field to the boundary is $\mathbf{B}\cdot\widehat{\mathbf{AA_1}}$ (hereafter $\widehat{\mathbf{AA_1}}$ denotes a unit vector along the line from A to A_1, which might be $\pm\hat{\mathbf{x}}$, $\pm\hat{\mathbf{y}}$ or $\pm\hat{\mathbf{z}}$), and BC would be formulated as

   $$\chi_A = 1\cdot\chi_{A_1} + 0\cdot\chi_{B_1} + 0\cdot\chi_{C_1}\ .$$

2. The voxel has two adjacent faces outside of the domain. Then we approximate the boundary as a plane, that cuts off these two faces, as shown in Figure 15, middle. If faces A and B are outside and faces A_1 and B_1 are inside of the domain, then we consider the normal field to be $\mathbf{B}\cdot\frac{1}{\sqrt{2}}\left(\widehat{\mathbf{AA_1}}+\widehat{\mathbf{BB_1}}\right)$ and set BC's as

   $$\begin{array}{rcl} \chi_A &=& 0\cdot\chi_{A_1} + 1\cdot\chi_{B_1} + 0\cdot\chi_{C_1},\\ \chi_B &=& 1\cdot\chi_{A_1} + 0\cdot\chi_{B_1} + 0\cdot\chi_{C_1}. \end{array}$$

3. Similarly, if three mutually adjacent faces of the voxel are outside of the domain (and three others are inside), as shown in Figure 15, right, then, analogously, we assume that the normal field is $\mathbf{B}\cdot\frac{1}{\sqrt{3}}\left(\widehat{\mathbf{AA_1}}+\widehat{\mathbf{BB_1}}+\widehat{\mathbf{CC_1}}\right)$ and BC's could be set in the following way:

   $$\begin{array}{rcl} \chi_A &=& 0\cdot\chi_{A_1} + \frac{1}{2}\cdot\chi_{B_1} + \frac{1}{2}\cdot\chi_{C_1},\\ \chi_B &=& \frac{1}{2}\cdot\chi_{A_1} + 0\cdot\chi_{B_1} + \frac{1}{2}\cdot\chi_{C_1},\\ \chi_C &=& \frac{1}{2}\cdot\chi_{A_1} + \frac{1}{2}\cdot\chi_{B_1} + 0\cdot\chi_{C_1}. \end{array}$$

(Note that in this case there are really three variables and one equation to satisfy; thus, there are different solutions to χ. But each of those solutions would be valid, as long as it satisfies $\mathbf{B} \cdot \hat{\mathbf{n}} = 0$.)

4. “Everything else”: the voxel has three or more non-adjacent faces that are outside of the domain, but still is on the boundary. It is considered an extraneous voxel and is removed from the boundary.

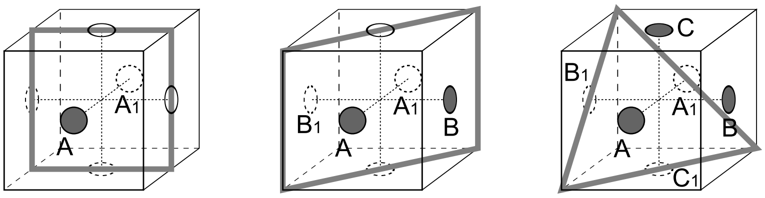

Figure 15. Different ways to approximate the boundary surface inside of a boundary voxel, depending on which portion of the voxel is found to be outside of the domain. White dots are the centers of the “interior” faces, gray dots are the centers of the “exterior” faces (see explanation in the text), the thick plane is the proposed approximation of the boundary surface $\partial\mathcal{D}$.

2.4. The Experiment

The method described above was tested on a simple quadrupole example, and the values of self-helicity it gives are in a good agreement with theoretical predictions [Longcope & Malanushenko, 2008]. That work, however, does not consider any sort of stable equilibrium and does not study any kinking instability thresholds, similar to those developed in [Hood & Priest, 1981].

The objective of the current work is to test whether the parameter H_A/Φ^2 behaves like a total twist in the sense that it has a critical value above which a system is unstable to a global disruption. To do so, we use the numerical simulation of kink instability in an emerging flux tube from [Fan & Gibson, 2003].

2.4.1. Simulation Data

The initial configuration is a linear arcade above the photosphere, into which a thick, non-force-free torus was emerged. Inside the torus the field lines wind around its minor axis and the field magnitude drops with distance from the minor axis. The exact shape of the magnetic field, in the coordinates shown on Figure 16, is the following:

$$\mathbf{B}_0 = B_\psi \hat{\boldsymbol{\psi}} + B_\varphi \hat{\boldsymbol{\varphi}} = B_t e^{-\varpi^2/a^2} \left(q \frac{\varpi}{\rho} \hat{\boldsymbol{\psi}} + \frac{a}{\rho} \hat{\boldsymbol{\varphi}} \right), \tag{2.6}$$

where $a = 0.1L$ is the minor radius, $R = 0.375L$ is the major radius, $q = -1$, $B_t = 9B_0$, L is the length scale of the domain (further in our calculations $L = 1$), B_0 is the characteristic strength of the photospheric arcade the torus is emerging into, and the time is given in the units of Alfven time, $\tau_A = L/v_A$. The field strength drops as $e^{-\varpi^2/a^2}$ with ϖ being the distance from the minor axis. At $\varpi = 3a$ magnetic field was artificially set to 0.

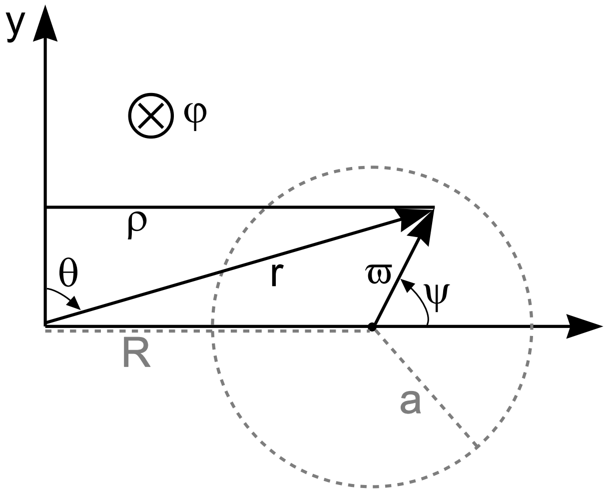

Figure 16. **B** is set in spherical coordinates (r, θ, ϕ) with the polar axis directed along $\hat{\mathbf{y}}$. We will mainly use different coordinates, namely, (ϖ, ψ, ϕ). R is the major radius of the torus, a is the minor one, $\rho = r\sin(\theta)$ is the distance from the y axis.

The torus is "emerged" from underneath the photosphere with a constant speed. There is a mass flow across the photosphere in the area, and the emerging tube is driven into the domain by an electric field at the boundary. This is made in the following way: for each time step (starting at t=0 and until the axis of the torus has emerged, t=54) the vertical photospheric field is set to that from the appropriate slice of the torus's field. Dynamical equations are then solved in order for the field above $z = 0$ to relax, so that at every time step the resulting configuration is a force-free equilibrium. The unsigned photospheric flux as a function of time is shown in Figure 17.

A visual representation of characteristic times is shown on Figure 18. Different rows correspond to different times: $t = 15$ – the tube is about to emerge; $t = 24$ – the minor axis of the torus has emerged; $t = 32$ – the bottom of the torus has emerged;

$t = 45$ – the tube undergoes acceleration; $t = 54$ – the major axis of the torus has emerged, the torus has stopped emerging, the tube starts getting a significant writhe; $t = 58$ – the tube escapes the domain; the simulation is over. Note that the torus starts to kink at $t \geq 45$ and keeps kinking until it escapes the computational domain at $t = 58$.

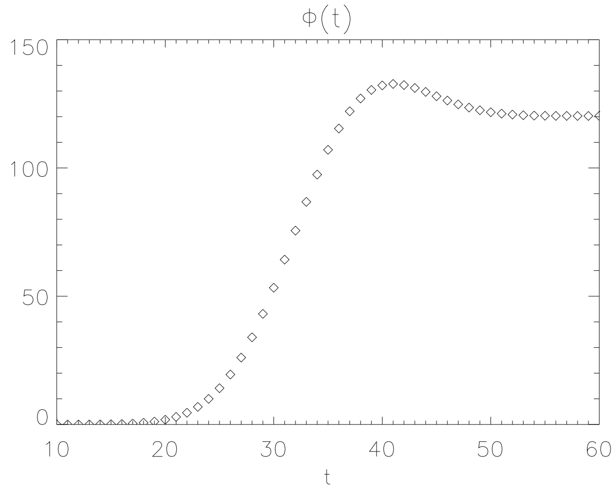

Figure 17. The total amount of unsigned photospheric flux, as defined in Equation (2.4), of the torus (not counting the arcade), plotted as a function of time. The major axis of the torus emerges at $t = 54$. The maximal value of flux is reached earlier than that because of the field winding aroung the torus and thus being not necessarily normal to $\hat{\mathbf{z}}$. After $t = 54$ the torus has stopped emerging and thus the magnetic field at the photosphere remains constant.

2.4.2. Computing H_A For Given Volume And The Potential Field.

We define different domains, $\mathcal{D}$, with the same field, by making different choices of boundary mask. We were interested in how different portions of the torus, namely,

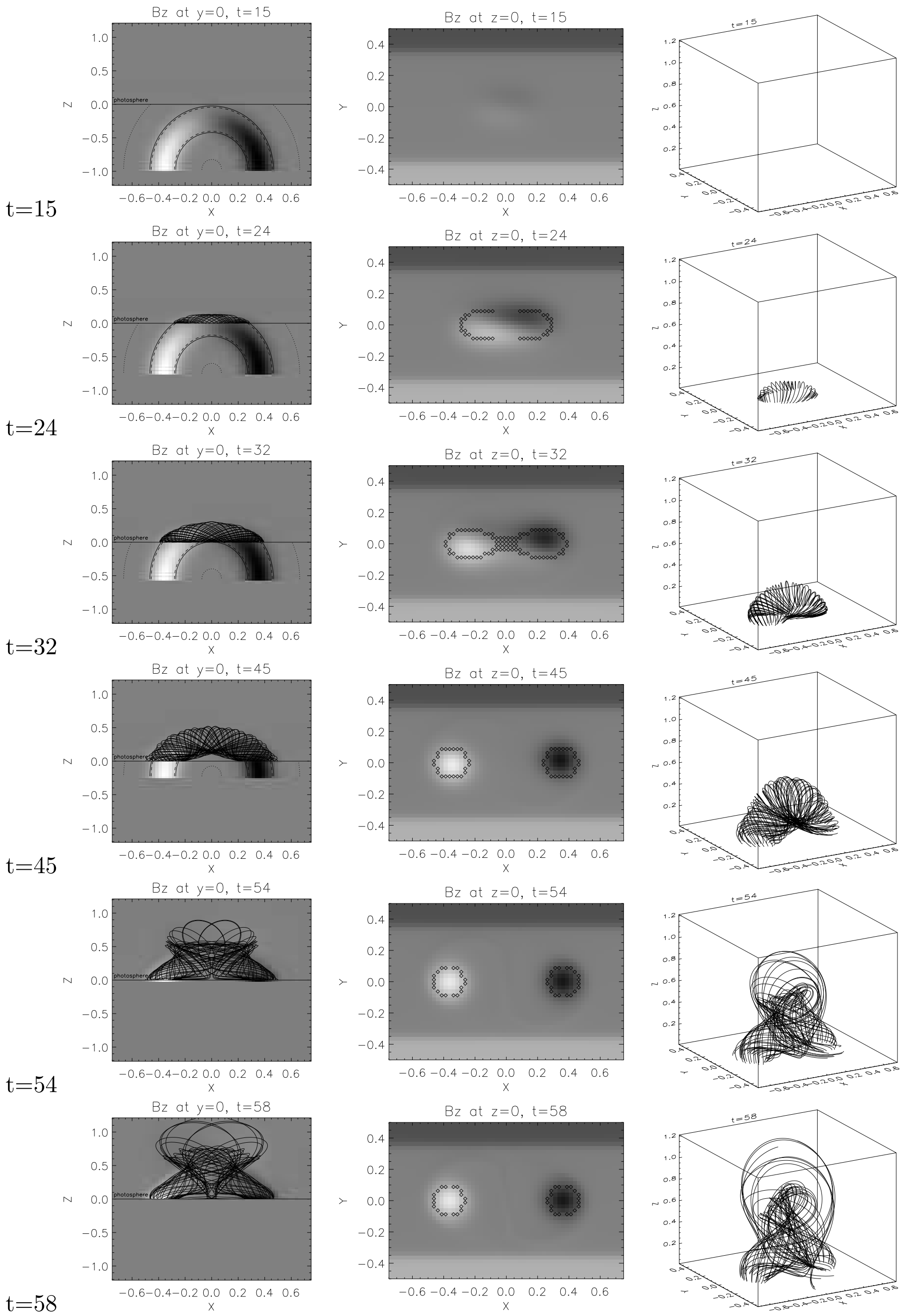

Figure 18. The characteristic times for the simulation of Fan & Gibson, 2003, different rows correspond to different time (see detailed explanation in text). *First column* – XZ slices, the analytical shape of the rising tube is shown beyond the photosphere, solid-dashed line is $\varpi = 1.0$ – the formal "edge" of the torus; dotted line is $\varpi = 3.0$. *Second column* – magnetograms at $z = 0$. *Third column* – side view of the field lines, initiated at $\varpi = 1.0$ (their footpoints are shown as diamonds in the second column).

the "core" and the outer layers behave during the instability.

Our masks are defined to be within the photospheric intersection of the emerging torus, $\varpi \leq \varpi_{max}$. By choosing different values of ϖ_{max} we construct domains, containing different portions of the emerging flux tube. The footpoints of domains with different ϖ_{max} are shown in Figure 19. The shape is distorted with respect to the original cross-section of a torus due to reconnection with the arcade, current sheet formation and due to near horizontality of some field lines.

We found domains for masks with $\varpi_{max} \in [0.5, 1.0, 2.0]\, R$ at different times during the emergence. We computed $\Theta\left(\varpi_{max}, t\right)$ and then constructed a potential field confined to it. The results are shown in Figures 19, 20 and 21.

For each t and ϖ_{max} we calculated vector potentials of the actual field, $\Theta\left(t, \varpi_{max}\right)\mathbf{B}\left(\mathbf{r}, t\right)$, and the reference field $\mathbf{B}_P\left(\mathbf{r}, t, \varpi_{max}\right)$. To do this we used a gauge in which one of the components of the vector potential (in our case, A_z) is identically zero. The other two could be found with a straight-forward computation:

$$\begin{aligned} A_x(x,y,z) &= \int\limits_0^z B_y(x,y,z')dz' \\ A_y(x,y,z) &= f(x,y) - \int\limits_0^z B_x(x,y,z')dz' \\ f(x,y) &= \int\limits_0^x B_z(x',y,0)dx' \end{aligned} \tag{2.7}$$

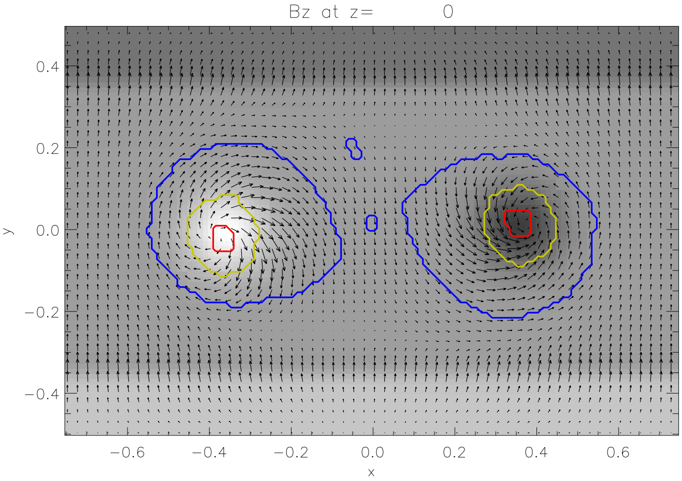

Figure 19. An example of footpoints of domains $\Theta\left(\varpi_{max} \in [0.5, 1.0, 2.0], t = 50\right)$. The vertical field, B_z, is shown in grayscale and horizontal field is shown with arrows. Three pairs of concentric curves, counting from inside out enclose footpoints of the domains defined by $\varpi_{max} = 0.5$, $\varpi_{max} = 1.0$ and $\varpi_{max} = 2.0$.

In terms of these elements the additive self helicity the additive self-helicity:

$$H_A\left(t, \varpi_{max}\right) = \int\limits_{\Theta(t,\varpi_{max})} \left(\Theta\mathbf{B} - \mathbf{B}_P\right) \cdot \left(A + A_P\right) dV \tag{2.8}$$

is computed.

2.4.3. Measuring Twist in Thin Flux Tube Approximation

To make contact with previous work we compare the additive self helicity to the twist helicity in our flux bundles. It can be shown analytically that in the limit of a vanishingly thin flux tube these quantities are identical. Here we must compute twist helicity for flux bundles of non-vanishing width. We do this in terms of a geometrical twist related to twist helicity.

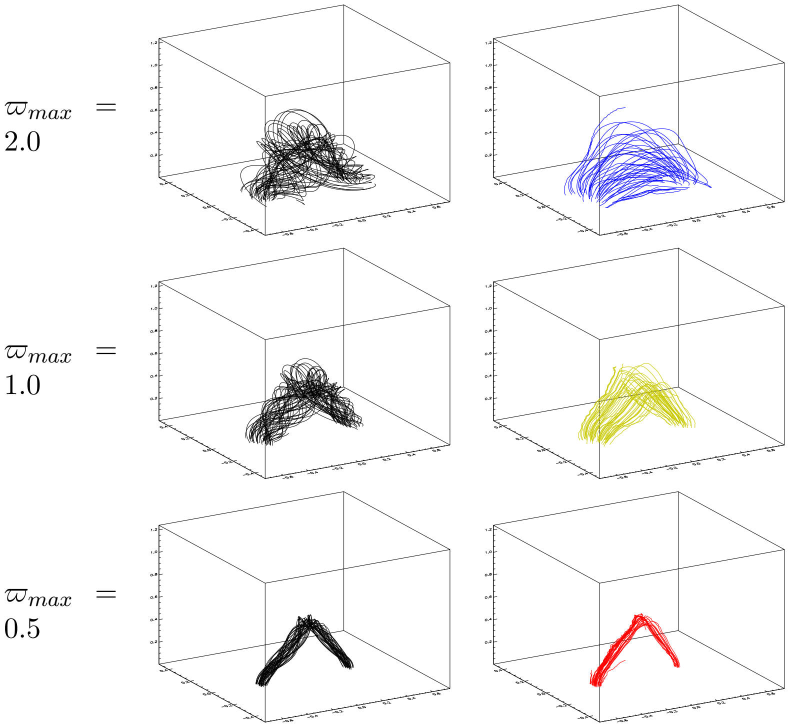

Figure 20. *(left column)* – field of a torus, confined to domains of different ϖ_{max}, with footpoints shown in Figure 19. *(right column)* – the potential field, constructed for each such domain.

One cannot really speak of twist, or of an axis, in the domains defined above. First, the thickness and the curvature radius of the flux bundles are comparable to their lengths. Secondly, the magnetic field and the twist vary rapidly over the cross-section of the bundle.

The domains constructed from the smaller masks, $\varpi_{max} = 0.5$ and $\varpi_{max} = 1.0$, may, however, be suitable for approximation[1] as thin tubes. Even in these cases the

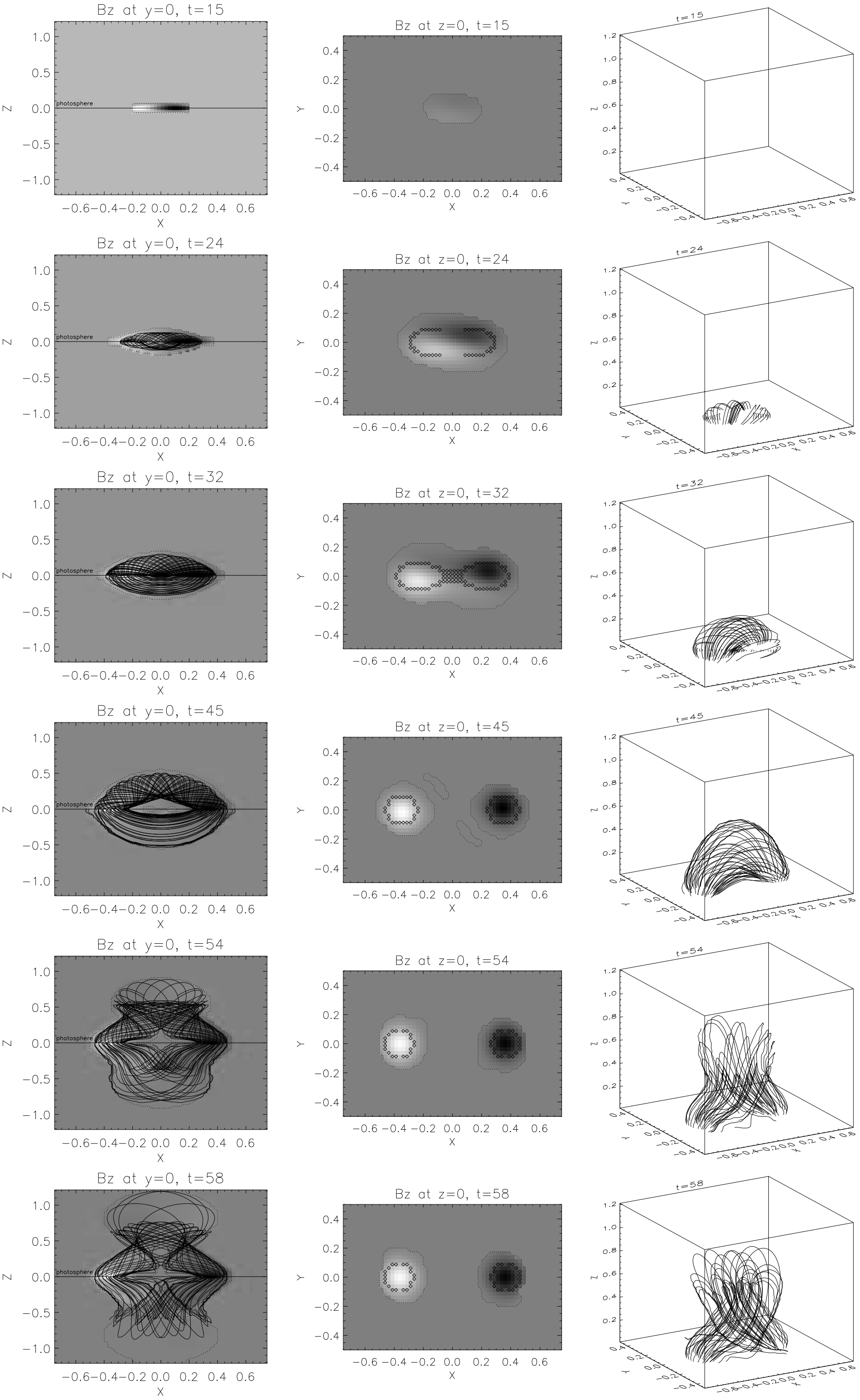

Figure 21. The strip plot of the results of the computation. The original data is shown above and the relaxed potential field $\mathbf{B}_P$ – below the photosphere. The dotted line indicates slices of the domain $\Theta\,(\varpi_{max} = 2.0)$. The magnetogram in the second column and the field lines in the third column are those of $\mathbf{B}_P$. All notation is similar to Figure 18.

approximation may suffer near the top part at later times: at $t = 50$ the radius of curvature becomes comparable to the width, and later, during kinking the radius of the tube becomes comparable to the length (see Figures 18 and 19).

We define an axis for the flux bundle by first tracing many field lines within it. Then we divide each field line into N equal segments (N is the same for all lines) of length L_i/N, where L_i is the length of the i^{th} line. If the bundle were an ideal cylinder, the midpoints of the n^{th} segment from every line would lie on a single plane; provided the bundle is thin these midpoints will lie close to a plane. We define the n^{th} point on an axis by the centroid of these approximately co-planar points. The set of N centroids forms the axis of our tube.

We then define the tangent vector $\hat{\boldsymbol{l}}_i$ along this axis, and a plane normal to this vector and thus normal to the flux tube (at least in the thin flux tube approximation). If the tube has some twist in it, then the point where one field line intersects the plane will spin about the axis as the plane moves along the tube. Such spinning must be defined relative to a reference vector on the plane which "does not spin". The net angle by which the intersection point spins, relative to the non-spinning vector, is the total twist angle of the tube. In a thin tube all field lines will spin by the small angle; in our general case we compute an average angle.

We produce a non-spinning reference vector using an orthonormal triad, arbitrarily defined at one end of the tube, and carried along the axis by *parallel transport.* For a curve with tangent unit vector $\hat{\boldsymbol{l}}$, the parallel transport of a vector $\mathbf{u}$ means $\hat{\boldsymbol{l}} \cdot (\partial \mathbf{u}/\partial l) = 0$. To impliment this numerically an arbitrary unit vector $\hat{\mathbf{u}}_0$ is chosen at one end of the axis perpendicular to the tangent, $\hat{\mathbf{u}}_0 \cdot \hat{\boldsymbol{l}}_0 = 0$. The third member of the triad is $\hat{\mathbf{v}}_0 = \hat{\mathbf{u}}_0 \times \hat{\boldsymbol{l}}_0$. At the next point, $\hat{\mathbf{u}}_1$ is chosen by projecting $\hat{\mathbf{u}}_0$ onto a plane normal to $\hat{\boldsymbol{l}}_1$ and normalizing it

$$\hat{\mathbf{u}}_1 = \frac{\hat{\mathbf{u}}_0 - \left(\hat{\mathbf{u}}_0 \cdot \hat{\boldsymbol{l}}_1\right) \hat{\boldsymbol{l}}_1}{\left|\hat{\mathbf{u}}_0 - \left(\hat{\mathbf{u}}_0 \cdot \hat{\boldsymbol{l}}_1\right) \hat{\boldsymbol{l}}_1\right|},$$

(see Figure 22). Then $\hat{\mathbf{v}}_1 = \hat{\mathbf{u}}_1 \times \hat{\boldsymbol{l}}_1$, and the procedure is repeated for every segment along the axis. Figure 23 shows an example of such vectors $\hat{\boldsymbol{l}}$, $\hat{\mathbf{u}}$ and $\hat{\mathbf{v}}$ computed along the axis of the tube at $t = 58$.

Figure 24 shows the axis of the torus and the behavior of one field line in such a nonspinning reference frame and a field line, traced from the similar location at a later time, after the tube has kinked. Both the trajectory of the field line and the total spin angle demonstrate how the thin tube twist is decreased by kinking.

2.5. Results

Based on the analogy between Tw and H_A/Φ^2, it would be natural to introduce quantity analogous to L and Wr in a similar way. We propose that L in the general (non-“thin”) case might be analogous to the *unconfined self-helicity,* introduced in [Longcope & Malanushenko, 2007] as the helicity of the field relative to a potential

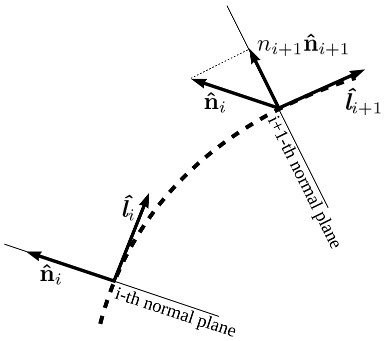

Figure 22. An illustration of parallel transport of a coordinate system. At every next step one unit vector of the previous coordinate system is projected to a new normal plane and normalized; the second vector is created anew as perpendicular to the new unit vector. $\hat{\boldsymbol{l}}$ is the tangent vector of the axis, $\hat{\mathbf{n}}$ is the unit vector in normal plane, carried with the plane along the axis.

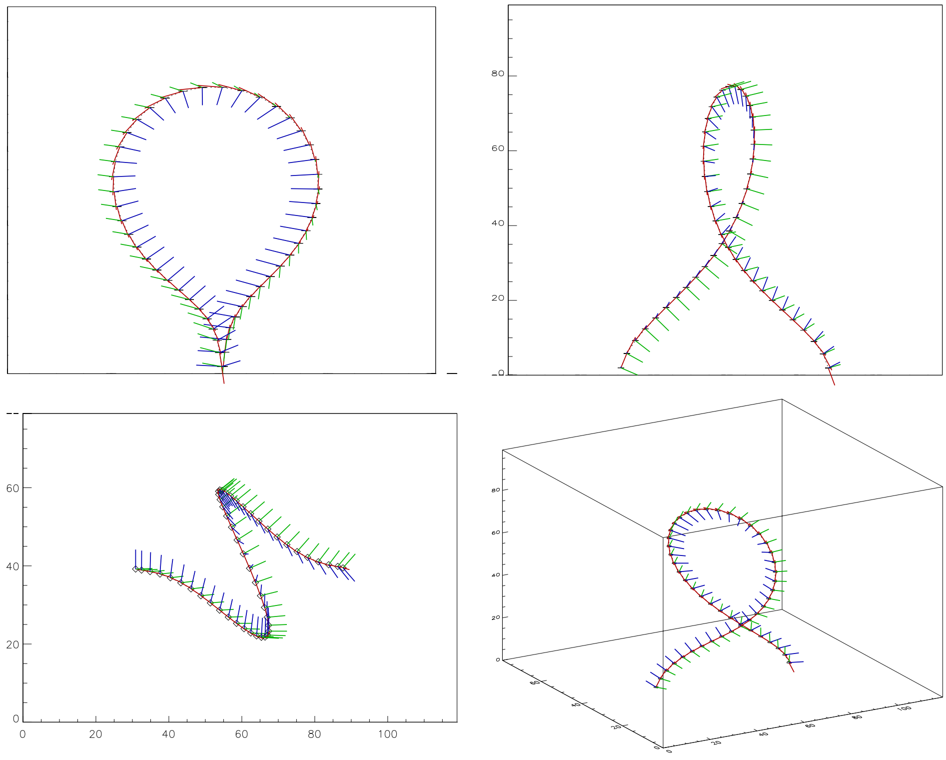

Figure 23. An example of the axis, found for $\varpi_{max} = 0.5$, $t = 58$, and the corresponding coordinate system, carried along by parallel transport. $\hat{\boldsymbol{l}}$, $\hat{\mathbf{u}}$ and $\hat{\mathbf{v}}$ are drawn in red, green and blue colors respectively.

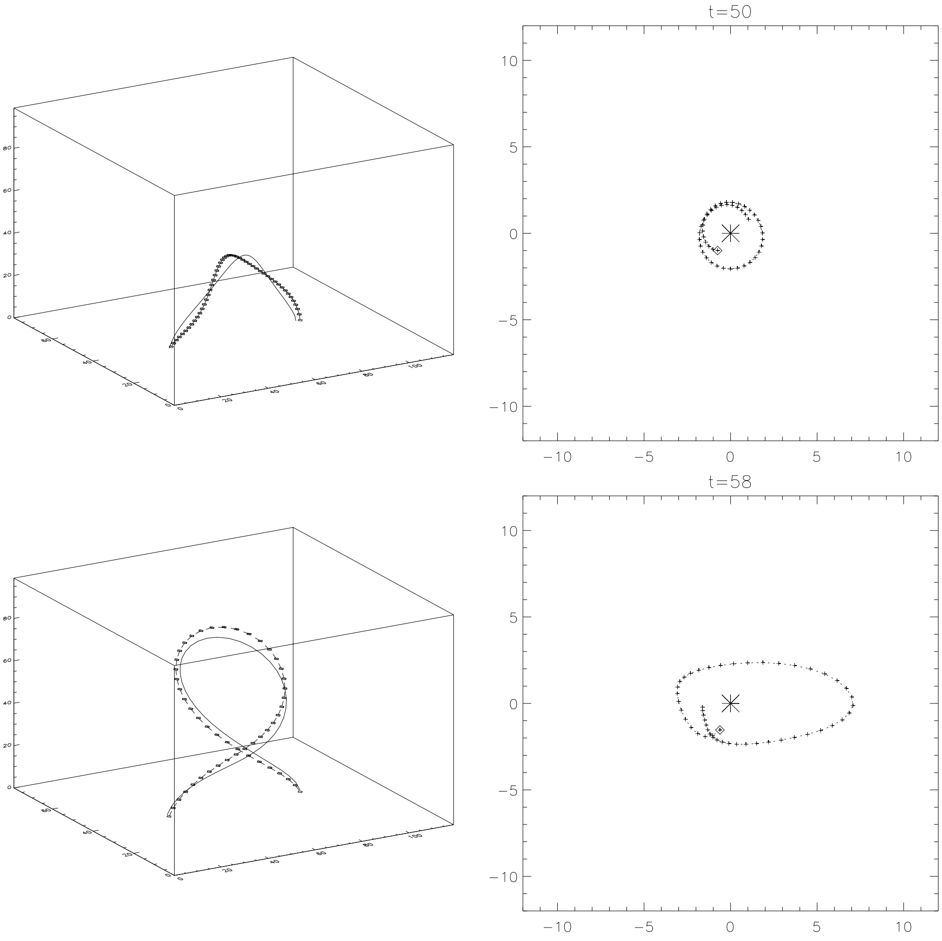

Figure 24. An illustration of how kinking decreases twist. An axis (solid) of a “thin”, $\varpi_{max} = 0.5$, tube and a single field line (dotted with diamonds) at a different times: top row is $t = 50$, the field line has $\Delta\theta \approx -3.1\pi$ and bottom row is $t = 58$ and the field line has $\Delta\theta \approx -2.4\pi$ (and $Tw = \Delta\theta/2\pi$). Left column is sideview and right column is *the trajectory of the line* in the tangent plane with coordinate system decribed above.

field filling $\mathcal{V}$ (which is constant in time and larger than $\mathcal{D}$ at all times during the evolution of the field; $\mathcal{V}$ could typically be Z_+ or a computational box), and Wr is similar to the helicity of the confined potential field relative to the unconfined potential field. From equation (3) of [Longcope & Malanushenko, 2007]

$$H(\mathbf{B},\mathbf{B}_{P,\mathcal{V}},\mathcal{V}) \equiv \int\limits_{\mathcal{V}} d^3x\mathbf{B}\cdot\mathbf{A} - \int\limits_{\mathcal{V}} d^3x\mathbf{B}_{P,\mathcal{V}}\cdot\mathbf{A}_P + \int\limits_{z=0} dxdyB_z(x,y,0)\int\limits_{\mathbf{x}_0}^{\mathbf{x}} d\mathbf{x}'\left[\mathbf{A}(\mathbf{x}')-\mathbf{A}_P(\mathbf{x}')\right] \tag{2.9}$$

(where $\mathbf{x}=\mathbf{r}(x,y,0)$ and $\mathbf{B}_{P,\mathcal{V}}$ is a potential field confined to $\mathcal{V}$ that matches boundary conditions $\mathbf{B}\cdot\hat{\mathbf{n}}|_{\partial\mathcal{V}} = \mathbf{B}_{P,\mathcal{V}}\cdot\hat{\mathbf{n}}|_{\partial\mathcal{V}}$) by plugging it into $H(\Theta_{\mathcal{D}}\mathbf{B},\mathbf{B}_{P,\mathcal{D}},\mathcal{V})$ and $H(\mathbf{B},\mathbf{B}_{P,\mathcal{V},\Theta},\mathcal{V})$ and adding them together it immediately follows, that

$$H\left(\Theta_{\mathcal{D}}\mathbf{B},\mathbf{B}_{P,\mathcal{D}},\mathcal{V}\right)+H\left(\mathbf{B}_{P,\mathcal{D}},\mathbf{B}_{P,\mathcal{V},\Theta},\mathcal{V}\right)=H\left(\Theta_{\mathcal{D}}\mathbf{B},\mathbf{B}_{P,\mathcal{V},\Theta},\mathcal{V}\right), \tag{2.10}$$

where $\mathcal{D}\subset\mathcal{V}$ and $\Theta_{\mathcal{D}}$ is a support function of $\mathcal{D}$. By $\mathbf{B}_{P,\mathcal{D}}$ we mean the potential field confined to $\mathcal{D}$ (and identically zero outside of $\mathcal{D}$) that matches boundary conditions $\mathbf{B}\cdot\hat{\mathbf{n}}|_{\partial\mathcal{D}} = \mathbf{B}_{P,\mathcal{D}}\cdot\hat{\mathbf{n}}|_{\partial\mathcal{D}}$, and by $\mathbf{B}_{P,\mathcal{V},\Theta}$ we mean the potential field, confined to $\mathcal{V}$, that matches boundary conditions $\Theta_{\mathcal{D}}\mathbf{B}\cdot\hat{\mathbf{n}}|_{\partial\mathcal{V}} = \mathbf{B}_{P,\mathcal{V},\Theta}\cdot\hat{\mathbf{n}}|_{\partial\mathcal{V}}$. As long as $\mathcal{D}$ is fully contained in $\mathcal{V}$, which is constant in time, the quantity $H_{\mathrm{unc},\mathcal{V}}/\Phi^2 \equiv H\left(\Theta_{\mathcal{D}}\mathbf{B},\mathbf{B}_{P,\mathcal{V},\Theta},\mathcal{V}\right)/\Phi^2$ will *behave like* L and $H\left(\mathbf{B}_{P,\mathcal{D}},\mathbf{B}_{P,\mathcal{V},\Theta},\mathcal{V}\right)/\Phi^2$ would then *behave like* Wr.

Figure 25 compares the generalized twist number, H_A/Φ^2, with helicity, unconfined to the flux bundle's volume, but confined to the computational domain of the simulation: $H_{\text{unc,box}}$. In this case $\mathcal{V}$ is the computational domain, a rectangular box. The behavior of all quantities matches expecation: $H_{\text{unc,box}}/\Phi^2$ increases as the torus emerges, and stays nearly constant after the emergence is complete (the slight decrease is due to the reconnection with the arcade field). The generalized twist number, H_A/Φ^2 also increases with the emergence, but decreases between $t = 50$ and $t = 58$ – the time when the torus kinks (see Figure 18). For different ϖ_{max} the decrease seems to start at a slightly different time.

Figure 25 demonstrates as well, that the general behavior of $H_{\text{unc},\mathcal{V}}/\Phi^2$ is qualitatively similar whether the volume $\mathcal{V}$ over which unconfined helicity is computed is the computational domain or the half space. To compute the unconfined helicity in the half space, $H_{\text{unc,Z}_+}$, we integrate the helicity flux in the way described in [DeVore, 2000] and used in [Fan & Gibson, 2004]. The helicity flux is computed relative to the potential field in half space, and thus, the helicity flux, obtained in this way, might be considered "confined to a half space".

Longcope and Malanushenko (2008) show that $H_{\text{unc,box}} = H_{\text{unc,Z}_+}$ when the volumes, $\mathcal{V}$ and Z_+ and the vertical field, $B_z(z = 0)$, all share a reflectional symmetry. This situation occurs in the simulation only for $t \geq 54$ when the torus is fully emerged and its major axis is at the photosphere. At these times the vertical component of the field is the toroidal component of the torus, which is symmetric about $y = 0$. Due to reconnection with the arcade, however, the footpoints of $\mathcal{D}$ may not share this symmetry, in which case the photospheric field $\Theta_{\mathcal{D}} B_z$ is not precisely symmetric. If the two helicities were ever to coincide, it would be at $t = 54$, so we choose constant of integration by setting $H_{\mathrm{unc,box}} = H_{\mathrm{unc,Z_+}}$ at that time. The time histories of both unconfined helicities are plotted in Figure 25. The discrepancy between the two before $t = 54$ arises from the non-vanishing helicity of $\mathbf{B}_{P,\mathcal{V},\Theta}$ relative $\mathbf{B}_{P,Z_+,\Theta}$ owing to a photospheric field, B_z, lacking reflectional symmetry. In spite of the discrepancy, we draw from each curve the same basic conclusion, that the kink deformation of $\mathcal{D}$ does not change $H_{unc,\mathcal{V}}$.

Figure 26 compares the generalized twist number to the traditional twist number described above. The twist number was computed only for the thinner subvolumes of the torus, $\varpi_{max} = 0.5R$ nd $\varpi_{max} = R$. Figure 26 shows agreement quite well for $\varpi_{max} = R$ and less well for $\varpi_{max} = 0.5R$. The reason might be the following: the smaller the subvolume, the fewer points does it have, so that, first, there are fewer field lines to be traced to measure twist, and second, the potential field, obtained by relaxation is numerically less precise. Nevertheless, the magnitudes and the general behaviors do agree.

Figure 26 also shows the twist number measured for the potential field in a subvolume $\mathbf{B}_P$, is zero to measurement error. Note, that a significant portion of the torus is emerged, its length is not large enough (relative to the thickness) for the thin tube

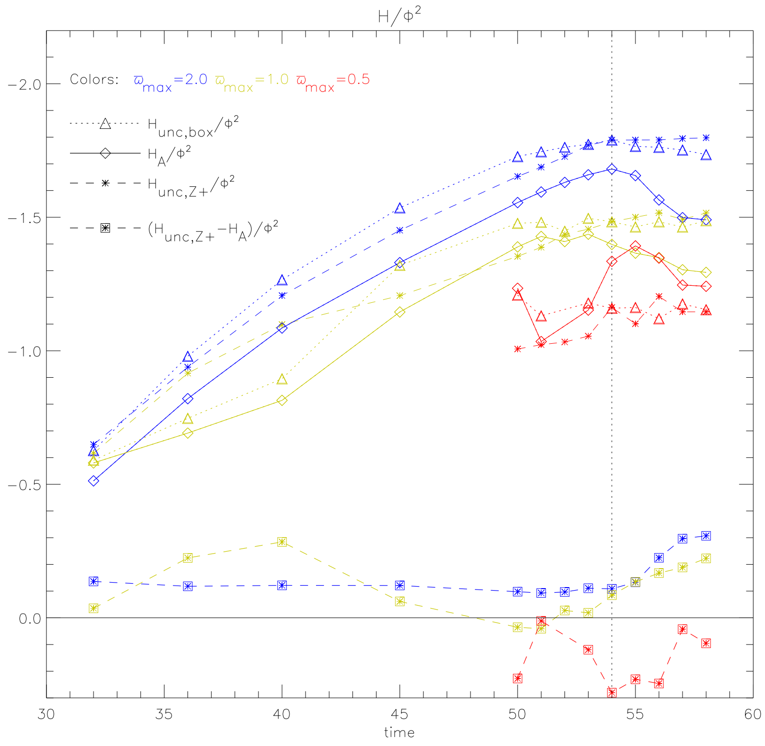

Figure 25. The comparison between H_A (i.e., confined to the volume of the flux tube), $H_{\mathrm{unc,box}}$ (confined to the box in which the original simulation was performed) and $H_{\mathrm{unc,Z_+}}$ (confined to half-space), normalized by Φ^2. Vertical dashed line at $t = 54$ indicates the time when the emergence has stopped and *all* further changes in Tw would be due to kinking and numerical diffusion, and all earlier changes are altered by the emergence of the tube and thus non-zero helicity flux over the surface. For ϖ_{max} of 2.0 and 1.0 it's clearly visible, that: a) after $t = 54$ the unconfined helicities remain nearly constant, while the confined to flux bundle's $\mathcal{D}$, that is, additive self helicity, decreases due to kinking; b) before $t = 54$ the difference between $H_{\mathrm{unc,Z_+}}$, that is, the integrated helicity flux, and $H_{\mathrm{unc,box}}$ is non-zero. The threshold for H_A/Φ^2 seems to be -1.7 for $\varpi_{max} = 2.0$ and -1.4 for $\varpi_{max} = 1.0$. $\varpi_{max} = 0.5$ seems to be too noisy to draw a reliable conclusions; possible reasons for that are discussed in the text.

approximation to be valid. As the twist of the potential field should theoretically be zero (as well as generalized twist), this plot also gives an idea of the magnitude of the error of twist measurements; at most times the error is less than 15% of the value.

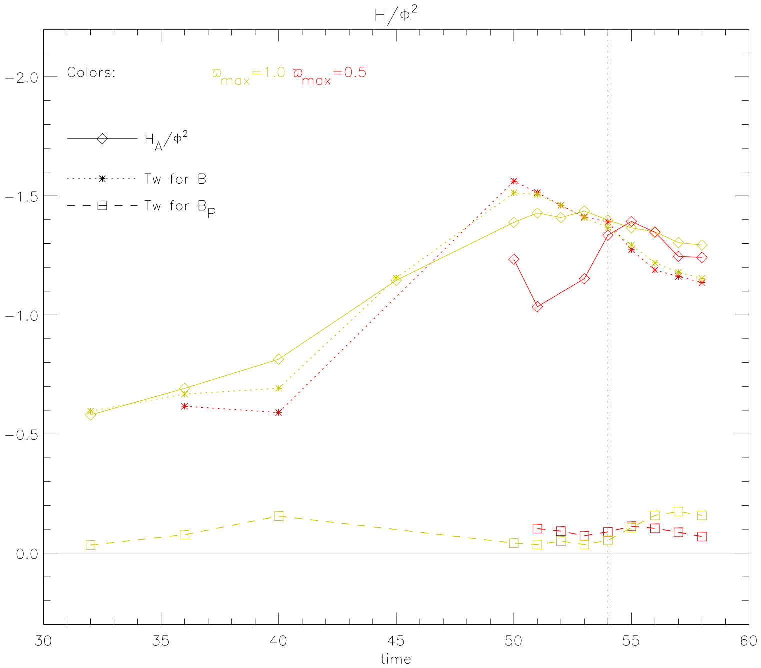

Figure 26. A comparison between generalized twist number (solid line with diamonds) and the “thin tube” classical twist number (dotted line with asterisks) for two subvolumes of a different size. Also, the “classical” twist number for a potential field (dashed line with squares).

2.6. Discussion

We have demonstrated that, at least in one MHD simulation, the quantity, $Tw_{(gen)}$, defined in terms of the additive self helicity shows a threshold beyond which the system became dynamically unstable. The simulation we considered, originally studied by [Fan & Gibson, 2003], is a three-dimensional, numerical solution of the time-dependent, non-linear evolution of an emerging flux system. The original study established that the system became unstable to a current-driven (kink) mode at some point during its evolution. In this work we have shown that the quantity $Tw_{(gen)}$ increases until the instability ($Tw_{(gen)} \simeq 1.5$) at which time it drops. This drop occurs as a natural consequence of the instability itself.

The quantity we propose as having a threshold, $Tw_{(gen)}$, is computed using a version of the self helicity previous defined by [Longcope & Malanushenko, 2008]. The present work has provided a detailed method for computing this quantity for any complex bundle of field lines within a magnetic field known on a computational grid. We also demonstrate that for the very special cases when that bundle can be approximated as a thin flux tube, $Tw_{(gen)}$ is approximately equal to the traditional twist number, Tw. In the case of thin flux tubes which are also dynamically isolated, free magnetic energy is proportional to $(Tw)^2$. Their free energy may be spontaneously reduced if and when it becomes possible to reduce the magnitude of Tw at the expense of the writhe number, Wr, of the tube's axis.

All this supports the hypothesis that $Tw_{(gen)}$ could be treated as a generalization of Tw. Such a generalization might be extremely useful in predicting the stability of magnetic equilibria sufficiently complex that they cannot be approximated as thin flux tubes. The case we studied, of a thick, twisted torus of field lines

[Fan & Gibson, 2003], appears to become unstable when $Tw_{(gen)}$ exceeds a threshold value between 1.4 and 1.7. This value happens to be similar to the threshold on Tw for uniformly twisted, force-free flux tubes, $Tw \approx 1.6$, as $\Delta\theta \approx 3.3\pi$ [Hood & Priest, 1979].

Previous investigations have shown that the threshold on Tw depends on details of the equilibrium such as internal current distribution [Hood & Priest, 1979]. It is reasonable to expect the same kind of dependance for any threshold on $Tw_{(gen)}$, so we cannot claim that $Tw_{(gen)} < 1.7$ for all stable magnetic field configurations. To investigate such a claim is probably intractable, but useful insights may be obtained by applying the above analysis to magnetic equilibria whose stability to the current-driven instability is already known. The paucity of closed-form, three-dimensional equilibria in the literature, and far fewer stability analyses of them, suggests this may be a substantial undertaking.

3. RECONSTRUCTING THE LOCAL TWIST OF CORONAL MAGNETIC FIELDS AND THE THREE-DIMENSIONAL SHAPE OF THE FIELD LINES FROM CORONAL LOOPS IN EUV AND X-RAY IMAGES

3.1. Abstract

Non-linear force-free fields are the most general case of force-free fields, but the hardest to model as well. There are numerous methods of computing such fields by extrapolating vector magnetograms from the photosphere, but very few attempts have so far made quantitative use of coronal morphology. We present a method to make such quantitative use of X-Ray and EUV images of coronal loops. Each individual loop is fit to a field line of a linear force-free field, allowing the estimation of the field line's twist, three-dimensional geometry and the field strength along it.

We assess the validity of such a reconstruction since the actual corona is probably not a linear force-free field and that the superposition of linear force-free fields is generally not itself a force-free field. To do so, we perform a series of tests on non-linear force-free fields, described in [Low & Lou, 1990]. For model loops we project field lines onto the photosphere. We compare several results of the method with the original field, in particular the three-dimensional loop shapes, local twist (coronal α), distribution of twist in the model photosphere and strength of the magnetic field. We find that, (i) for these trial fields, the method reconstructs twist with mean absolute deviation of at most 15% of the range of photospheric twist, (ii) that heights of the loops are reconstructed with mean absolute deviation of at most 5% of the range of

trial heights and (iii) that the magnitude of non-potential contribution to photospheric field is reconstructed with mean absolute deviation of at most 10% of the maximal value.

3.2. Introduction

Most active region coronal magnetic fields are believed to be in a force-free state,

$$\nabla \times \mathbf{B} = \alpha(\mathbf{r})\mathbf{B}, \tag{3.1}$$

where α is a scalar of proportionality, e.g., [Nakagawa et al., 1971]. It turns out that α is closely related to the local twist of magnetic field lines. For example, in a cylindrical uniformly-twisted flux tube, field lines twist about the axis by an angle $\theta = \frac{1}{2}\alpha L$ over axial distance L [Aschwanden, 2006].

If α varies in space, a solution of Equation (3.1) is called a non-linear force-free field, as it solves a non-linear system of equations for different components of $\mathbf{B}$ and the scalar α. [Demoulin et al., 1997] described basic problems arising when trying to solve these equations. In particular, the existence and uniqueness of a solution is not entirely clear. Another difficulty is the fact that the only source of boundary conditions available at the moment are vector magnetograms measuring the field within the non-force-free photospheric layer.

A particular case of a force-free field, called a linear force-free field, or a constant-α field, occurs when $\nabla\alpha = 0$. In this case, using $\nabla \cdot \mathbf{B} = 0$, Equation (3.1) is transformed to a Helmholtz equation for $\mathbf{B}$. This is much easier to solve and the conditions for existence and uniqueness of solution are known. Nor does the solution require vector magnetogram data, but only a line-of-sight magnetogram and a value of the constant α. This boundary condition is affected less by the fact that the photosphere is probably not force-free. There are many methods of solving for linear force-free fields, e.g., [Nakagawa & Raadu, 1972, Chiu & Hilton, 1977, Altschuler & Newkirk, 1969, Lothian & Browning, 1995, Alissandrakis, 1981]. In particular, we will use the Green's function method, described in [Chiu & Hilton, 1977], as it does not place any restrictions on α and it generates a field over an entire half-space, without boundaries.

While they are simpler to generate, linear force-free fields have proven insufficient to model complex geometries of the solar corona. Observations of curvature of Hα structures, visual studies of twist in coronal loops, and estimations of local twist at the photospheric level via vector magnetograms reveal active regions with spatially varying twist, and even varying sign of twist, for example, [Burnette et al., 2004, Nakagawa & Raadu, 1972]. In light of this any constant-α approximation would appear to be, strictly speaking, incorrect. Over the past decade there have been many attempts to perform extrapolations of non-linear force-free magnetic field into the corona and to assess the quality of the extrapolation by comparing lines of the resulting field to coronal loops, e.g., [Schrijver et al., 2008, DeRosa et al., 2009] and references therein.

In the current work we apply a completely different approach. We use the visible shapes of coronal loops to infer the twist of the magnetic field. Instead of measuring twist in the photosphere, where Equation (3.1) is not appropriate, we *perform measurements in the region of interest*, in the low-β force-free solar corona. The method thus relies solely on EUV or X-Ray images of coronal loops and on line-of-sight magnetograms.

The basic idea is to try to approximate every visible coronal loop with a field line from a linear force-free field, and allow α to be different for every loop. Even for non-linear force-free fields, α must be constant along each field line[1]. If α changes smoothly then it would be reasonable to expect that α is nearly constant in the vicinity of a given field line. Of course, a superposition of constant-α fields would not in general be a force-free field and at first sight such a method could not be expected to yield meaningful results. In the next few paragraphs we argue that such a method might work under certain circumstances relevant to the solar corona. Within the core of this work we support the hypothesis with tests first using analytic non-linear force-free fields and then with solar data.

Our method is similar to the ones proposed by [Green et. al., 2002] and [Lim et. al., 2007], however, with several important advantages. First, it does not require the full length of a coronal loop to be visible for a successful reconstruction. Second, it does not require either of the footpoints to be visible. Third, it allows the user to draw

---

[1] This result is obtained by taking the divergence of both sides of Equation (3.1) and using $\nabla \cdot \mathbf{B} = 0$ and the identity $\nabla \cdot (\nabla \times \mathbf{B}) = 0$, so that $\mathbf{B} \cdot \nabla \alpha = 0$.

a smooth curve (a Bézier spline) interactively on top of the loop, rather than selecting a few points along the loop. This maximizes the amount of information taken from the coronal image. The fit itself is similar to the one used by [van Ballegooijen, 2004]; but while van Ballegooijen (2004) fits loops with lines of a particular non-linear force-free field model, we fit loops with lines of many different linear force-free fields, choosing the best α.

Consider an imaginary example of two dipoles far apart compared to their sizes. Suppose that they constitute a non-linear equilibrium, having different twist, possibly of opposite signs. Suppose, however, that within each dipole the twist is more or less constant. In such a scenario there would probably be some transition region between the dipoles where α changed significantly. Provided the dipoles are far apart we may claim that in the vicinity of the footpoints of one of them the current of the other would not significantly perturb the field, and in the close vicinity of each of them the field would be nearly a constant α field.

To support this reasoning we note that the dipolar term of a magnetic field drops as $1/r^3$ and thus the effect of a distant dipole is in general not very large compared to the nearby dipole. Indeed, this is why studying a magnetic field of an isolated region of the corona is at all meaningful.

We therefore argue that a non-linear force-free field could be considered to be linear in the regions of slowly changing α (in some sense of the term). Thus the geometry of a field in isolated regions of slowly-changing α might be approximated by the geometry of a constant-α field.

What is the limit of applicability of such an assumption? It is quite clear that it could work well for an isolated uniformly-twisted active region. Is it possible to pick a field line in an active region, and to suppose that the field's geometry is not significantly different from that of a linear field in a close vicinity of this field line? We herein conduct several experiments on both synthetic and real data which provide evidence that at least in certain cases of interest such an assumption is reasonable.

The chapter is organized in the following manner. In Section 3.3 we explicitly define the function to be minimized in order to obtain a best fit, a "distance" between two curves, d. In Section 3.4 we describe the minimization process, varying α and the line-of-sight coordinate h, and report that it indeed works in the obvious case, where the loop is a field line from an actual linear force-free field. In Section 3.5 we describe the typical features of the function $d(\alpha, h)$ and attempt to explain their appearance. In Section 3.6 we present the results of applying this procedure to several analytic non-linear force-free fields, described by [Low & Lou, 1990]. We also present an additional step proven necessary for the best fit procedure. This step amounts to minimizing $d(\alpha, h)$ in a very specific region of (α, h) parameter space. We demonstrate that this step significantly improves the results for strongly twisted fields. In Section 3.7 we demonstrate the same method applied to real data: line-of-sight magnetograms from SOHO/MDI and coronal images from Hinode/XRT. In Section 3.8 we discuss the results and their possible use in studying coronal magnetic fields.

3.3. The Distance Between Two Lines

In order to compare two curves, we seek a function quantifying the discrepancy between the curves. The ideal function would yield similar results to those obtained by visual comparison. It would be large when a human observer would consider the two lines to be far apart or unlike one another and small when a human observer would consider them to be similar and close to one another.

We use for this purpose a function first introduced by [Green et al., 2002] and later used by [Lim et al., 2007]. We apply it, however, to a different set of objects. While Green et al (2002) and Lim et al (2007) compare *a few points along the loop* to a set of field lines traced from the photosphere, *at the presumed location of the loop's footpoints*, we compare a *smooth curve*, chosen to visually match the loop, to a set of field lines traced from *different locations along the line-of-sight* at some point along the curve. The same method was used by [van Ballegooijen, 2004]. Therefore, unlike method of Lim et al (2007), our method does not require knowledge of the footpoints. In fact, it will work with even a small portion of a loop.

The *discrepancy* function is defined between two smooth curves in a plane, $\mathbf{L}_1 = \{x_1(l), y_1(l), 0 \leq l \leq L_1\}$ and $\mathbf{L}_2 = \{x_2(l), y_2(l), 0 \leq l \leq L_2\}$. For every point l on $\mathbf{L}_1$ it is possible to define a minimal distance between that point $\mathbf{L}_1(l)$ and $\mathbf{L}_2$ *in the* *classical sense*: the smallest of the distances between the point $\mathbf{L}_1(l)$ and every point along $\mathbf{L}_2$. It could also be defined as the length of the shortest perpendicular from the point $\mathbf{L}_1(l)$ to the curve $\mathbf{L}_2$, given sufficient smoothness. We will refer to this distance as $\delta(\mathbf{L}_1(l), \mathbf{L}_2)$. The discrepancy between the two curves is the average of $\delta(l)$ over curve $\mathbf{L}_1$,

$$d(\mathbf{L}_1, \mathbf{L}_2) = \frac{1}{L_1} \int\limits_0^{L_1} \delta(\mathbf{L}_1(l), \mathbf{L}_2) dl. \tag{3.2}$$

A numerical scheme to compute this integral is quite simple. Sample line $\mathbf{L}_1$ into n_1 segments with equal lengths $\Delta l_1 = L_1/n_1$. Provided the segments are small compared to the local radius of curvature, for every point on $\mathbf{L}_1$,

$$\delta(\mathbf{L}_1(l_i), \mathbf{L}_2) = \min\left(\sqrt{(x_1(l_i) - x_2)^2 + (y_1(l_i) - y_2)^2} \,\middle|\, (x_2, y_2) \in \mathbf{L}_2 \right). \tag{3.3}$$

The discrepancy integral can then be approximated by the sum

$$d(\mathbf{L}_1, \mathbf{L}_2) = \frac{\Delta l_1}{L_1} \sum_{i=0}^{n_1} \delta(\mathbf{L}_1(l_i), \mathbf{L}_2), \tag{3.4}$$

representing the mean distance between points of one curve and the whole second curve; it has the units of length.

The trivial properties of the discrepancy function $d(\mathbf{L}_1, \mathbf{L}_2)$ are, first, that it is non-negative and second, it is non-commmutative, meaning $d(\mathbf{L}_1, \mathbf{L}_2)$ is different in general from $d(\mathbf{L}_2, \mathbf{L}_1)$, as illustrated in Figure 27.

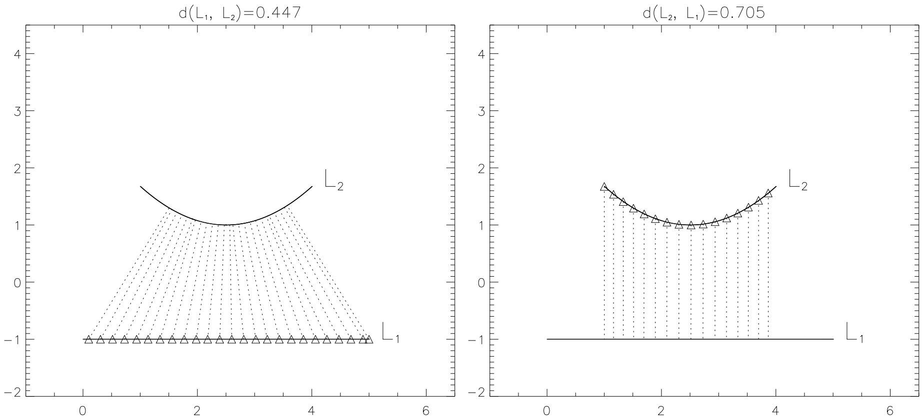

Figure 27. The discrepancy between the two lines. The left panel illustrates the calculation of $d(\mathbf{L}_1, \mathbf{L}_2)$ and the right shows $d(\mathbf{L}_2, \mathbf{L}_1)$. For each point on the first curve (the first argument of d), denoted by a triangle, one finds the closest point on the second curve (the second argument). The closest distance is shown as a dashed line. The net discrepancy is the average of all such distances. Comparison of the two panels illustrates that the discrepancy is non-commutative.

3.4. α-h-fit

For a visible coronal loop it is possible to construct a smooth two-dimensional curve $\mathbf{L}_0$ in the plane of the sky visually approximating the loop, or some portion of the loop. The loop is really a three-dimensional structure and for every point on $\mathbf{L}_0$, the third coordinate, i.e. along the line of sight (LOS), is unknown. If the loop is at disk center, then the LOS coordinate is the height above the photosphere. For simplicity in notation, we will thereafter refer to this coordinate as “height”, denoted h, even when it is not vertical.

The main idea of what we call an *h-fit* is to choose a point l_0 on the loop $\mathbf{L}_0$ and *prescribe* a certain height. Then, if the magnetic model is known, trace a field line from the three-dimensional location $(L_{0x}(l_0), L_{0y}(l_0), h)$ and compare its plane of the sky projection $\mathbf{L}(h)$ to the original loop by calculating $d(h) = d(\mathbf{L}_0, \mathbf{L}(h))$. Finally, we vary h to find the minimum of $d(h)$.

To illustrate this method we construct a synthetic magnetogram and generate a magnetic field (the potential field of a magnetic quadrupole in half-space Z_+). As a model of the ‘loop’ we take an actual field line, projected onto the x–y plane. We then take the mid-point of the projected loop, $\mathbf{L}_0(\frac{1}{2}L_0)$, and trace field lines at different heights (see Figure 28). Figure 29 shows the function $d(h)$ with one minimum at the actual height, to within one step of the h search.

Suppose now that the coronal magnetic field is not known, but belongs to a known family of magnetic fields, described by certain parameters. It is then possible to do fitting not only in height, but also in the space of these magnetic field parameters. For example, if there is a reason to believe that the actual field is constant-α , but with unknown α, then the discrepancy is a function of both α and h, $d = d(\alpha, h)$ and the minimization must be done over (α, h) space.

To illustrate such a minimization we perform the following experiment. From the quadrupolar magnetogram of Figure 28 we extrapolated a constant-α field into the corona (Z_+). We produced several such fields with different values of α. For each of these fields we selected several magnetic field lines at random, which we projected onto x–y plane. We then treated these projections as synthetic loops and performed an $\alpha - h$ fit. Provided the method works, the best-match α should have one-to-one correspondence with the real α for each field line.

The constant-α fields were generated using Green's function [Chiu & Hilton, 1977] for a field in a half-space. This has the advantage that it places no limitations on α, whereas Fourier methods using periodic images separated by L, require $|\alpha| < \frac{2\pi}{L}$ [Nakagawa et al., 1971]. In Section 3.6 we demonstrate that our method can reconstruct values of $|\alpha|$ up to $\frac{\pi}{h}$, where the height h of *a point* (not necessarily the highest one) along the loop could be much less than the linear size of the computational domain L. For the method we propose, to perform $\alpha - h$ fit within the full region of interest, including $h < L/2$, α values larger than the maximal allowed by the Fourier method are needed.

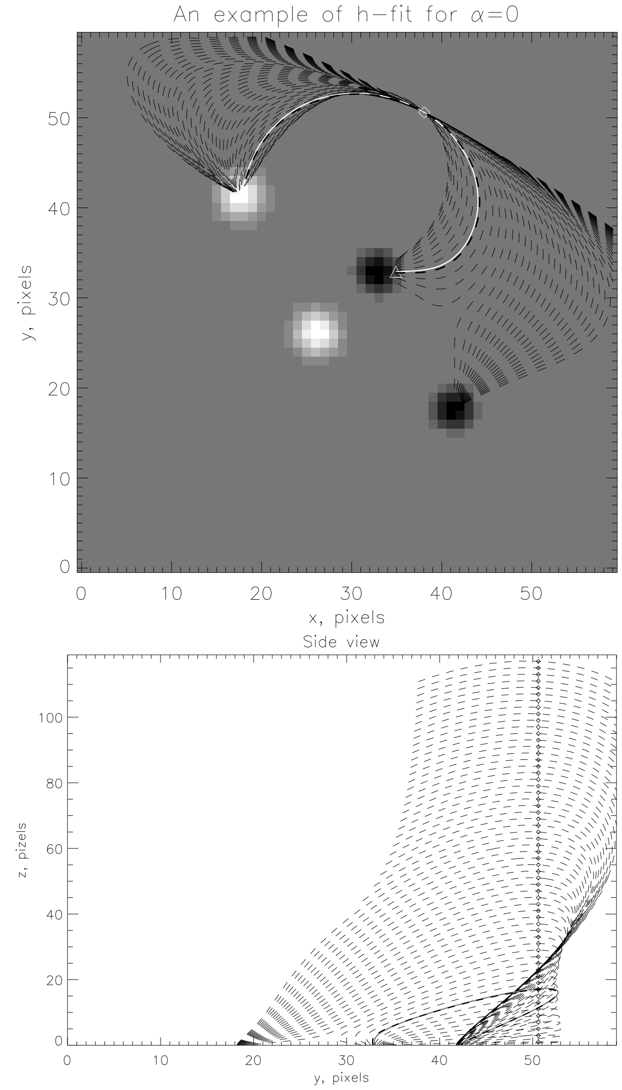

Figure 28. The synthetic example used to illustrate the *h-fitting routine*. *Top*: The synthetic magnetogram (in gray-scale) was used to generate the potential field in Z_+. One field line was selected to represent the synthetic loop (in white; its starting point is shown as the triangle). It was projected onto x–y plane and compared with field lines, traced from the points with the same (x_0, y_0) (in this case $(x_0, y_0) \approx (38, 51)$), but at different heights. These trial field lines are shown as dashed lines; they are traced for every pixel of the column $(x_0, y_0, z \in [1, n_z - 1])$. To make the plot clearer, only every second one is drawn. The point (x_0, y_0) was chosen as the mid-point of the projection of the "loop" (shown in diamond). *Bottom*: The same example, viewed in x–z projection. The initial "loop" is shown as gray, the traced field lines are shown as dashed lines, and their starting points are shown as diamonds. The thick dashed line shows the *best h-fit*.

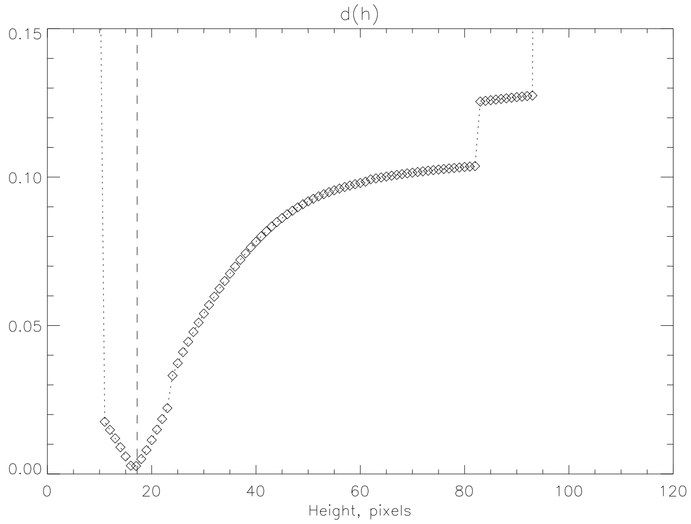

Figure 29. The function $d(h)$ has its minumum at a height $h \approx 17$ within the numerical error of the real height of the field line it is modeling. Note that for $h < 11$ pix and $h > 93$ pix the length of the projection of the traced lines is smaller than the length of the "coronal loop". Such lines could be automatically discarded from consideration, since the "loop" should be a part of a field line, and the length of a part of a curve cannot be greater than the length of the whole curve. We discard them by making $d(h)$ artificially large if the length of $\mathbf{L}_0$ is smaller than the length of $\mathbf{L}_1$.

The results of the fit show that there is indeed a strong correlation between best-match α and the real α. However, in some cases (46 points out of 689, about 7% of all field lines) the fit seems to be off by more than one step of α. We attribute these errors of the fit to several factors. One factor is the gridded search algorithm whereby we calculate $d(\alpha, h)$ for each point on a grid with fixed steps in both α and h (it is clear that a better algorithm could be implemented, however, in this work we concentrate on the theoretical possibility of the method, rather than on programming tasks). A second is that the fit is poorly constrained when a field line's shape is hidden by the projection. Finally, there are numerical errors associated with numerical integration of a field line from a field represented only on discrete grid points.

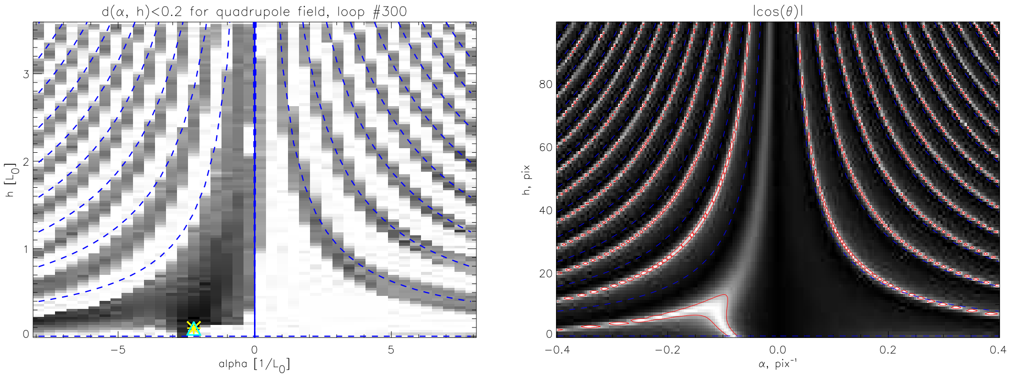

Figure 30. *(left)* – The parameter space of $d(\alpha, h)$. The yellow asterisk shows the location of the "real" (α, h) of the field line and the cyan triangle shows the "best-fit" (α, h). The blue dotted lines are hyperbolae $h = n\pi/\alpha$, $n = 0, \pm 1, \pm 2, ...$ For this field line, as for nearly all of them, the "real" minimum lies in the "branch" of local minima, that is within $-\pi/\alpha \leq h \leq \pi/\alpha$. We sped up the computation significantly by computing d only for (α, h), for which at the initial point (x_0, y_0) the magnetic field makes a relatively small angle with the normal of the loop: $|\cos(\theta)| = \left|\mathbf{B} \cdot \hat{\boldsymbol{l}}\right| / |\mathbf{B}||\hat{\boldsymbol{l}}| \leq \sqrt{2}/2$. Our study shows that for most of the "loops" the local minima lie within this range of $|\cos(\theta)|$. *(right)* – The parameter space of the Green's function for constant α field in half-space. The function being plotted is $|\cos(\theta)| = \left| G_y(\mathbf{r} - \mathbf{r}_0, \alpha) / \sqrt{G_x^2(\mathbf{r} - \mathbf{r}_0, \alpha) + G_y^2(\mathbf{r} - \mathbf{r}_0, \alpha)} \right|$, where $\mathbf{r}_0 = (0, 0, 0)$ and $\mathbf{r}_1 = (10\cos(320°), 10\sin(320°), h)$. The red contours are $|\cos(\theta)| = \sqrt{2}/2$, the blue dashes contours are $h = n\pi/\alpha$, $n = 0, \pm 1, \pm 2, ...$

3.5. Shape of $d(\alpha, h)$ in the Parameter Space

Figure 30 shows the function $d(\alpha, h)$ for one of the loops from the experiment described above. This function has valleys (dark) in the shapes of hyperbolae, located at or between the hyperbolae $h = n\pi/\alpha$, $n = \pm 1, \pm 2, ...$ After examining parameter spaces of many field lines we have concluded that there is one and only one "branch" of local minima in each $n\pi/\alpha \leq h \leq (n+1)\pi/\alpha$, except for $n = \pm 1$; there are usually two or more "branches" in $-\pi/\alpha \leq h \leq \pi/\alpha$.

The foregoing behavior can be explained by the Green's function in the far field. Far from the photospheric flux concentration at $\mathbf{r}_0$ the field is dominated by the monopole moment, $\mathbf{B}(\mathbf{r}) \propto \mathbf{G}(\mathbf{r} - \mathbf{r_0})$. For a field restricted to half space, Green's function $\mathbf{G}$ is given in [Chiu & Hilton, 1977] and later in [Lothian & Browning, 1995]. It depends on $\sin(\omega h + \phi_0)$ and $\cos(\omega h + \phi_0)$, where $\omega \propto \alpha$ and $\phi_0 \propto \alpha\sqrt{(x - x_0)^2 + (y - y_0)^2}$. If one changes both α and h in such a manner that $\alpha h = const$, that is, remaining on the same hyperbola in (α, h) parameter space, the $\sin(\omega h + \phi_0)$ and $\cos(\omega h + \phi_0)$ terms remain constant.

This observation about the parameter space suggests a useful heuristic restriction to the search. Tracing field lines from (x_0, y_0, h) for increasing values of h (provided $\alpha \neq 0$) causes the angle between the field line and $\mathbf{L}$ at (x_0, y_0, h) to increase or decrease monotonically. The cosine of this angle,

$$\cos(\theta) = \frac{\mathbf{B}(x_0, y_0, h, \alpha) \cdot \mathbf{L}(x_0, y_0)}{|\mathbf{B}||\mathbf{L}|}$$

will be a local maximum near the local minima of $d(\alpha, h)$, but not exactly at the same place. Evaluating the magnetic field at one point is, of course, much faster, than tracing a whole field line. We found that without loss of any information about local minima of d, we may restrict the search to only those (α, h), for which $|\cos(\theta)| \leq \sqrt{2}/2$.

It is clear why the local minima of $d(\alpha, h)$ are co-aligned with maxima in $|\cos(\theta)|$. Since $\mathbf{L}$ is a smooth curve, there will be a vicinity of (x_0, y_0), where $\mathbf{L}$ is, to first order, a straight line. The same is true for field lines of a force-free field: the field lines are smooth curves, so the field line traced from (x_0, y_0, h) in a close vicinity of this point is also to the first order a straight line. Suppose $|\cos(\theta)| = 1$, i.e., $\mathbf{B}(x_0, y_0, h)$ is parallel to $\mathbf{L}(x_0, y_0)$. Then in the neighborhood of (x_0, y_0) the two curves would be exactly the same, and d would be close to zero, if averaged only in that vicinity. Farther from (x_0, y_0) the two may differ significantly resulting in non-zero d over the whole length of the loop.

If the line-of-sight angle is such that the loop's projection is nearly a straight line, then there will be *many* field lines, with different α, that are high enough and long enough to appear nearly straight along all the length of the projection. In this case the fit may give poor results. The upshot is that even though one does not need the whole loop to perform the α-h fit, the projection of the visible portion should not be "too straight". We develop a more quantitative measure for this criterion below.

3.6. α-h fit: Applied to Low & Lou Field

We next test the α-h fit on a set of non-linear force-free fields from [Low & Lou, 1990]. Each of these can be viewed as the field of a singular point source placed below the photosphere and inclined. The field is specified by parameters a (related to characteristic range of field's α), l (depth of the source under the photosphere, we used $l = 0.3$

for all fields), Φ (orientation of the source, we used $\Phi = \pi/2$ for all fields) and n (for explicit derivation and definitions, see the Appendix A).

The experiments were conducted as follows. We generated several Low & Lou fields with different parameters. For each field, we traced a few hundred field lines, projected them on the x–y plane and used them as synthetic loops. Then for each such loop we conducted an α-h fit (by gridded search), with values of α being within the range of Low & Lou's field photospheric α.

We found that for a "dipolar" field (in the sense of it having two distinct polarities, see Figure 31) with $n = 1$, $a = 0.02$, the values resulting from constant α fits do indeed correlate with the real values of the field lines, as shown in Figure 32 (left plot).

For this dipolar field the $d(\alpha, h)$ plots for most loops had one distinct valley of local minima (horizontal or nearly horizontal), and hints of other valleys at larger α or h. Another notable feature of the low valley is that it tends to cross the $\alpha = 0$ line rather than approach it asymptotically. The parameter space for one of these loops is shown in Figure 33 (left plot). Notable in that plot is *the global minimum was always in the lowest nearly-horizontal valley.* The "true location" (from the original Low & Lou field line) was also within that valley; however, it is sometimes offset with respect to the global minimum. In general, *α of the global minima are correlated with α of the original Low & Lou field lines*, as shown in Figure 32 (left plot). Finally, Figure 33 (right plot) shows that the constant α field line of the global minimum seems to approximate the original Low & Lou field line quite well, although a tendency to under-estimate α is evident, and still clearer in the histogram of Figure 32 (right plot).

For notational convenience, we hereafter refer to lines of Low & Lou fields as *real field lines* and to their best-fits of constant α field as *found field lines.* We will also use $(\alpha_{real}, h_{real})$ to denote the parameters of the real field line (recall: h is a height in the midpoint of the line's projection into the photosphere). Similarly, we will use $(\alpha_{found}, h_{found})$ notation to refer to the parameters of the found field line.

Best-fits are potentially useful in reconstructing *the photospheric distribution of* α. We constructed a photospheric map of α by assigning the coronal value to the footpoints of the reconstructed field lines. A full map requires a smoothing, averaging or interpolation, to assign α to photopsheric points around the footpoints of observed loops. To illustrate this possibility we did a robust reconstruction with bicubic spline interpolation (see, for example, [Press et al., 1986]), shown in Figure 34. The fit that we did is simple and robust, nevertheless it is able to reconstruct the general shape of the actual distribution of α in the Low and Lou field.

Another measure of the quality of the fit is its reconstruction of magnetic field $\mathbf{B}$, for example, at $z = 0$. We utilize the form $\mathbf{B}_{ff} = \mathbf{B}_{pot} + \mathbf{B}_{np}$, where $\mathbf{B}_{ff}$ is the full force-free field, $\mathbf{B}_{pot}$ is the potential field with the same normal component at the boundary, and $\mathbf{B}_{np}$ is a "current contribution" — a non-potential (and not in general a force-free) field with $\mathbf{B}_{np} \cdot \hat{\mathbf{n}}|_{\partial\mathcal{V}} = 0$. Note that $\mathbf{B}_{pot}$ is the same for $\mathbf{B}_{L\&L}$ and $\mathbf{B}_{recon}$ (reconstructed), since it is uniquely defined by the volume and by the

Dirichlet boundary conditions. For “weakly non-potential” field $|\mathbf{B}_{pot}| \gg |\mathbf{B}_{np}|$; this is true of some of our cases. Rather than comparing $\mathbf{B}_{L\&L}$ to $\mathbf{B}_{recon}$, we compare their “current contribution” terms, normalized by the potential field: $|\mathbf{B}_{L\&L} - \mathbf{B}_{pot}|/|\mathbf{B}_{pot}|$ to $|\mathbf{B}_{recon} - \mathbf{B}_{pot}|/|\mathbf{B}_{pot}|$. The histogram for $z \in [0, 2]$ pix is shown in Figure 35 (left). To make it, we evaluated $\mathbf{B}_{L\&L}$, $\mathbf{B}_{recon}$ and $\mathbf{B}_{pot}$ *along the found field lines.* It seems that for most of points the two fields were nearly identical, suggesting the accuracy of the reconstruction.

From both Figure 32 and Figure 35 it seems that the reconstruction does a better job for smaller α and for weaker $\mathbf{B}_{np}$, than for larger α and for stronger $\mathbf{B}_{np}$. This and the reasoning from the previous section suggest that *α-h fit might not work for strongly twisted, or maybe strongly non-linear, fields.* We tried to determine the range of α for which the fit would yield reliable results. For that, we generated several more Low & Lou fields, this time quadrupolar (in the sense of it having three polarities, like the field of a point quadrupole): we kept $n = 2$ and gradually increased a over the following values: $a \in [0.05, 0.1885, 0.3, 0.6, 1.0, 1.5, 2.0]$; in addition we computed a field for $n = 3$, $a = 0.4$. We generated both signed and unsigned Low & Lou fields; both have identical photospheric B_z, but the first one has $\alpha > 0$ and $\alpha < 0$, while the second one has only $\alpha > 0$ (see Appendix A). This was done in order to relate the errors of the fit with the “non-linearity”, that is, with how much α changes over a fixed length.

Typical parameter spaces for those fields are shown in Figure 36 and Figure 37. We found that for weakly twisted fields (that is, $a = 0.05$, $a = 0.1885$ and marginally $a = 0.3$, for which $|\mathbf{B}_{recon} - \mathbf{B}_{pot}|/|\mathbf{B}_{pot}|$ is at most 0.15, 0.3 and 0.4 respectively within the computational box close to the photosphere) a typical $d(\alpha, h)$ parameter space has one valley of local minima, with the same characteristics as the parameter space for $n = 1.0$, described earlier. It does not seem to approach $\alpha = 0$ or $h = 0$ asymptotically like a hyperbola would, but rather it crosses $\alpha = 0$ axis. The global minimum always lies on this valley. The point $(\alpha_{real}, h_{real})$ also lies on this valley. It seems that the more horizontal this valley is, the more offset could be the "real" and "found" points along the valley, so the more different could be α_{real} and α_{found}; h_{real} and h_{found} always appear to be very close.

For more strongly twisted fields ($a > 0.3$) the parameter space within the range of α and h of the real field reveals more valleys, although the larger-scale behavior seems to follow the analytic Green's function behavior shown in Figure 30. That is, $d(\alpha, h)$ seems to have valleys of local minima that look like hyperbolae and are located at or in between the hyperbolae $\alpha h = \pm\pi, \pm 2\pi, ...$ Except for $|\alpha h| < \pi$, there is one and only one valley in between every two hyperbolae $n\pi < \alpha h < (n + 1)\pi$, $n = \pm 1, \pm 2, ...$ Within $|\alpha h| < \pi$ there are usually two or more valleys, and one of them is usually "non-hyperbolic" in the sense described above. In these more strongly twisted cases we observed that the global minimum could be in one of the "higher" valleys. It seems that the field line corresponding to (α, h) of the global minimum is much longer than the “loop” (line of Low & Lou field) and morphologically is quite different. Its smaller d results from a small portion of the long line coinciding with the “loop”. This happens especially often for loops that are “too straight” in some sense. This is qualitatively described in Section 3.5 and quantitatively described further in the text.

After inspecting a great number of these parameter space plots we have noticed that $(\alpha_{real}, h_{real})$ still tends to correlate with the location of the “non-hyperbolic” valley. To prove this point, we conducted the following experiment. First we excluded loops that were “too straight”. Second, we chose as the best fit for each of the loops a local minimum on the non-hyperbolic valley, rather than the global miminum. The results of this two-step procedure are shown in Figure 39. The explicit description of the procedure is below.

As a definition of “too straight” we adopted the ratio of sides of a box circumscribing the loop. The box is aligned with the least-square line fit to the loop, its length being the length of the loop along this line and its width being twice the maximal deviation. Based on visual examination we chose the minimum width-to-length ratio to be 0.05 for the “loop” to be eligible for the analysis.

As for selection of the “non-hyperbolic” valley, we developed and followed an algorithm based on the shape of the parameter space. We have found that for Low & Lou fields this algorithm yields good results. First of all, for a given parameter space plot we identified several one-dimensional local minima for each column (α_i, h). Then we manually select some of those local minima that belong to only one of the valleys and find a local minimum of $d(\alpha, h)$ within this valley.

For the selection of the valley, we followed these steps:

0. Consider only the valleys for which $|\alpha h| < \pi$.

1. Is there one "non-hyperbolic" valley in this region? If yes, select the local minima within it. If definitely no, proceed to the next step. If not sure, discard this loop from consideration. If there are several local minima along this valley, select the one that has the lowest h. Example in Figure 38, top left.

1a. If the "non-hyperbolic valley" merges with a "hyperbolic-like" loop, select the local minima in the "non-hyperbolic" part. If unclear, discard this loop from the consideration. Example in Figure 38, top right.

2. Does this "non-hyperbolic" valley seem to change directions, possibly crossing $\alpha = 0$ more than once? If yes, select local minima on *the lowest (smallest h) section of it.* If definitely no, proceed to the next step. If not sure, discard this loop from consideration. Example in Figure 38, middle left.

3. Are there two "non-hyperbolic" valleys on either side of $\alpha = 0$, and neither of them crosses $\alpha = 0$ line? If yes, select local minima on the one that extends to a bigger range of h. If definitely no, proceed to the next step. If not sure, discard this loop from consideration. (We found that such parameter space plots often happens for a "too straight" loop, and threshold of $2\sigma/L = 0.05$

seems to eliminate the majority of them. For the latter ones, α_{real} seems to be on the higher-extending valley.) Example in Figure 38, middle right.

4. If there is no such special valley, among the "hyperbolic" valleys in $|\alpha h| < \pi$ there is a "lowest-order" one, that is, the one that has smallest $|\alpha|$ for $h \to \infty$. Is there enough of this loop presented? (I.e., that did not fall below the threshold on $|cos\theta| \leq \pi/2$, as described in Section 3.5, or that did not fall below any other threshold that was used, such as difference in length being too big, or the length of the field line being significantly smaller than the length of the loop, or the amount of self-crossovers of a field line being two large – we use the second and third thresholds, but not the first one.) If yes, select the *lowest in* h local minima on this valley. If definitely no or not sure, discard this loop from consideration. Example in Figure 38, bottom left.

5. Hard to classify cases: discard from consideration. Example in Figure 38, bottom right.

As shown in Figure 39, for signed field with $a = 1.5$, the global minima selection does not work very well. The above-mentioned algorithm of selection of only "non-hyperbolic" minima works much better; it significantly improves the correlation of α_{real} and α_{found} for large a (and big ranges of α). We also tested this algorithm for when the loops belong to linear force-free fields and verified that it yields the correct results at least within the range $|\alpha|L \leq 5$, which is far beyond the range of all Low & Lou fields studied in this work.

The results for all Low & Lou fields are summarized in Table 1. The individual results are shown in Figs. 40 - 43. This includes scatter plots of α_{real} versus α_{found}, h_{real} versus h_{found}, the comparison of $\mathbf{B}_{ff}$ and $\mathbf{B}_{recon}$ and photospheric distributions of α_{real} and α_{found}. The magnetic fields are compared in the same manner as described in Figure 35: $\mathbf{B}_{ff}$ and $\mathbf{B}_{recon}$ are evaluated at the photospheric level for each of the reconstructed field lines, and a two-dimensional histogram is computed. The photospheric distributions of α_{found} are plotted in the same color table and with the same contours as α_{real} and are obtained in the same manner as described in Figure 34: $\alpha_{found}(x, y, z = 0)$ is collected from all reconstructed field lines; the resulting set of points is used for two-dimensional spline interpolation.

We draw several conclusions based on the results of this analysis, First, at least for some range of α, field lines of Low & Lou fields could indeed be approximated with the field lines of constant α fields of similar α and h. The reconstructed photospheric distribution of α seems to recover the general shape of the original field. Amazingly, it is also able to recover the area of the strongest gradients of α. Second, the height of the loops is reconstructed very well for the fields with a small range of α and less well for the fields with a greater range of α (see correlation coefficients and errors in Table 1; note that for unsigned fields the range of α is about half the range in signed fields). Third, this method is also capable of reconstructing the magnetic field, at least near the photosphere.

We summarize all the results on two plots in Figure 44. For each Low & Lou field, we looped through α_{found} and measured the mean and standard deviation of α_{real}, and plotted $\langle\alpha_{real}\rangle \pm \sigma$ versus α_{found}. We did the same for h. It seems that the method systematically underestimates α by a small amount and it sometimes overestimates h by a small amount. The least-squares line fit of the mean values, including standard deviation, gives an estimate $\langle\alpha_{real}\rangle \propto 1.23\alpha_{found}$ and $\langle h_{real}\rangle \propto 0.79h_{found}$.

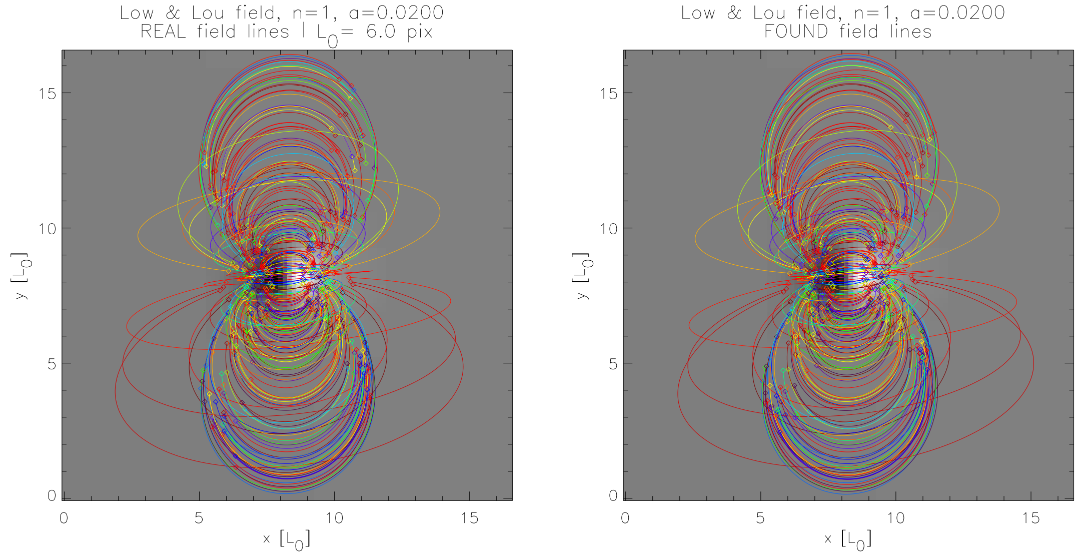

Figure 31. *(left)* – A synthetic magnetogram of a non-linear nearly-dipolar field at the photosphere, with synthetic "loops" – field lines – projected onto x–y plane. For each of those lines we tried to approximate it with a line of a constant α field, recording α_{found} and comparing it with the real α of the original field line. *(right)* – Best-fit field lines of constant α fields, each line belonging to a different constant α field. Hereafter all lengths are given in the units of L_0 – a characteristic separation distance between two polarities, we calculated it as the distance between the pixels with maximal and minimal magnetic fields. In this case, $L_0 = 6$ pix.

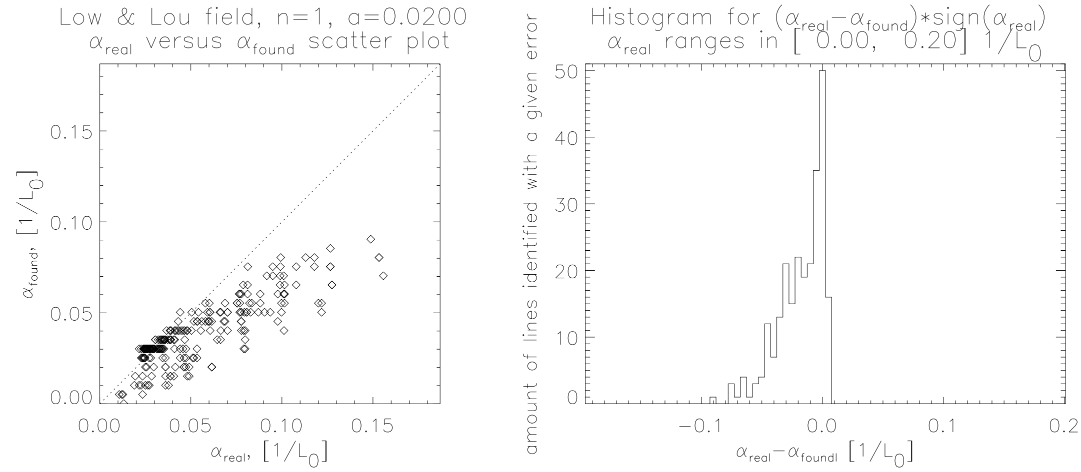

Figure 32. Results for the data, shown in Figure 31. On the left is a scatter plot of α_{real} vs. α_{found}. The correlation is evident. On the right is the histogram of the error $\alpha_{real} - \alpha_{found}$.

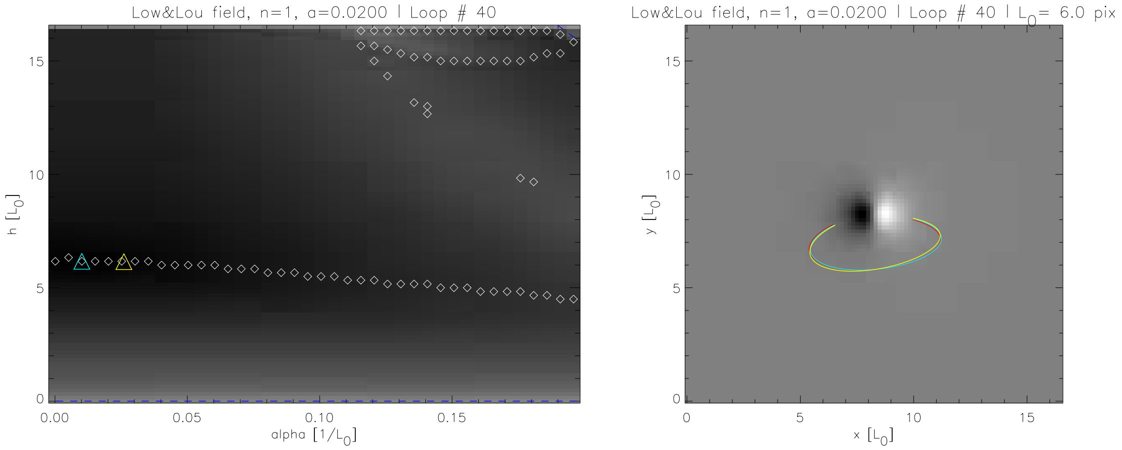

Figure 33. *(left)* – A typical $d(\alpha, h)$ parameter space for one of the field lines shown in Figure 31. There is one nearly horizontal valley of local minima and a clue to other possible valleys for larger (α, h). White diamonds show the local minima in individual columns. Cyan triangle shows the location of the global minimum. A yellow triangle shows "real" (α, h) of the Low & Lou field line. Blue dashed lines (barely visible on this plot, but more evident on the other plots of this kind) are hyperbolae $\alpha h = n\pi$, $n = 0, \pm 1, \pm 2, ...$ *(right)* – Best-fit for the same field line (cyan), field of the constant α field, traced from the "real" values (yellow), and the the Low & Lou field line (red). The difference is barely visible, however, the cyan line seems to match red line better than the yellow line.

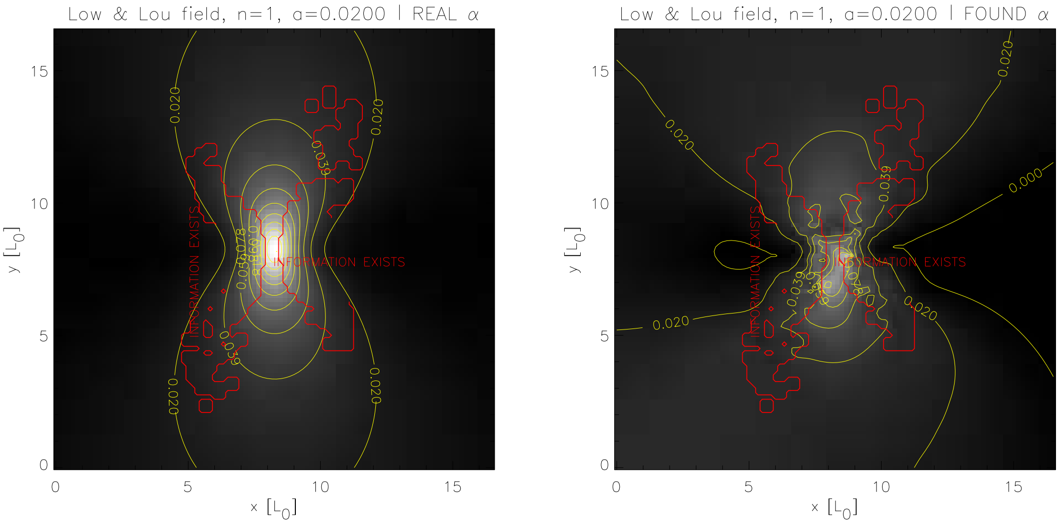

Figure 34. *(left)* – Photospheric distribution of α for the field from Figure 31. The yellow contours are contours of α. *(right)* – the result of the reconstruction using α-h fit. The grayscale and contours on this reconstruction are identical to those on the real distribution. The red contours show the location of the footpoints of the found lines, that is, *there is no information outside of these contours*, and whatever is outside is shown solely for easy viewing. The only meaningful part is inside of the red contours. The result was extrapolated using thin plate splines fit into the set of footpoints with found α. This robust fit is sensitive to individual noisy points, and it is intended only to illustrate of the potential possibility of such reconstruction. Yet, with all these remarks, such robust fit is capable of reconstructing the principal shape of the distribution.

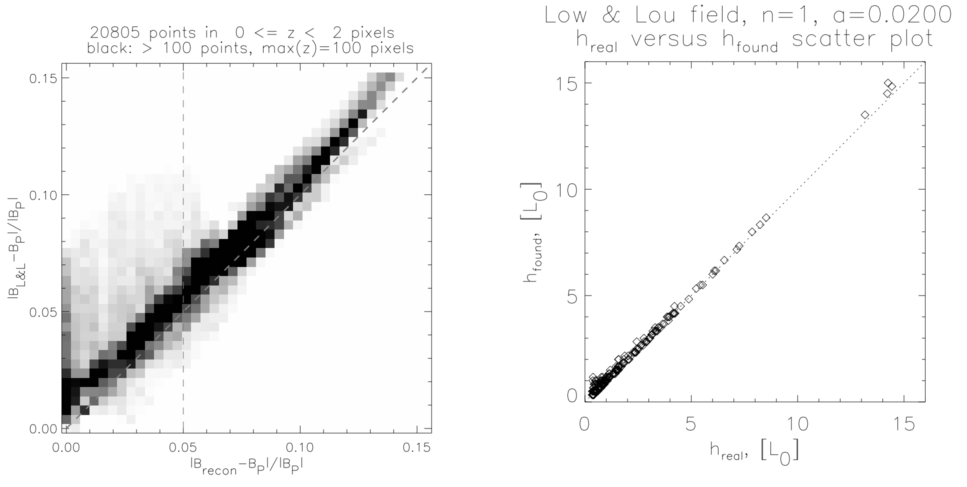

Figure 35. *(left)* – the comparison of reconstructed magnetic field, $\mathbf{B}_{recon}$ to the Low & Lou field, $\mathbf{B}_{L\&L}$, at the photospheric level ($0 < h < 2$ pix). We follow the "found" (best-fit) field lines and evaluate $\mathbf{B}_{lfff}$ (with different α for each field line), $\mathbf{B}_{L\&L}$ and $\mathbf{B}_{pot}$ along them. By $\mathbf{B}_{recon}$ we mean the composition of $\mathbf{B}_{lfff}$'s for all loops (strictly speaking, the way it's constructed makes it in general not force-free and probably not even source-free, so it could hardly be called a magnetic field at all, rather, an approximation of the reconstructed field, evaluated along different field lines). As discussed in the text, most of the field is potential, so we compare the "non-potential" contributions only, normalized by the potential field. Here $\mathbf{B}_{pot}$ is a potential magnetic field, that is restricted to the upper half-space and has the same Dirichlet boundary conditions as $\mathbf{B}_{L\&L}$ and the same as $\mathbf{B}_{recon}$. It seems that the non-potential part of the magnetic field is reconstructed well. *(right)* – scatter plot of h_{real} vs. h_{found}. It seems, that h is found with much better confidence than α.

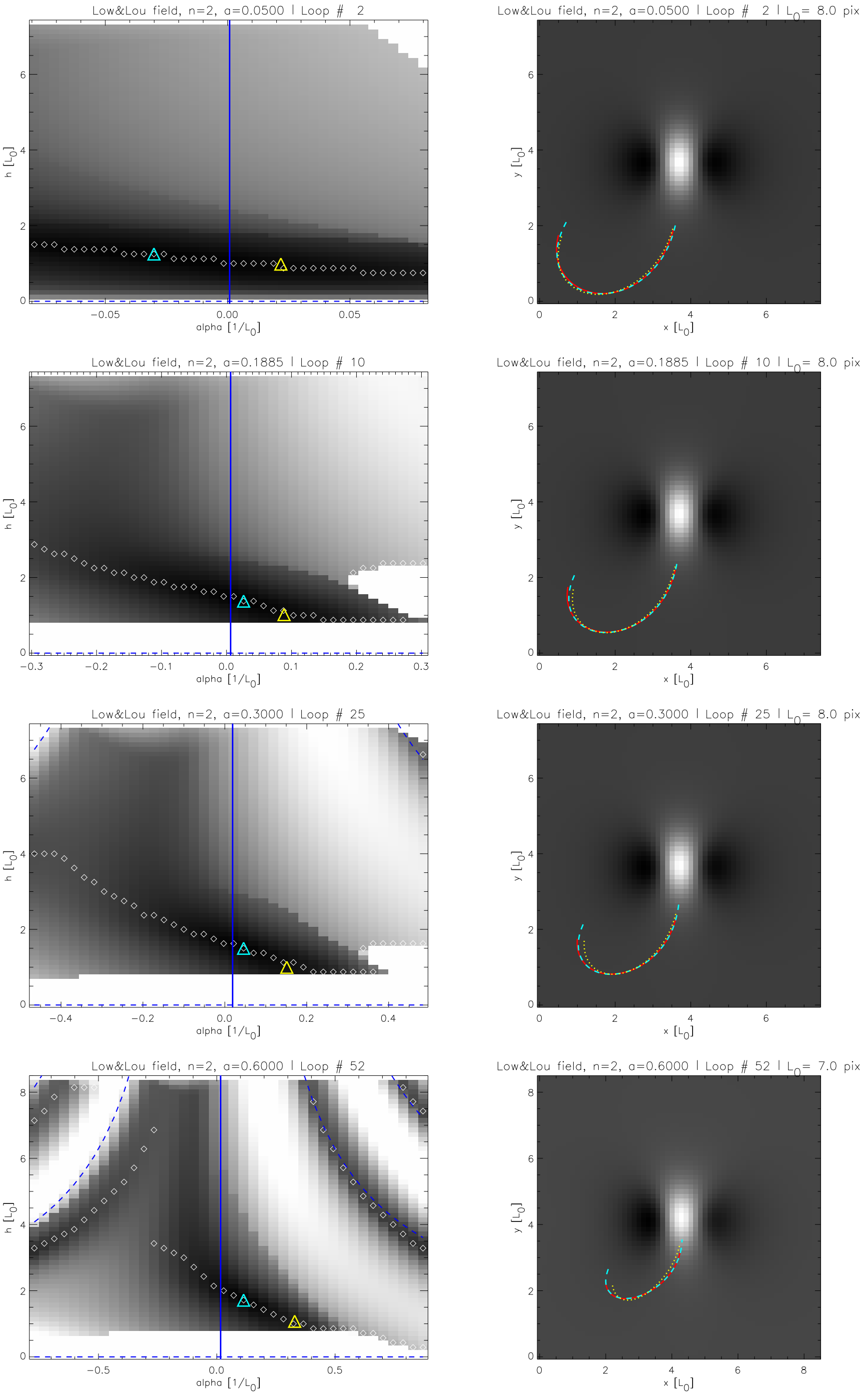

Figure 36. *(left column)* – typical parameter spaces for Low & Lou fields with gradually increasing a. Here dashed blue lines are hyperbolae $\alpha h = 0, \pm\pi, \pm 2\pi, ...$, white diamonds show local minima in each column $\alpha = const$, yellow triangle shows the location of $(\alpha_{real}, h_{real})$ and cyan triangle shows the location of the global minimum, that is, $(\alpha_{found}, h_{found})$. *(right column)* – the original "loop" of each of those parameter spaces (red), the "global minimum" field line (cyan) that has $(\alpha_{found}, h_{found})$ and a constant α field line, that has $(\alpha_{real}, h_{real})$ (yellow).

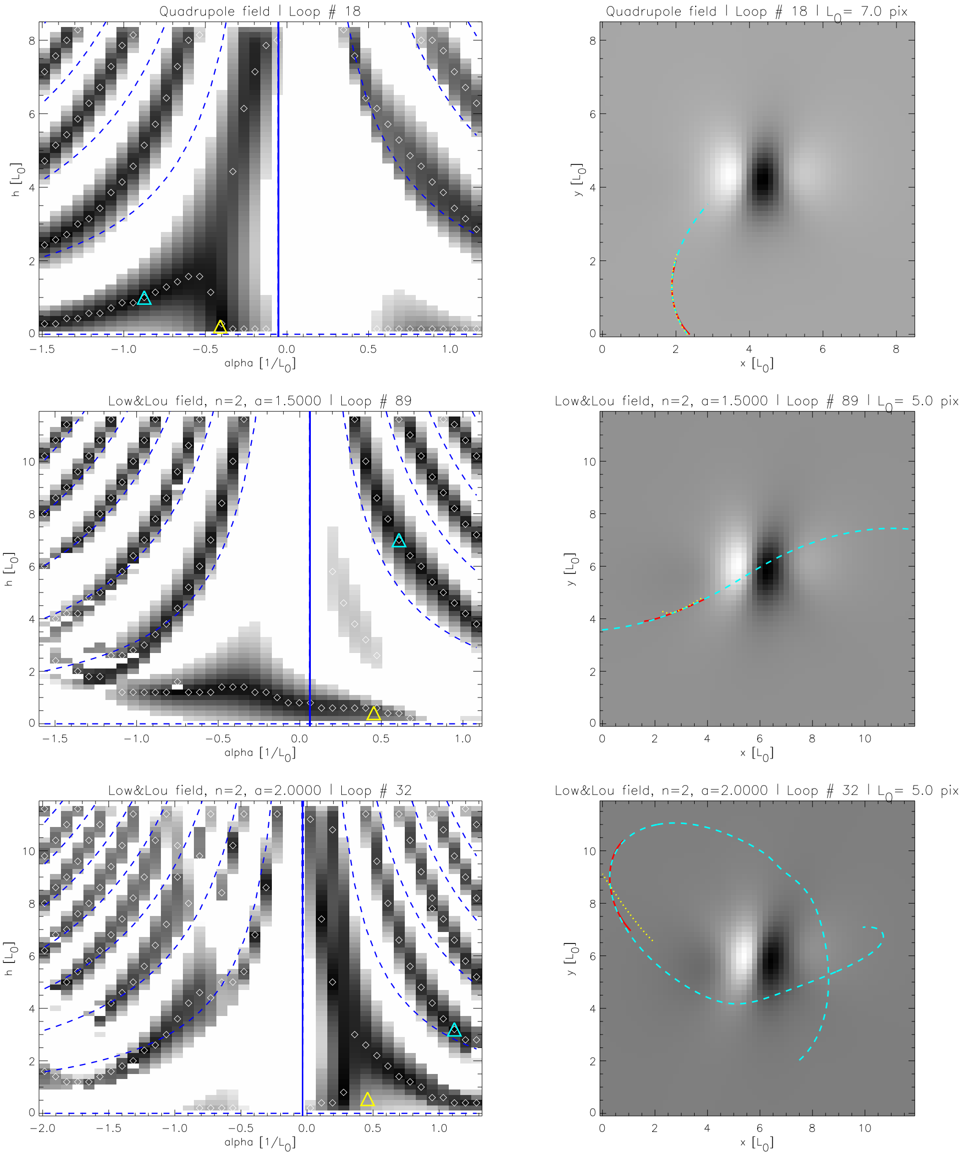

Figure 37. The continuation of Figure 36 for larger a, the notation is the same. Note that $(\alpha_{real}, h_{real})$ is still at or near the "non-hyperbolic" valley, while the global minimum could be at one of the other valleys. The field line, corresponding to the global minimum, is much longer than the loop and part of this field line happened to match the loop.

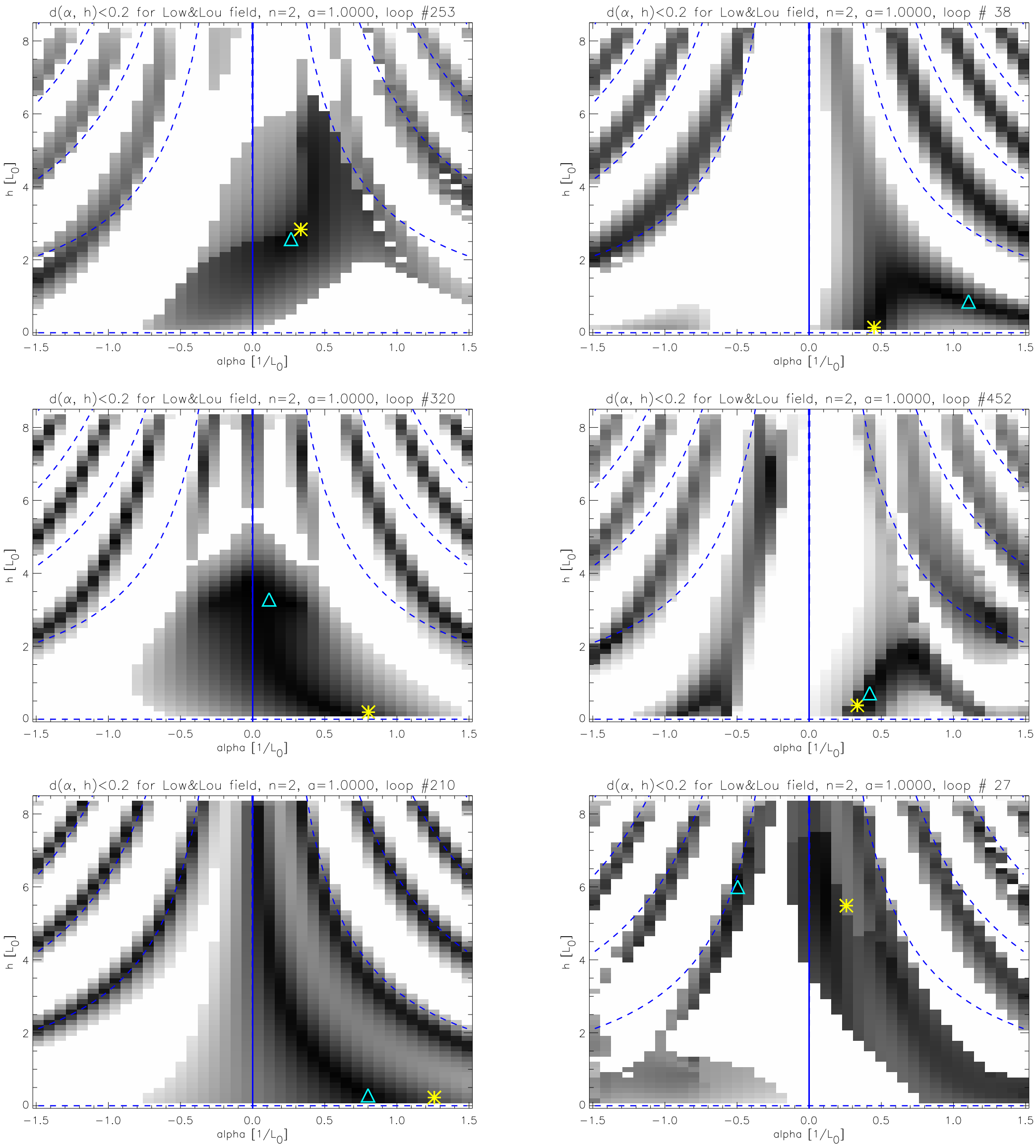

Figure 38. The illustrations of the algorithm that helps to select local minimum on "non-hyperbolic" valley. The notation is the same as in Figure 36. For description, please refer to the different options in the algorithm.

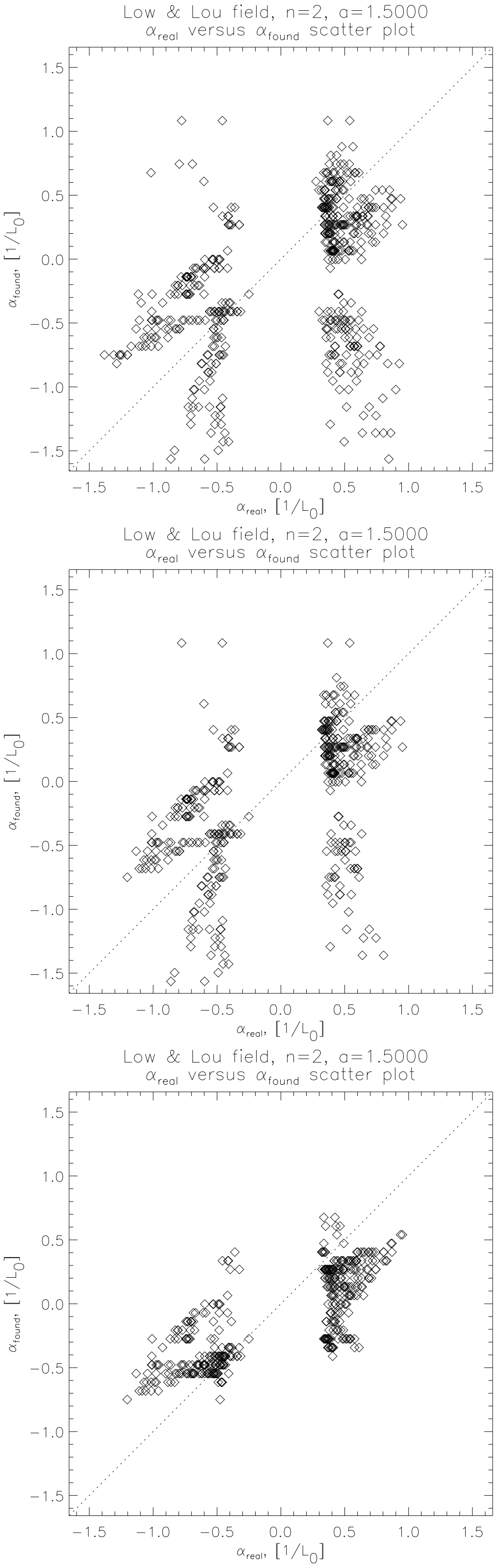

Figure 39. *(top)* – a scatter plot of α_{real} vs. α_{found} for “signed” $a = 1.5$, $n = 2$ Low & Lou field. *(middle)* – same, but with “too straight” loops removed. *(bottom)* – same, but with “too straight” loops removed and with the minima selected only along “non-hyperbolic” valleys rather than the global minimum.

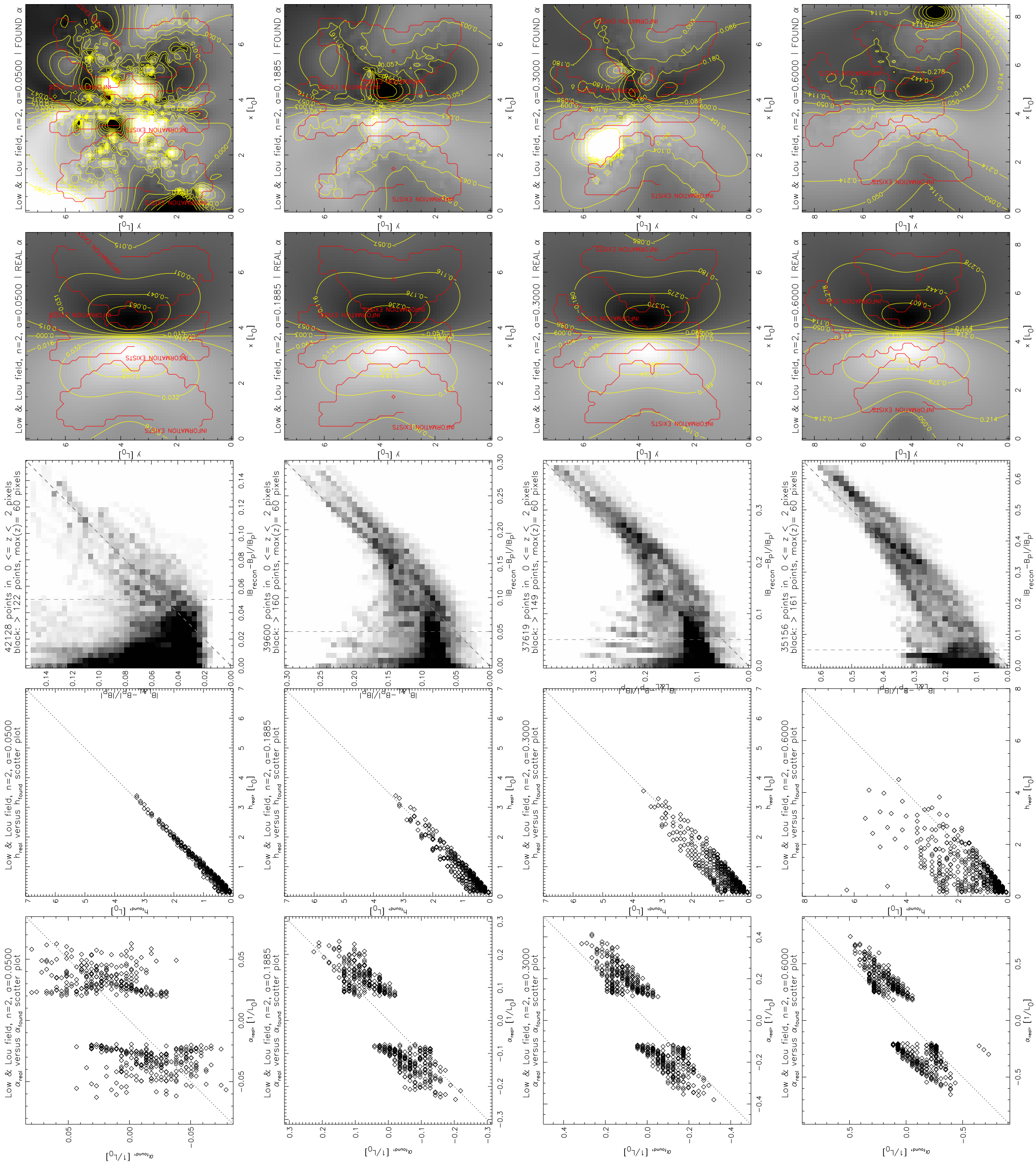

Figure 40. The results of the fit for "signed" Low & Lou fields: scatter plots of α_{real} vs. α_{found} (first column), h_{real} vs. h_{found} (second column), histogram of $|\mathbf{B}_{ff} - \mathbf{B}_{pot}|/|\mathbf{B}_{pot}|$ (third column), real and reconstructed photospheric distributions of α (fourth and fifth columns respectively, the notation is same as in Figure 34). Note that as the range of α increases, the reconstructed photospheric distribution of α gets better, but the correlation of h_{real} and h_{found} gets worse.

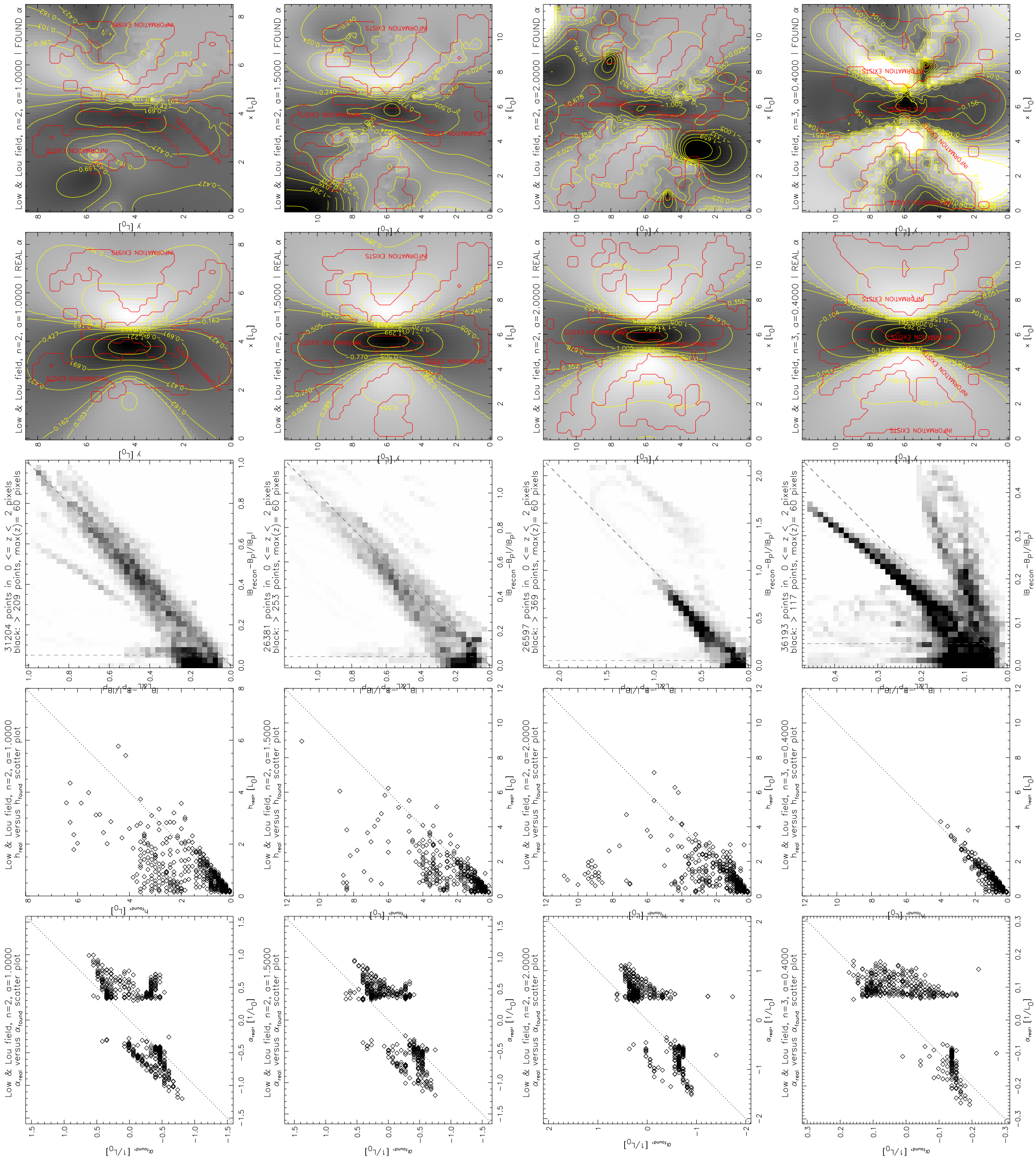

Figure 41. The results of the fit for "signed" Low & Lou fields. The notation is the same as in Figure 40. Note that the last row corresponds to an $n = 3$ field.

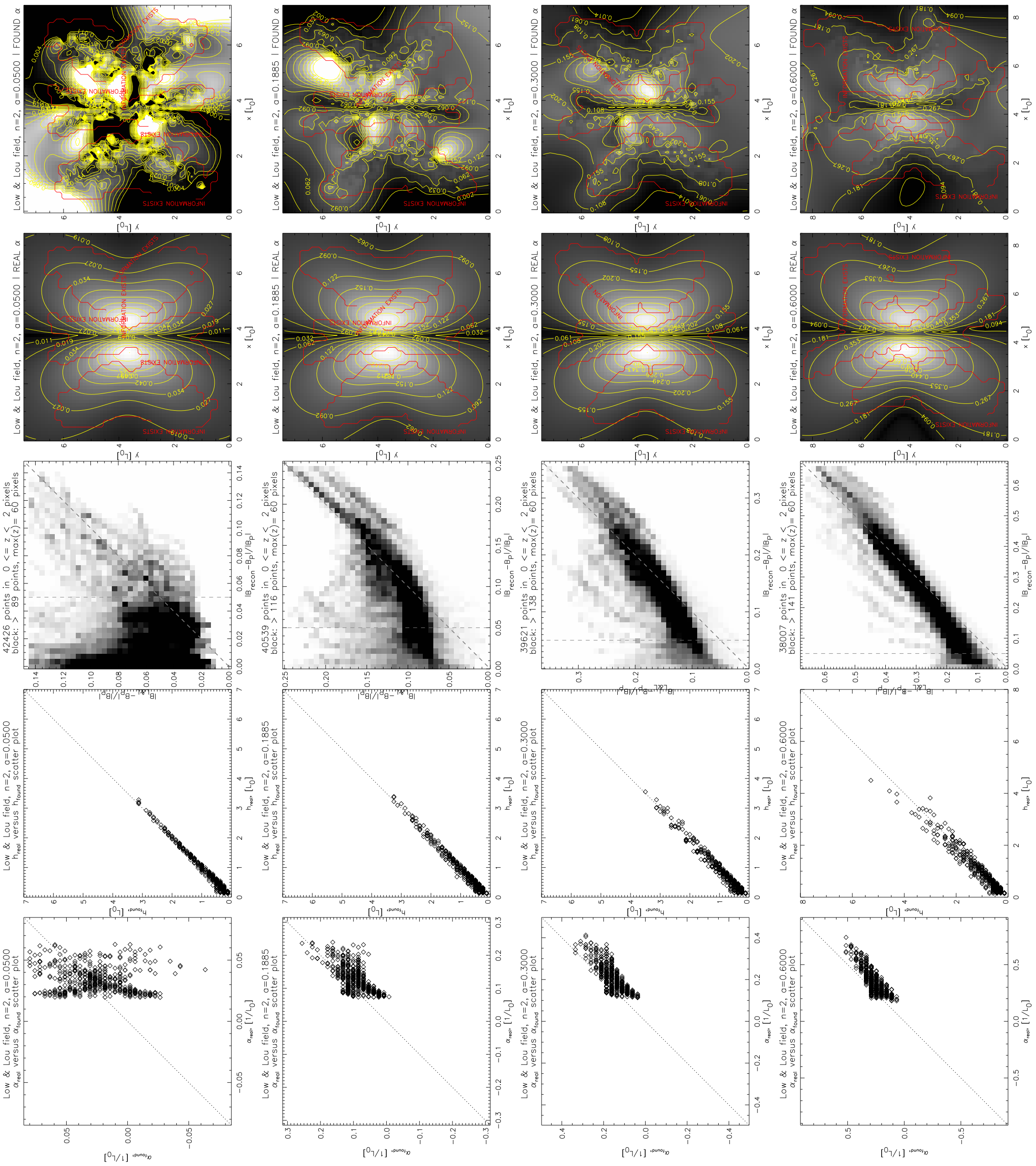

Figure 42. The results of the fit for “unsigned” Low & Lou fields. The notation is the same as in Figure 40.

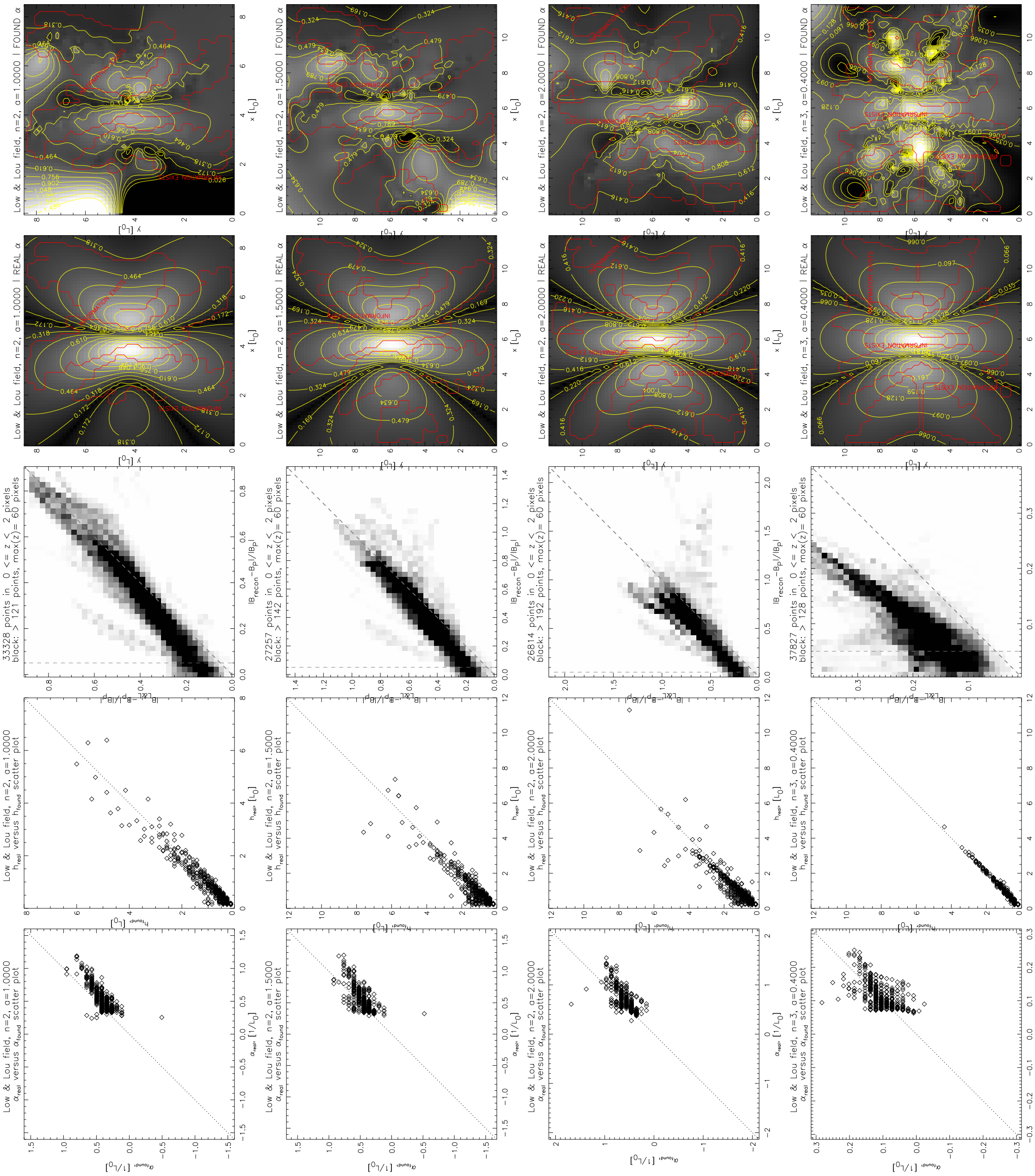

Figure 43. The results of the fit for “unsigned” Low & Lou fields. The notation is the same as in Figure 40. Note that the last row corresponds to an $n = 3$ field.

n	a	sign of α	L_0, pix	α range, $1/L_0$	α fit results			h fit results			$\lvert\mathbf{B}-\mathbf{B}_{pot}\rvert/\lvert\mathbf{B}\rvert$ fit results		
					LAD slope	LAD mean abs. dev.	r_s	LAD slope	LAD mean abs. dev.	r_s	LAD slope	LAD mean abs. dev.	r_s
1	0.02	+	6.0	0.196	1.63	6.65	0.805	0.99	0.55	0.967	1.03	3.21	0.934
2	0.05	+	8.0	0.080	0.17	10.15	0.160	1.01	0.73	0.968	1.06	7.29	0.563
2	0.1885	+	8.0	0.302	0.60	7.55	0.585	1.01	0.92	0.966	0.59	6.99	0.647
2	0.3	+	8.0	0.484	0.86	6.49	0.743	0.99	1.13	0.954	0.64	5.79	0.812
2	0.6	+	7.0	0.871	1.03	5.63	0.805	0.93	1.59	0.944	0.75	4.01	0.937
2	1.0	+	7.0	1.486	1.19	5.22	0.799	0.87	1.86	0.926	0.82	3.21	0.943
2	1.5	+	5.0	1.564	1.09	6.36	0.696	0.90	2.22	0.825	0.78	6.74	0.896
2	2.0	+	5.0	1.985	1.19	5.45	0.789	0.87	2.11	0.870	0.79	9.02	0.809
3	0.4	+	5.0	0.315	0.45	7.50	0.567	1.06	0.60	0.965	1.32	3.37	0.775
2	0.05	±	8.0	0.159	0.72	15.00	0.601	1.00	0.85	0.964	0.94	6.60	0.593
2	0.1885	±	8.0	0.598	1.36	9.14	0.879	0.96	1.80	0.921	0.67	6.84	0.708
2	0.3	±	8.0	0.949	1.41	8.78	0.889	0.89	2.70	0.855	0.68	7.38	0.749
2	0.6	±	7.0	1.642	1.40	10.02	0.875	0.53	4.83	0.715	0.73	6.58	0.885
2	1.0	±	7.0	2.647	1.30	12.14	0.660	0.35	5.41	0.621	0.81	5.56	0.895
2	1.5	±	5.0	2.647	1.42	10.16	0.770	0.47	3.48	0.756	0.88	6.49	0.818
2	2.0	±	5.0	3.268	1.49	8.36	0.795	0.56	3.89	0.689	0.64	3.50	0.821
3	0.4	±	5.0	0.529	0.95	11.38	0.704	0.98	1.25	0.889	0.22	6.23	0.386

Table 1. A brief summary of the results, shown in Figs. 40-43. LAD fit and Spearman's rank order correlation r_s were computed for $\alpha_{real}(\alpha_{found})$. LAD mean absolute deviation for α is given in percent of the range of α along the photosphere, for h in percent of the maximal height, and for $|\mathbf{B}-\mathbf{B}_{pot}|/|\mathbf{B}_{pot}|$ in percent of the maximal value along all measured field lines in the same height range that is used for the histograms. All statistics for the latter one is measured for $|\mathbf{B}-\mathbf{B}_{pot}|/|\mathbf{B}_{pot}| > 0.05$. The confidence of Spearman's rank-order correlation is bigger than 99.95% of α for signed $n = 2$, $a = 0.05$ and bigger than 99.999% for all other entries..

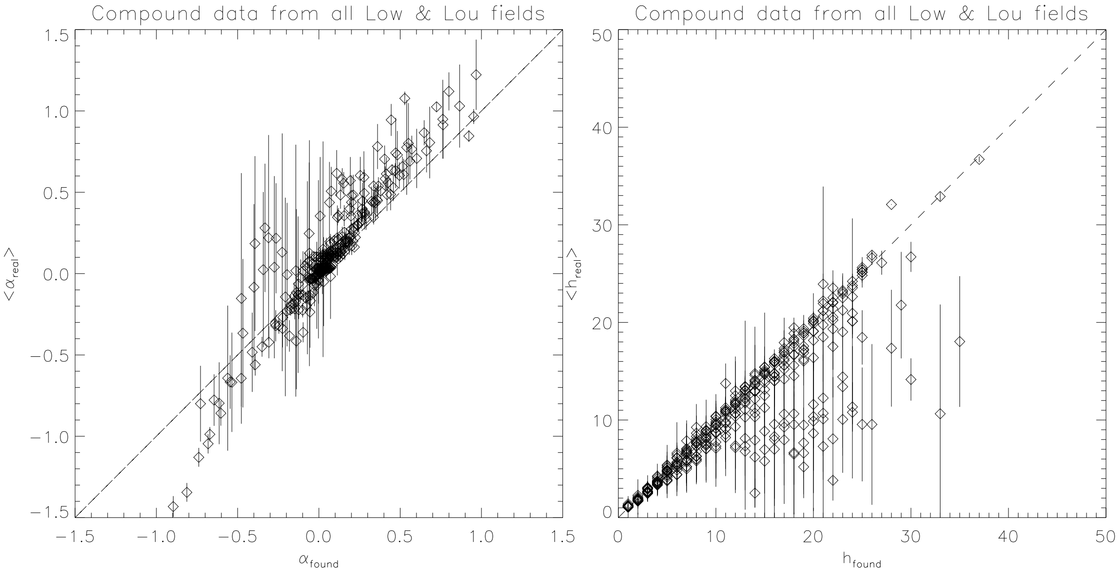

Figure 44. *(left)* – Compound plot based on all Low & Lou fields measurements. For each field we went through all α_{found} and measured mean and standard deviation of α_{real}. Each such measurement corresponds to a point and error bar on this plot. *(right)* – same for h. The units for α are $1/L_0$ and for h are L_0, where L_0 is a separation distance between two polarities.

3.7. α-h-Fit Applied To Solar Data

As a further test of the applicability of the method, we applied the algorithm described above to real solar data. We chose the unnumbered active region close to disk center on 2007 February 10. This region, denoted SOL2007-02-10T11:22:L290C101 according to the Solar Object Locator[2], was observed by the instruments on Hinode [Kosugi et al., 2007], particularly the X-Ray Telescope (XRT, [Golub et al., 2007, Kano et al., 2008]). As reported by [McKenzie & Canfield, 2008], the region had a sigmoidal shape indicative of highly sheared coronal loops. Such regions are believed

---

[2] http://www.iac.es/proyecto/iau_divii/IAU-DivII/documents/target_naming_convention.html

to comprise strongly twisted non-potential magnetic fields, and thus store significant amounts of energy, and commonly erupt in flares and/or coronal mass ejections. For this reason, coronal sigmoids present a very reasonable target structure for application of the proposed method of magnetic field modeling. The 2007 February sigmoid is particularly useful because the high-resolution observations of Hinode/XRT (1 arcsecond per pixel) and the sigmoid's location near disk center facilitate tracing of the individual loops forming the sigmoid. We utilized the XRT image from 2007 February 10, 11:22:06UT, to identify and trace 12 coronal loops. The magnetic models were generated from LOS magnetograms from the MDI instrument on SOHO [Scherrer et al., 1995], and then utilized for fittings to obtain the 3D shape and α of the coronal loops.

To get the two-dimensional shape from XRT image we manually drew smooth curves (3-point cubic spline) over each of the loops. We then visually co-aligned XRT and MDI images and obtained (x, y) of the loops in MDI coordinates. No de-rotation was needed since MDI and XRT data were within one minute of each other. Since the region of interest was small enough, and close to disk center, we worked in a tangent plane approximation where the photospheric plane, $z = 0$, was taken to be the plane of the sky.

To perform the fitting we extracted a region measuring $506'' \times 506''$ from the full-disk MDI magnetogram (257×257 pixels). In order to save computation time, we downsized the magnetogram by a factor of two in each dimension. Then we generated constant α fields confined to half space (using Green's function from [Chiu & Hilton, 1977]) in a $506'' \times 506'' \times 200''$ computational box. We generated 41 different fields with $-0.04 \leq \alpha \leq 0.04$ arcsec^{-1}.

The results are summarized in Table 2 and Figure 45. Visually it seems that the fit did a good job for all but three loops. The parameter space plots, such as the one shown in Figure 46, all looked like those for Low & Lou fields. For all of them we applied the proposed algorithm of selecting local minima on "non-hyperbolic" valley.

Disregarding the three "unsuccessful" fits, it seems that α was of the order of $0.010 - 0.015$ arcsec^{-1} in the outer region of the sigmoid, and higher in the middle, exceeding 0.02 arcsec^{-1}. Using the solar radius $983.13''$ and recalling a typical bias of $\alpha_{real} \propto 1.23\alpha_{found}$ (see Figure 44), we estimate α_{real} to be $1.7 - 2.6 \times 10^{-8}\mathrm{m}^{-1}$ in the outer regions and over $3.5 \times 10^{-8}\mathrm{m}^{-1}$ in the core. These values fall in the range typical of active region fields, such as those reported in [Burnette et al., 2004]: $\pm 4 \times 10^{-8}\mathrm{m}^{-1}$. The magnetic field strength along all the non-potential field lines was always within 50% of the strength of the potential field, evaluated along the same path; it was within 25% in at least half the cases.

Assuming a typical separation distance $L \approx 50''$ (see Figure 45) the values of α_{found} was of the order of $0.5 - 0.75L^{-1}$ outside of the sigmoid and exceeded $1.0L^{-1}$ inside of the sigmoid. This is within the range of reconstructed α in the trial Low & Lou fields (see Figure 44).

Loop #	α, arcsec^{-1}	h_{max}, arcsec
0	0.012	12.9
1	0.016	0.0
2	0.014	23.8
3	0.026	9.5
4	*0.008*	*35.4*
5	*0.024*	*33.9*
6	0.020	14.3
7	0.014	12.7
8	0.010	31.5
9	*0.010*	*24.5*
10	0.012	27.4
11	0.010	3.3

Table 2. The results of the α-h fit to solar data. Here h_{max} is maximal height (not height at mid-point, as before in the text). Loops that don't seem to give a good fit to the data are in italic.

3.8. Discussion

In this work we have proposed a semi-automated method that, from a given two-dimensional EUV or X-Ray image of coronal loops and a line-of-sight magnetogram, reconstructs local twist and a three-dimensional shape of each loop. It tacitly assumes that coronal loops follow magnetic field lines. Our fitting matches the plane of sky projection of each loop to the projection of lines of linear force-free fields, traced from different heights along the line-of-sight and that have different twist in them. The method thus constructs a linear force-free field and one field line in it, that is the best match of an individual loop. The method is similar to the ones proposed by [Green et al., 2002] and [Lim et al., 2007], however, it holds several important advantages. First, it does not require a full length of the loop to be visible for a successful reconstruction. Secondly, it does not require any of the footpoints to be visible. Thirdly, it allows the user to draw a smooth curve (e.g., a Bézier spline) interactively on top of the loop, rather than selecting a few points along the loop, thus maximizing the amount of information taken from the coronal image.

We address the question of validity of such a reconstruction, given the fact that the coronal field is probably non-linear force-free and that the superposition of linear force-free fields obtained for each individual loop would not, in general, be a force-free field. To do so, we perform a series of tests on non-linear analytic force-free fields, described in [Low & Lou, 1990], and as model loops we utilize projections of field lines on the photosphere. We compare several results of the method with the original field: 3D shapes of loops, local twist (coronal α), distribution of twist in the photosphere and the strength of magnetic field.

We also find that the best-fit line may not be a global minimum of $d(\alpha, h)$, but one in a particular part of parameter space. We developed an algorithm that aids in locating the appropriate region of the parameter space. We followed it manually, but it could be automated. The algorithm seems to improve the results on Low & Lou fields, but it probably does not describe every possible feature of the parameter space resulting from every single arbitrary magnetic field. The algorithm could be improved and expanded, based on further research involving other non-linear fields and real solar data.

Based in Table 1 we draw the conclusions (i) that on the trial fields the twist is reconstructed with mean absolute deviation of at most 15% of the range of photospheric twist, (ii) that heights of the loops are reconstructed with mean absolute deviation of at most 5% of the range of trial heights, and (iii) that the magnitude of non-potential contribution to photospheric field is reconstructed with mean absolute deviation of at most 10% of the maximal value.

As shown in Figure 44, there is a typical underestimation of twist when performing this procedure. Based on the experiments with Low & Lou fields we conclude, that typically $\alpha_{real} \approx 1.23\alpha_{found}$.

We also demonstrate how this method can be applied to real solar data, by doing the reconstruction based on the data from SOHO/MDI magnetograms and Hinode/XRT X-Ray images. The resulting field lines visually match the observed loops, have reasonable heights and self-consistent amount of twist of the magnitude that agrees with existing measurements of twist in active regions [Burnette et al., 2004].

This work was supported by NASA grants NNX07AI01G and NNX06AB83G.

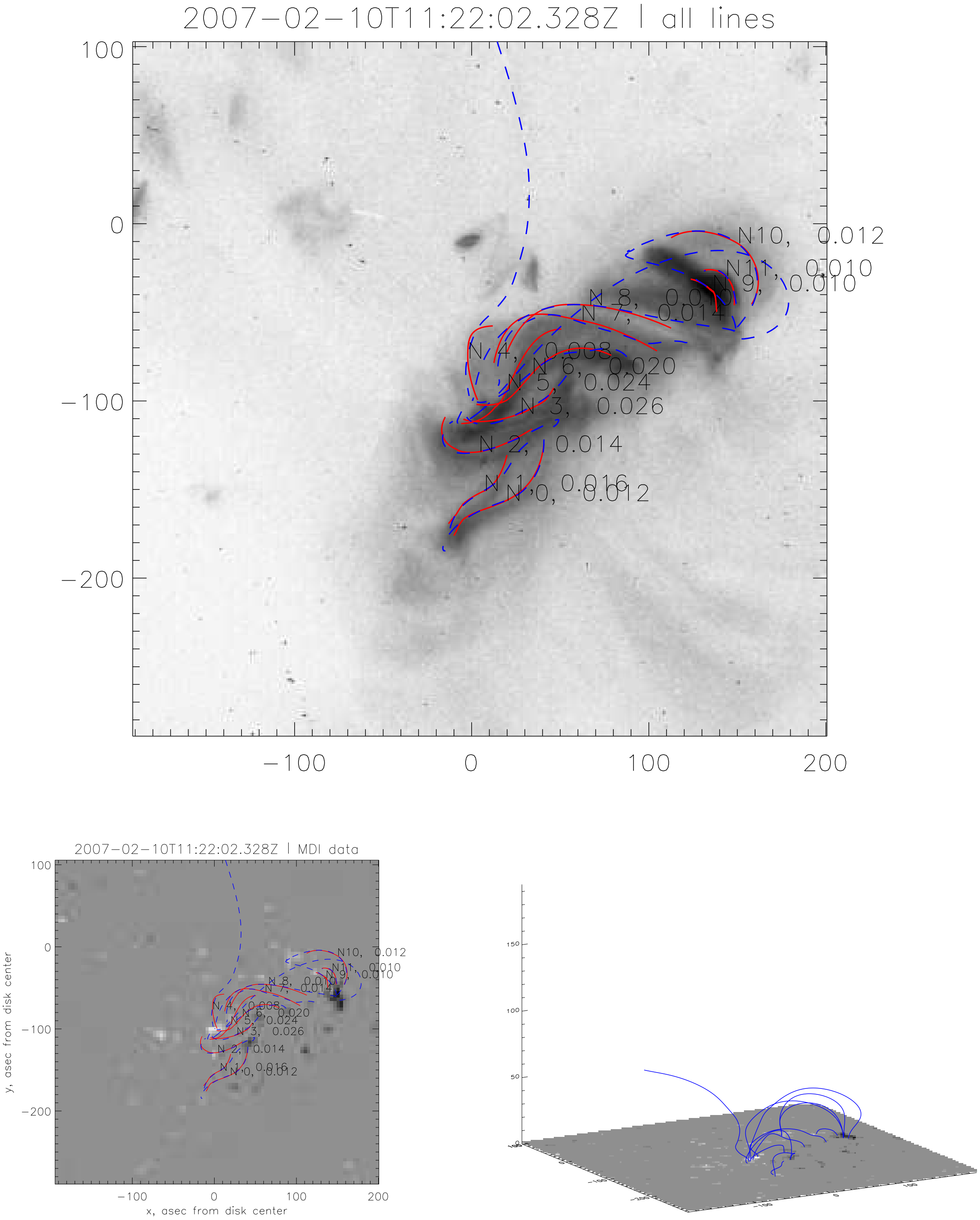

Figure 45. Out of 12 loops that we selected, three, namely, loops 4, 5, 9 don't seem to give a good fit to the data, and the rest seem to give fairly good fit.

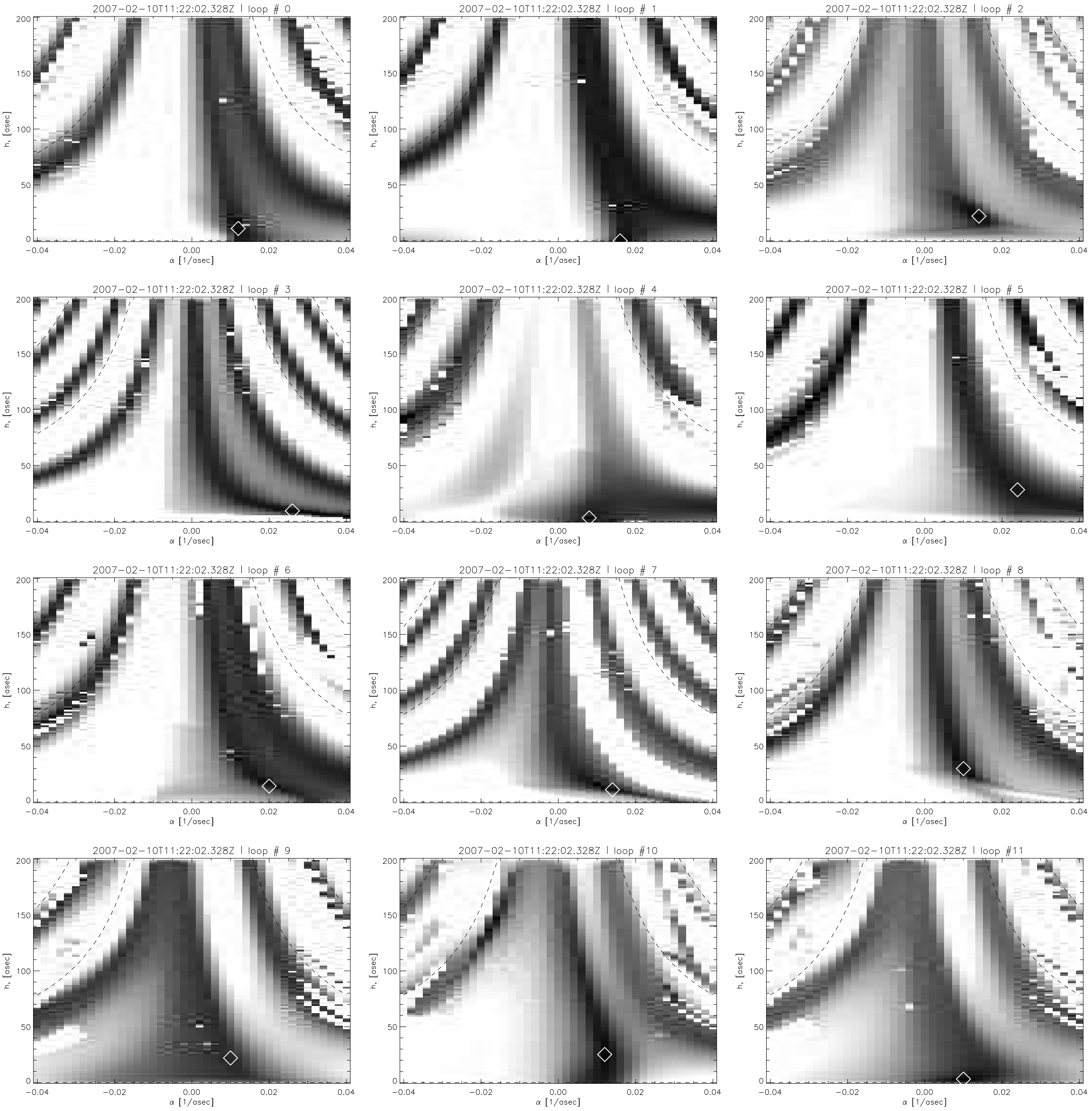

2007−02−10T11:22:02.328Z | loop # 0

2007−02−10T11:22:02.328Z | loop # 1

2007−02−10T11:22:02.328Z | loop # 2

2007−02−10T11:22:02.328Z | loop # 3

2007−02−10T11:22:02.328Z | loop # 4

2007−02−10T11:22:02.328Z | loop # 5

2007−02−10T11:22:02.328Z | loop # 6

2007−02−10T11:22:02.328Z | loop # 7

2007−02−10T11:22:02.328Z | loop # 8

2007−02−10T11:22:02.328Z | loop # 9

2007−02−10T11:22:02.328Z | loop #10

2007−02−10T11:22:02.328Z | loop #11

Figure 46. Parameter spaces for loops shown in Figure 45.

4. DIRECT MEASUREMENTS OF MAGNETIC TWIST IN THE SOLAR CORONA

4.1. Abstract

In the present work we study evolution of magnetic helicity in the solar corona. We compare the rate of change of helicity in the corona to the helicity flux through the photosphere and find that the two rates are similar. This gives an observational evidence that helicity flux across the photosphere is indeed what drives helicity changes in solar corona during emergence.

For the purposes of estimating coronal helicity we neither assume a strictly linear force-free field, nor attempt to construct a non-linear force-free field. For each coronal loop evident in Extreme Ultraviolet (EUV) we find a best-matching line of a constant-α field and allow α to be different for each line. This method was introduced and its applicability was discussed in [Malanushenko et al., 2009b].

The object of the study is emerging and rapidly rotating AR 9004 over the time interval of about 80 hours. As a proxy for coronal helicity we use the quantity $\langle \alpha_i L_i/2 \rangle$ averaged over many reconstructed lines of magnetic field. We argue why it is approximately proportional to "flux-normalized" helicity H/Φ^2, where H is helicity and Φ is total enclosed flux of the active region. The time rate of change of such quantity in the corona is found to be about 0.021 rad/hr (about 1.2 deg/hr, comparable to many such observations).

This result is compared to the helicity flux through the photosphere, using data from [Longcope et al., 2007] for the same AR at the same time, obtained using local correlation tracking method. The flux of normalized helicity is found to be 0.016 rad/hr.

4.2. Introduction

Magnetic helicity is generally accepted to be an important quantity in understanding evolution of coronal magnetic fields and studying solar eruptions. It is approximately conserved when conductivity is high, as it is expected to be in solar corona. This sets up an important constraint on evolution of a magnetic field. It is believed that helicity in excess of a certain threshold could be responsible for triggering magnetohydrodynamics instabilities and thus be responsible for coronal mass ejections (CMEs) (see [Démoulin, 2007] for further discussion).

Helicity is a function of magnetic field $H = H(\mathbf{B})$, defined as a volume integral of $\mathbf{A} \cdot \mathbf{B}$ (where $\mathbf{A}$ is the vector potential and $\mathbf{B}$ is the magnetic field), if no lines of magnetic field leave this volume. For situations, when field lines leave the volume (e.g., $\mathbf{B} \cdot \hat{\mathbf{n}} \neq 0$ on the boundary), such as the solar corona, where there is a nonzero magnetic flux through the photosphere, helicity is defined *relative* to some reference field: $H_{relative} = H(\mathbf{B}, \mathbf{B}_{ref}) = H(\mathbf{B}) - H(\mathbf{B}_{ref})$, that has the same normal component of magnetic field at the boundary of the volume [Berger & Field, 1984, Finn & Antonsen, 1985]. A potential magnetic field

($\nabla \times \mathbf{B}_{ref} = 0$) has the minimum possible energy, so using it as a reference means a non-zero helicity demands some free energy. Relative helicity, defined this way, is approximately conserved under internal (to the volume of integration) motions of the plasma.

Direct measurements of helicity in the corona remain an extremely challenging problem. They are usually performed by extrapolating magnetic field into corona using photospheric magnetic field as a boundary condition and then estimating the helicity of this field. The extrapolations are often performed in such a way that lines of resulting magnetic field resemble observed coronal loops evident in extreme ultraviolet (EUV) or soft X-Rays (SXR). The popular choices of magnetic fields are constant-α field[1] confined to a box, e.g., [Green et al., 2002, Lim et al., 2007] and non-linear force-free (NLFFF) extrapolations [Régnier et al., 2005]. Both methods remain imperfect. The main drawbacks of the constant-α field are that it is clearly wrong for active regions with field lines of clearly different twists [Burnette et al., 2004], and it places restrictions on α depending on the domain size. The second method has problems dealing with solving non-linear equations and with the use of ambiguity-resolved vector magnetograms in a non force-free photosphere (see [Demoulin et al., 1997] for further discussion). Applying different extrapolation methods to the same data was found to produce significantly different solutions [DeRosa et al., 2009].

---

[1] See Section 4.3 for description

A quantity that is easier to measure than helicity is the flux of helicity through the photosphere. It can be shown that for changing relative helicity, changes of magnetic flux at the boundary are far more effective than internal electric currents in the presence of high connectivity [Berger, 1984]. This allows one to express the change in the magnetic helicity in the corona through apparent motions of photospheric magnetic features, as first suggested by [Chae, 2001] and later developed by [Démoulin & Berger, 2003].

The theoretical prediction that the coronal helicity is injected from underneath the photosphere is not supported by much observational evidence. Only a few works compare integrated helicity flux through the photosphere to coronal helicity. [Pevtsov et. al., 2003] have studied the evolution of coronal α and found that its evolution is consistent with theoretical estimates of such for an emerging twisted flux tube. [Burnette et al., 2004] have found a correlation between coronal α of a linear field (chosen to visually match most of SXR loops) and α measured in the photosphere using vector magnetograms (averaged, in some sense, over the whole active region). [Lim et al., 2007] have found that helicity injection through photosphere (obtained using local correlation tracking) is consistent with the change observed in corona after taking account, approximately, of helicity carried away by CMEs; they assume linear field and a typical value for a helicity in CME. Comparisons of the change in coronal helicity with helicity of interplanetary magnetic clouds have demonstrated both a clear correspondence of the two [Mandrini et al., 2004] and a lack of such [Green et al., 2002].

In the current work we study an emerging active region over a long period of time with high temporal cadence. We compute a rate with which coronal helicity[2] changes and find that this rate is consistent with rate of helicity injection through the photosphere, reported for the same active region by [Longcope et al., 2007]. This is the first time (of which we are aware) that the helicity *change rate* in the corona over long period of time has been found to be consistent with the helicity flux in the photosphere.

We approximate the state of the coronal field using a method recently proposed by [Malanushenko et. al., 2009b]. It approximates coronal loops with lines of constant-α field like the above mentioned works, however, it allows α to vary from line to line. That is, each of the coronal loops is approximated by a field line of a different constant-α field. Strictly speaking, this approach is wrong, as a superposition of linear force-free fields will not resemble a force-free field at all. [Malanushenko et al., 2009b] argued that it might work for some cases relevant to the solar corona and have supported the reasoning with tests on analytical non-linear (or non-constant-α) force-free fields [Low & Lou, 1990] with amount of twist comparable to one typical to solar active regions as reported by [Burnette et al., 2004].

---

[2] Or rather a quantity closely related to it. The reasons for choosing this quantity will be clear in Section 4.3.

This method of determining properties of coronal loops does avoid some of the problems faced by linear or non-linear extrapolations. We will henceforth refer to it as (Non)-Linear Force-Free Field or shortly (N)LFFF[3]. It bears less uncertainty than a linear extrapolation, as α is allowed to vary in space. Also it is immune to some of the drawbacks plaguing non-linear extrapolations; in particular, it does not use vector magnetograms (which are obtained in the photosphere, where the force-free approximation is questionable, see [Demoulin et al., 1997] for further discussion) and does not attempt to solve non-linear equations.

The chapter is organized in the following manner. In Section 4.3 we review the methodology, describe the measured quantity and establish its relation to helicity. In Section 4.4 we describe the data to be used. In Section 4.5 we summarize results and findings from the data analysis. Section 4 contains the discussion of the results achieved. The Appendix B explains tangent plane projection and why it was chosen for the present work.

4.3. The Method

Most active region coronal magnetic fields are believed to be in a force-free state, given by Equation (3.1), where α is a scalar of proportionality [Nakagawa et al., 1971]. Extrapolations of coronal magnetic field usually imply solving this equation using photospheric data as a boundary condition. When $\nabla\alpha = 0$, Equation (3.1) reduces

---

[3] We are grateful to Carolus Schrijver for this name.

to a system of linear equations and thus is called linear or constant-α field. When α varies in space, Equation (3.1) represents a non-linear system and the solution is called a non-linear of non-constant-α field.

In the present work we use linear fields confined to half space, computed using Green's function from [Chiu & Hilton, 1977]. Such fields are less popular than linear fields confined to a box [Alissandrakis, 1981] because it takes much more computational time to build them. We use them, however, because they do not impose restrictions on α based on the size of the computational domain and because the field lines are allowed to leave the computational domain. We believe this is a better representation of coronal magnetic fields.

The result of the procedure of [Malanushenko et al., 2009b] is a line of a constant-α field[4] best-fitting a coronal loop for every visible loop. This gives the following set of parameters for every coronal loop that was successfully fit: its α, shape $\mathbf{r}(l)$ and the profile of magnetic field $\mathbf{B}(l)$.

In the current work we do not compute a helicity, but rather a quantity related to it, $\alpha_i L_i/2$ (where L_i is the length of i-th field line and α_i is its α). Most classical definitions of helicity involve a volume integral, which requires knowledge of magnetic field on a grid or analytically in a volume. (N)LFFF does not provide such gridded data or even volume-filling data. However, $\alpha L/2$ is closely related to helicity. For example, self-helicity of a uniformly twisted torus is $H = Tw\Phi^2$,

---

[4] Note that even for non-linear force-free fields $\alpha =$ const along every field line, of $\nabla\alpha \cdot \mathbf{B} = 0$. This result is obtained by taking the divergence of both sides of Equation (3.1) and using $\nabla \cdot \mathbf{B} = 0$ and the identity $\nabla \cdot (\nabla \times \mathbf{B}) = 0$, so that $\mathbf{B} \cdot \nabla\alpha = 0$.

where Tw is a number of turns that a field line makes per unit length and Φ is a net flux [Berger & Field, 1984, Moffatt & Ricca, 1992], and for a thin cylindrical uniformly-twisted flux tube[5] it can be shown that $2\pi Tw = \alpha L/2$ over axial distance L [Aschwanden, 2006].

It is not immediately clear, that the same expression could be used for a more complex flux configuration when thin flux tube approximation is not applicable. However, [Longcope & Malanushenko, 2008] have demonstrated how additive self helicity (helicity of a field relative to a potential field confined to the same domain) is consistent with an empirical function $\alpha\langle L_i\rangle\Phi^2/4\pi$ with $\langle L_i\rangle$ being the average length of a field line in the domain[6] and Φ being the total flux in the domain. This was shown for a case when the thin flux tube approximation was clearly inapplicable: for a constant-α synthetic field of a quadrupolar field confined to a box, for a domain, connecting two polarities. Later [Malanushenko et al., 2009a] suggested that "flux-normalized" additive self helicity could be treated as a generalized twist, $H_A/\Phi^2 = Tw_{gen}$ for an arbitrary magnetic configuration. That leads to a conclusion that

$$2\pi Tw_{gen} = \alpha\langle L_i\rangle/2, \tag{4.1}$$

in a similar manner as in thin flux tubes, at least in *linear* force-free fields. [Malanushenko et. al., 2009] demonstrated that Tw_{gen} is equal to Tw for a thin flux tube and that it

---

[5] Thin flux tube approximation usually refers to a structure with well-defined axis, with diameter small compared to its length and with radius of curvature large compared to its diameter.

[6] By "domain" we mean the same thing as [Longcope & Malanushenko, 2008] and [Malanushenko et al., 2009a]. It is a volume occupied by field lines connecting two given footpoints, so there is no magnetic flux across the boundaries of such a volume, except at the footpoints.

behaves like Tw in arbitrary magnetic configurations, for example, serving as a kink instability threshold. We hereafter refer to $Tw_{gen} = H_A/\Phi^2$ as "twist".

To the best of our knowledge, such relationship between α and helicity has not been established for general non-linear force-free fields. However in a thin *non-uniformly* twisted cylinder it might be expected that Tw_{gen} would be proportional to axial length with a constant of proportionality, that should reduce to α if the cylinder were uniformly twisted. For a more complex configuration Tw_{gen} might be expected to be proportional to some length scale times a constant that has dimensions of α. We choose to use a quantity $\langle \alpha_i L_i/2 \rangle$, averaged over many field lines as a proxy of Tw_{gen} and find that it changes consistently with the injection of coronal twist.

We compare this quantity to the normalized helicity flux across the photosphere, measured by [Longcope et al., 2007]. They split flux of unconfined self helicity (of a field confined to half space relative to the potential field in half space) into two parts: the "spinning" and the "braiding" contributions, as illustrated in Figure 47. The first one comes from rotation of footpoints about their axis and its change rate was expressed by [Longcope et al., 2007] through the average spinning rate $\dot{\theta}_{spin}$ as:

$$\dot{H}^a_{spin} = -\frac{1}{2\pi}\Phi_a^2\dot{\theta}^a_{spin}, \tag{4.2}$$

for a-th footpoint. The second one comes from the relative rotation of footpoints and its change rate could be expressed through the average tilt angle $\theta_{braiding}$:

$$\dot{H}^{ab}_{braiding} = -\frac{1}{\pi}\Phi_a\Phi_b\dot{\theta}^{ab}_{braiding}. \tag{4.3}$$

$\dot{H}_{spin}$ and $\dot{H}_{braiding}$ are not equivalent to fluxes of "twist" and "writhe" helicities [Berger & Field, 1984, Moffatt & Ricca, 1992]. In addition to the discussions in [Longcope et al., 2007] and [Longcope & Malanushenko, 2008], we would like to provide an illustrative example of this statement. Consider a thin untwisted torus from Figure 47 (a), deformed in the following way: first, the footpoints are rotated about each other by θ, then each of the footpoints is rotated about its own center by $-\theta/2$. This transformation is equivalent to a rotation of the whole torus as a rigid body and adds no helicity to it. However, an observer, who believes that $\dot{H}_{braiding}$ is equivalent to the flux of writhe helicity, might consider that the writhe helicity has increased by $\Phi^2\theta/\pi$. This is certainly not true, as the resulting configuration has no twist in it. [Longcope et al., 2007] argued that "spinning" and "braiding" fluxes of helicity might be produced by different physical processes.

Combining Equations (4.2) and (4.3) and noticing that for a flux-balanced dipole $\Phi_a = -\Phi_b$, we get:

$$\dot{H}_{total}/\Phi^2 = -\frac{1}{2\pi}\left(\dot{\theta}^a_{spin} + \dot{\theta}^b_{spin} - 2\dot{\theta}^{ab}_{braiding}\right). \tag{4.4}$$

From Equations (4.1) and (4.4) it follows, that if the quantity $\langle\alpha_i L_i\rangle/2$ is roughly proportional to H/Φ^2 in a non-linear field, its change rate should be proportional to $-\left(\dot{\theta}^a_{spin} + \dot{\theta}^b_{spin} - 2\dot{\theta}^{ab}_{braiding}\right)$. We would like to note, that $\langle\alpha_i L_i\rangle/2$ is really meant to represent Tw_{gen} and thus be relevant only to the additive self-helicity H_A, that is to helicity of the field in a subdomain relative to the potential field in the same subdomain, and H_{total} is the helicity of the field in half space relative to potential field in half space (see [Longcope & Malanushenko, 2008] for further discussion). However, the difference $H_{total} - H_A$ only depends on the shape of the subdomain and both [Longcope & Malanushenko, 2008] and [Malanushenko et al., 2009a] have studied the cases with subdomains of relevant shapes and found this difference to be small (except at the pre-CME state).

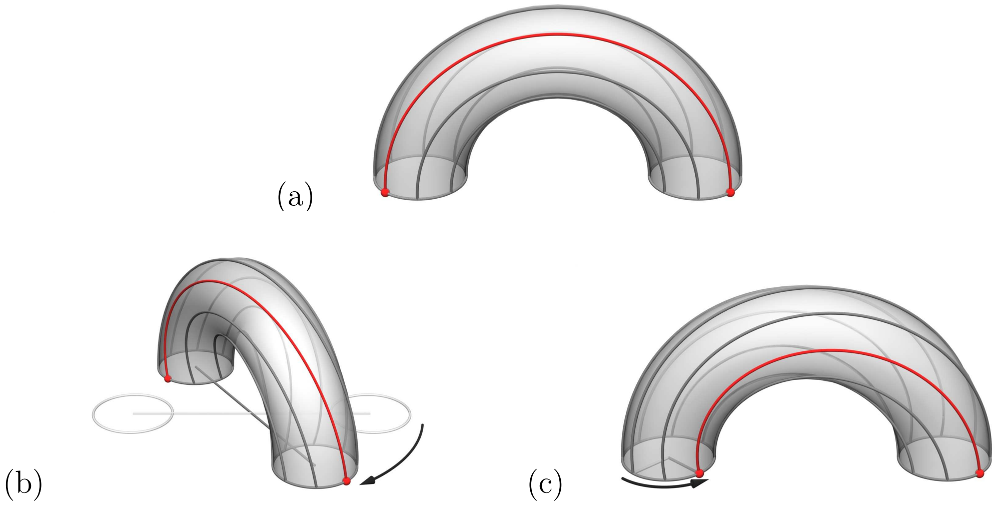

Figure 47. A schematic illustration of braiding and spinning motions of footpoints. (a) An untwisted torus. (b) A configuration that results from relative rotation of the footpoints (braiding). (c) A configuration that results from rotation of one of footpoints about its center (spinning). In general case, the total injected helicity is proportional to $\theta = \theta_{pos.spin} + \theta_{neg.spin} - 2\theta_{braiding}$.

4.4. The Data

The present study is devoted to AR 9004. It was emerging, as its flux was increasing. [Longcope et al., 2007] managed to follow its evolution beginning at a time it had about 30% of its final flux. The other feature of this active region is that

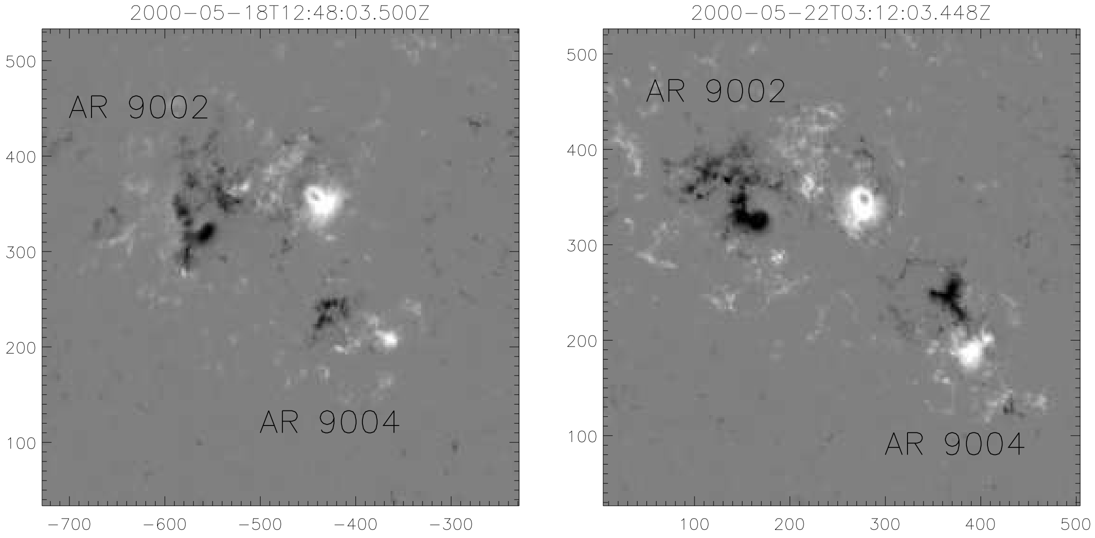

Figure 48. We studied the region with AR's 9002 and 9004 from 2000-05-18 12:48:03 till 2000-05-22 03:12:03. AR 9002 was an old diffuse active region and AR 9004 was emerging and rapidly rotating active region.

its footpoints were rotating about each other and about themselves at measurable pace. The measurements of the rotation were performed by [Longcope et al., 2007].

We chose 21 full-disk MDI magnetograms in the time range between 2000-05-18 12:48 and 2000-05-22 03:12. The first and the last images are shown in Figure 48.

The magnitude of the magnetic field on each magnetogram was corrected for the foreshortening factor, assuming the magnetic field to be purely radial: $B_z(x, y) = B_{los}(x, y)/\sqrt{1 - \rho(x, y)^2/R_\odot^2}$, where $\rho(x, y) = \sqrt{x^2 + y^2}$ is the plane-of-the-sky distance from the disk center to the point (x, y). Each magnetogram was then remapped to the disk center in orthographic projection (see Appendix B).

For each magnetogram we selected several (typically two) TRACE 171Å images taken within 30 minutes of the magnetogram. The selection criteria was the visibility of many distinct coronal loops. On each TRACE image as many loops as could be discerned were "traced", or visually approximated with a smooth curve, a two-segment Bézier spline (e.g., [Prautzsch et al., 2002]).

Each magnetogram on the tangent plane was rebinned on a coarser grid, half the size in each dimension, and then used to construct 41 constant-α fields with $\alpha \in [-0.05, 0.05]$ arcsec^{-1} and with step of $\Delta\alpha = 0.0025$ arcsec^{-1} in a box with $z_{max} = 200$ arcsec and $\Delta z \approx 1.5$ arcsec. Both ranges of α and z have proven to be sufficient to reconstruct most of the loops. For every "traced" coronal loop we traced many field lines along the line of sight from the midpoint of the loop, as illustrated in Figure 49. The procedure was repeated for all constant-α fields. Each field line (that is described by α of the constant-α field it belongs to and the coordinate along the line of sight h) was projected onto the plane of the sky. The mean distance $d(h, \alpha)$ between this projection and the traced loop was computed. Then the minimum of $d(h, \alpha)$ on a grid of given values α and h was found following a semi-automatic algorithm described in [Malanushenko et al., 2009b].

We found that for many loops ($\sim$55% of all 301 loops) the general shape of the $d(h, \alpha)$ parameter space matches one of the types described in [Malanushenko et. al., 2009]. As for the "undescribed" types, we chose not to ignore them, but try to identify anything that looks like the non-hyperbolic valley and choose a local minimum on it that resulted in visually better fit. Among those "undescribed" types of parameter spaces there was one that has found to occur frequently enough ($\sim$ 36%

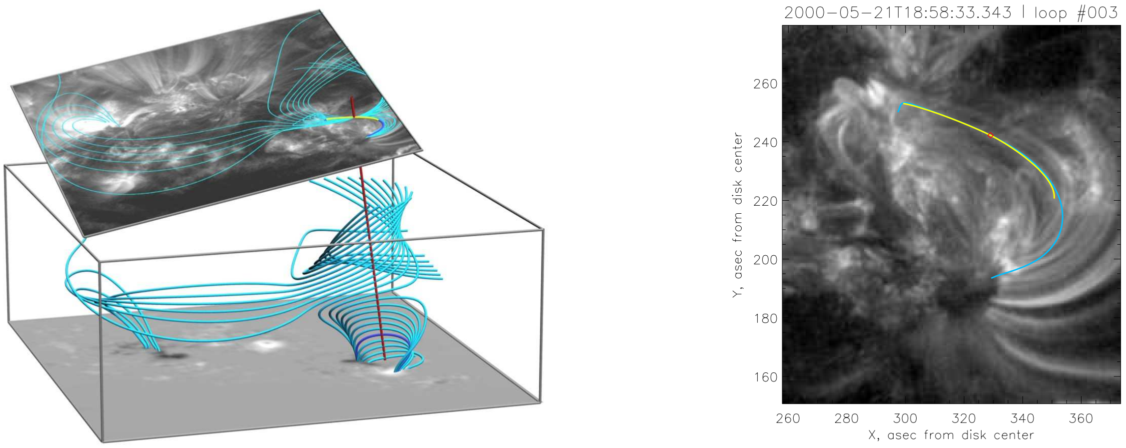

Figure 49. *(left)* – TRACE image in the plane of the sky and de-rotated MDI images shown with their respective angles. For every coronal loop (yellow) the algorithm browses through several different constant-α fields. In each field it traces field lines (cyan) along the line or sight (red). The field lines are than projected back to TRACE image and compared to the loop using the semi-automatic selecting algorithm. Best-fit field line is shown in darker shade of blue. (Field lines are of $\alpha = 0.025$ arcsec^{-1}, that corresponds to the best-fit α for this particular loop, so the dark blue line is the resulting best-fit line for this loop.) Gray box shows the actual computational domain. *(right)* – a fragment of the TRACE image in the plane of the sky, the traced loop (yellow), the projection of the best fit to the plane of the sky (cyan) and the midpoint of the loop (red).

of all loops) to warrant new classification. The "anomalous" (or "non-hyperbolic") valley in the parameter space of this type looked like two branches at each side of $\alpha = 0$ line joined together (see Figure 50). According to the algorithm from [Malanushenko et al., 2009b] such a loop had to be either ignored or the local minimum on this valley that corresponded to lowest height was to be chosen. We found that such a choice results in visually much worse fit than chosing the global minimum of this valley. We thus proceeded with selecting the global minimum on the non-hyperbolic valley. This type of the parameter space had not been found on tests in analytic data and there is no clear indication that it is trustworthy, except for the better visual correspondence to the coronal loops. We believe it might represent a distortion of "conventional" shapes due to the inclination of the line of sight. We would like to mention that such classification of parameter spaces is subjective and sometimes ambiguous, but it has been found to yield statistically reasonable results when tested on analytical fields.

This procedure resulted in a "best-fit" line of a constant-α field for every coronal loop. The quality of the fit was visually judged and assigned a subjective grade between 0 (unsuccessful fit) and 1 (perfect fit). For further analysis, only loops that had a fit quality greater than 0.7 were used. For example, the fit in Figure 50 was given a quality grade of 0.7 and the fit in Figure 49 was judged to be of quality 1.

4.5. Results

We have performed the reconstruction procedure for the total of 303 coronal loops of AR 9004. 61 of them (20%) had quality 0.7 and 219 (73%) had quality 1, so in total there were 280 (93%) successful reconstructions. The real percentage of the successful fits might be slightly lower, as some coronal loops seeming to belong to AR 9004 on EUV image were reconstructed as open field lines or as field lines interconnecting ARs 9002 and 9004, and some of those fits have failed as well. We could have estimated how many loops seemed to have incorrect reconstructed connectivity, but we chose

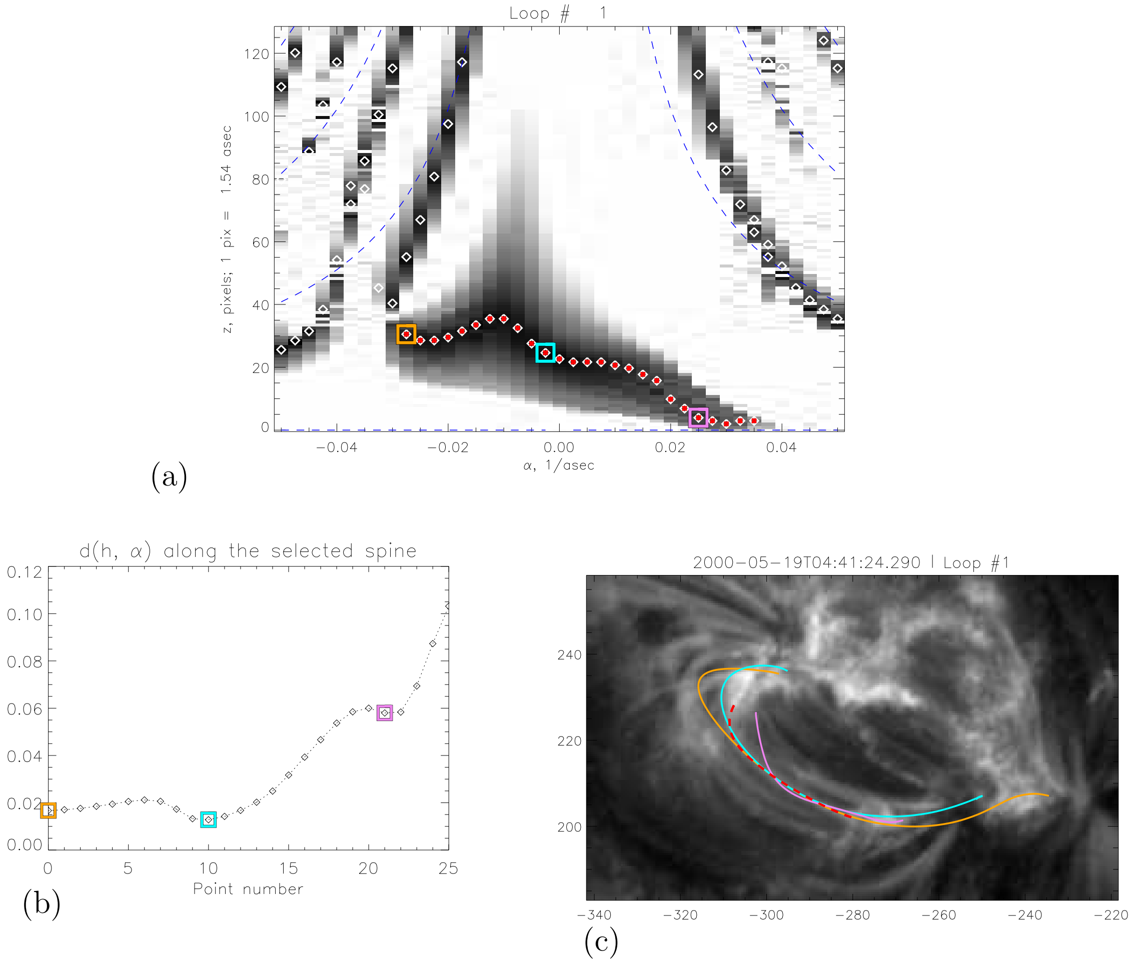

(a)

(b)

(c)

Figure 50. A type of parameter space, not described in [Malanushenko et al., 2009b] on tests with analytic fields. (a) — The parameter space. White diamonds: local minima in columns. White diamonds with red dots: selected "non-hyperbolic" valley. Three colored squares: points that correspond to the local minima on this valley. Blue dotted lines: hyperbolas $h = n\pi/\alpha$, $n = 0, \pm1, \pm2, \ldots$. (b) — $d(\alpha, h)$ along the selected valley. (c) — A fragment of TRACE 171Å image with the traced loop (dashed red) and three field lines, corresponding to the three local minima. It seems that the one, corresponding to the lowest h (magenta) is visually a much worse fit than the one, corresponding to the global minimum on this valley (cyan). We consider the valley to the left of the 'hump' a different valley, that could have been a degenerate hyperbolic. Based on this, we decide that the cyan line should be used. We update the algorithm from [Malanushenko et al., 2009b] with the parameter space of this type.

not to do so. The reason is that it would involve visual estimation of the connectivity that may or may not be right on its own.

The following evolution was observed:

- Up to $t = 35.5$ hrs[7] (images 1-7 in Figure 53) the loops had *mainly negative (left-handed) twist* and the median twist has decreased in magnitude.
- From $t = 48.2$ hr to $t = 51.7$ hr (images 10-11 in Figure 54) had *twist of both signs*, with negative twist predominantly in the eastern half of the dipole and positive twist predominantly in the western half. The median was close to zero. (Only half of the region was seen on images 8 and 9, so we could not draw any conclusion about spatial structure of the twist from $t = 38.0$ hr to $t = 41.3$ hr.)
- Most of the loops on image 12, $t = 54.6$ hr, had twist of positive sign.
- The loops on image 13, $t = 58.9$ hr, were *poorly fit.* As suggested in [Malanushenko et. al., 2009], this might indicate that the field was strongly twisted or maybe strongly non-linear.
- Almost no loops of AR 9004 were observed and well fit on images 14-16 ($t = 64.0$ hr to $t = 70.3$ hr). It is possible that the existing loops were *outside* of TRACE field of view.
- Most of loops on images 17-21 ($t = 72.2$ hr to $t = 99.4$ hr) had twist of positive sign (or right-handed twist). The median twist appeared to be slightly increasing.

The emergence of AR 9004 was evident from the evolution of the magnetic flux. The magnetic flux, according to [Longcope et al., 2007], was steadily increasing until

---

[7] All times are in hours since 2000-05-18 00:00:00.

about $t = 55$ hrs, and after that it exhibited a slight decrease. This decrease was contemporary with the drop in the combined twist angle in Figure 51.

For any given time there was a wide distribution of measured twist. There was, however, a general trend for the twist to increase. While most of the loops were negatively twisted at early times, most of loops at later time exhibit positive twist.

We summarize the findings in Figure 52. Each point there represents $\alpha L/2$ of a single loop versus time when it was measured. At every time we find a mean twist and mean of the absolute deviation (this way the time frames with many data points would not be given more weight in the fitting procedure than the time frames with few data points). We then fit a line to the twist as a function of time using least absolute deviation fit to the means using the mean of the absolute deviation. We only fit the line in the time interval from $t = 10$ hrs to $t = 55$ hrs. The start time is the earliest time available and the final time is where the photospheric twist starts to decrease. We have measured $\langle \alpha L/2 \rangle$ to increase at about 0.021 rad/hr.

Figure 51 shows the twist injection rate as measured by [Longcope et al., 2007] as a black curve. It also shows individual spinning (red for positive and blue for negative) and tilt (green) angles. We fit a line to the combined angle using least absolute deviations to the same time interval as on the coronal measurements and find a twist injection of about -0.0160 rad/hr.

We conclude, that the rate of change of the coronal twist is consistent with the twist injection through the photosphere.

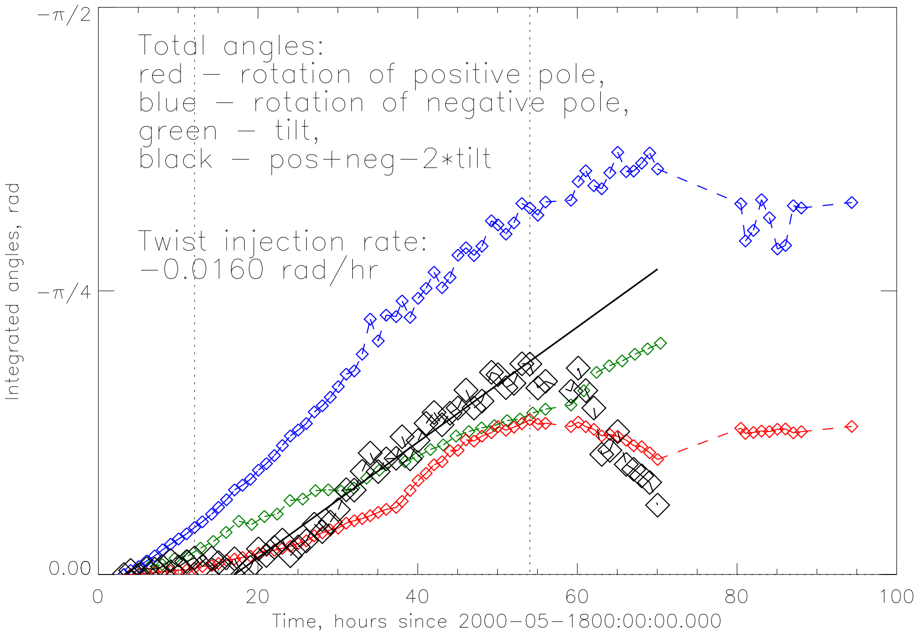

Figure 51. Twist rate, as measured by [Longcope et al., 2007]. The data points within time interval from $t_0 = 12$ hours to $t_1 = 57$ hours were fit to a line with least absolute deviations. The lower boundary of the interval was chosen to be the lower boundary for (n)lfff data and the upper boundary was chosen where the linear twist injection was no longer obvious.

4.6. Discussion

In the current work we have observed how helicity flows into the corona through photospheric motion. In the beginning of the time sequence coronal loops of AR 9004 appear to have negative helicity and after about 60 hours all the coronal loops appear to have positive helicity. We have observed that when a negatively twisted field is subject to the injection of helicity of positive sign, magnetic field does not pass through the potential state. Rather, it passes through a complex non-linear

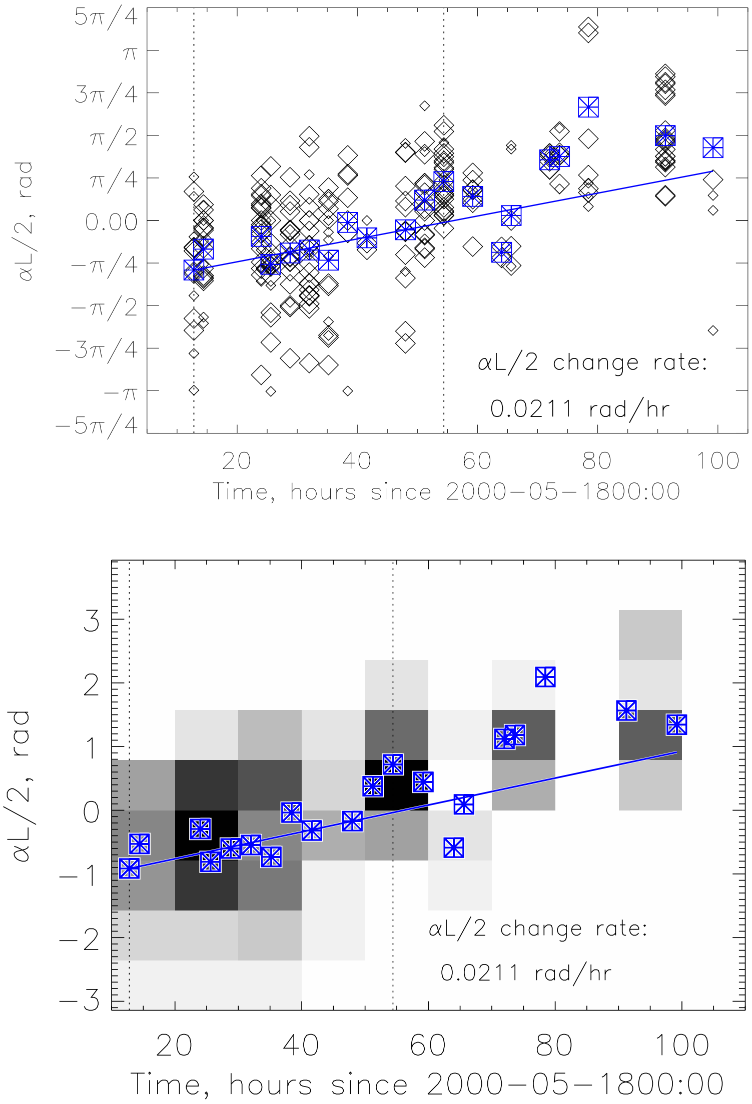

Figure 52. Twist of coronal loops versus time, using (n)lfff reconstruction from [Malanushenko et al., 2009b]. *(top)* — Diamonds show twist of individual loops (larger correspond to quality 1 and smaller to quality 0.7). Blue squares are medians for each individual time. The line shows least absolute deviation to the means with means of the absolute deviations fit to the diamonds within the selected time range (same range as in Figure 51). *(bottom)* — A histogram showing time-twist distribution of coronal loops makes the trend evident. Black color corresponds to 20 points or more and white corresponds to one or no points.

equilibrium that has parts with distinct positive and parts with distinct negative twist.

There were two weak flares associated with AR 9004 in the examined time interval, according to Solar Monitor [Gallagher et al., 2002]. These included one C2.7 flare at $t = 52.6$ hrs and then a C1.9 at $t = 88.6$ hrs. [Kusano et al., 2003] have proposed a model in which the field of an active region, featuring twist of both signs, undergoes magnetic reconnection. This process is accompanied by a flare and results in an untwisted magnetic field (that is, with zero helicity). The flares in AR 9004 do not seem to be associated with confident drops of twist. Moreover, the AR that we study does have twist of both signs at $t \in [20, 55]$ hrs and yet does not seem to relax to a potential state at later times, after $t = 72$ hrs. It is worth noting, however, that in the period of $t \in [58.9, 70, 3]$ hrs there were almost no loops that were successfully fit, leaving open the question of what might have happened at that time. It could be argued that the field indeed had relaxed to the potential state and its further positive (right-handed) twist was injected through the photosphere, but at least the apparent injection of negative helicity within about $t \in [55, 70]$ hrs (evident in Figure 51) suggests that this might not be the case.

We have studied the time rate of change of the following quantity: $\langle \alpha_i L_i / 2 \rangle$ averaged over many reconstructed field lines. In Section 4.3 we argued that it might be proportional to the additive self helicity [Longcope & Malanushenko, 2008] of a non-linear field in the similar manner as $\alpha L/2$ is proportional to twist helicity of a thin flux tube and as $\alpha\langle L_i\rangle/2$ is related to additive self helicity for a linear force-free field.

We have found that the time rate of change of $\langle\alpha_i L_i/2\rangle$ (and arguably a generalized twist, $Tw_{gen} = H_A/\Phi^2$) is found to be about 0.021 rad/hr. This rate is similar to the time rate of change of the flux-normalized total helicity H_{total}/Φ^2 (or unconfined self helicity, of a field in half space relative to potential field in half space) that was found to be 0.016 rad/hr. We would like to mention, that H_A and H_{total} differ from each other by a helicity of potential field confined to the domain containing the dipole of interest relative to a potential field with the same footpoints confined to half space; however, for configurations studied in [Longcope & Malanushenko, 2008] and [Malanushenko et al., 2009a] this difference was found to be small. This gives a hope that we are measuring different, yet close quantities in the present work.

The difference between H_A and H_{total} might be responsible for the fact that even though H_{total} starts to decrease after about $t = 55$hrs, the twist derived from coronal loops remains of a positive sign and does not show any signs of decrease. We have noticed that a lot of bright coronal loops connecting ARs 9004 and 9002 appear at about $t = 75$hrs and later at about $t = 100$hrs. It is possible that while photospheric helicity injection changes sign, magnetic reconnection that happens after that changes the balance between "twist" and "writhe" helicities[8]. In the current paragidm magnetic reconnection results in a decrease of magnetic energy. It is also true that linear

---

[8] In the sense of H_A as a "generalized twist helicity" and $H_{total} - H_A$ as a "generalized writhe helicity".

force-free fields with larger α are typically thought of having larger magnetic energy than those with smaller α [Aly, 1992]. However the field of AR 9004 was found to be non-linear, which means, for the same system there exists a linear force-free field with lower energy [Woltjer, 1958]. A possible scenario for the observed phenomena is the following: magnetic reconnection between ARs 9004 and 9002 lowers the total magnetic energy and possibly turns AR 9004 to a linear (or nearly linear) force-free field. Total helicity of AR 9004 is decreased due to photospheric motions, however, its self-helicity stays nearly constant, signifying a decrease of "generalized writhe helicity". The latter appears to be only a function of the shape of the domain containing field of AR 9004. So both magnetic reconnection (that has decreased the volume of this domain by reconnecting some of the flux to AR 9002) and photospheric motions might have contributed to that.

This work was supported by NASA under grant NNX07AI01G and NSF under award ATM-0552958.

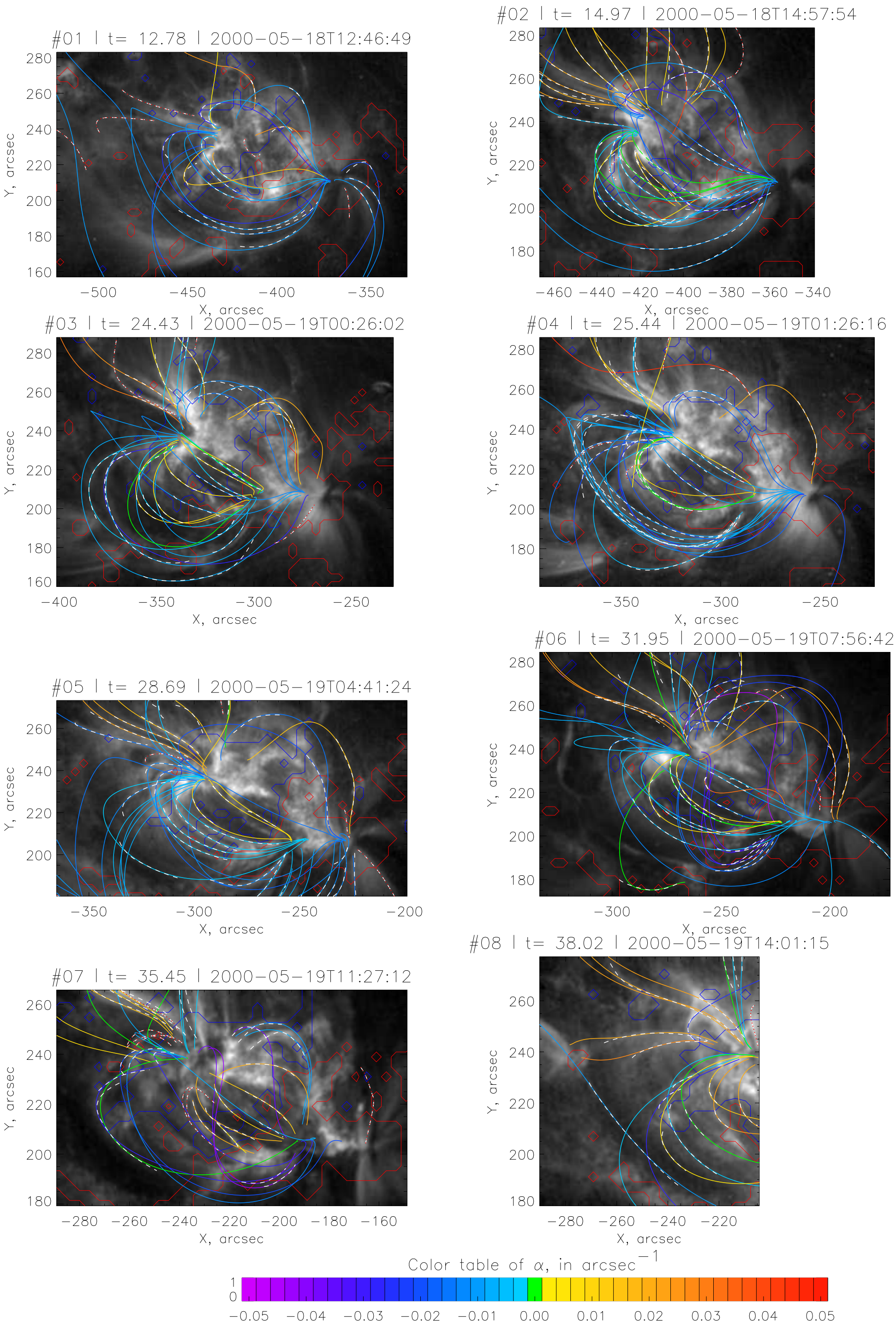

Figure 53. All reconstructed field lines of quality 0.7 or 1 (solid lines). Their color corresponds to α. The original coronal loops are shown as dashed white (for successful reconstruction) or dashed red-white (for unsuccessful). Different image sizes are due to different amount of data within the field of view. The image sequence continues in Figure 54.

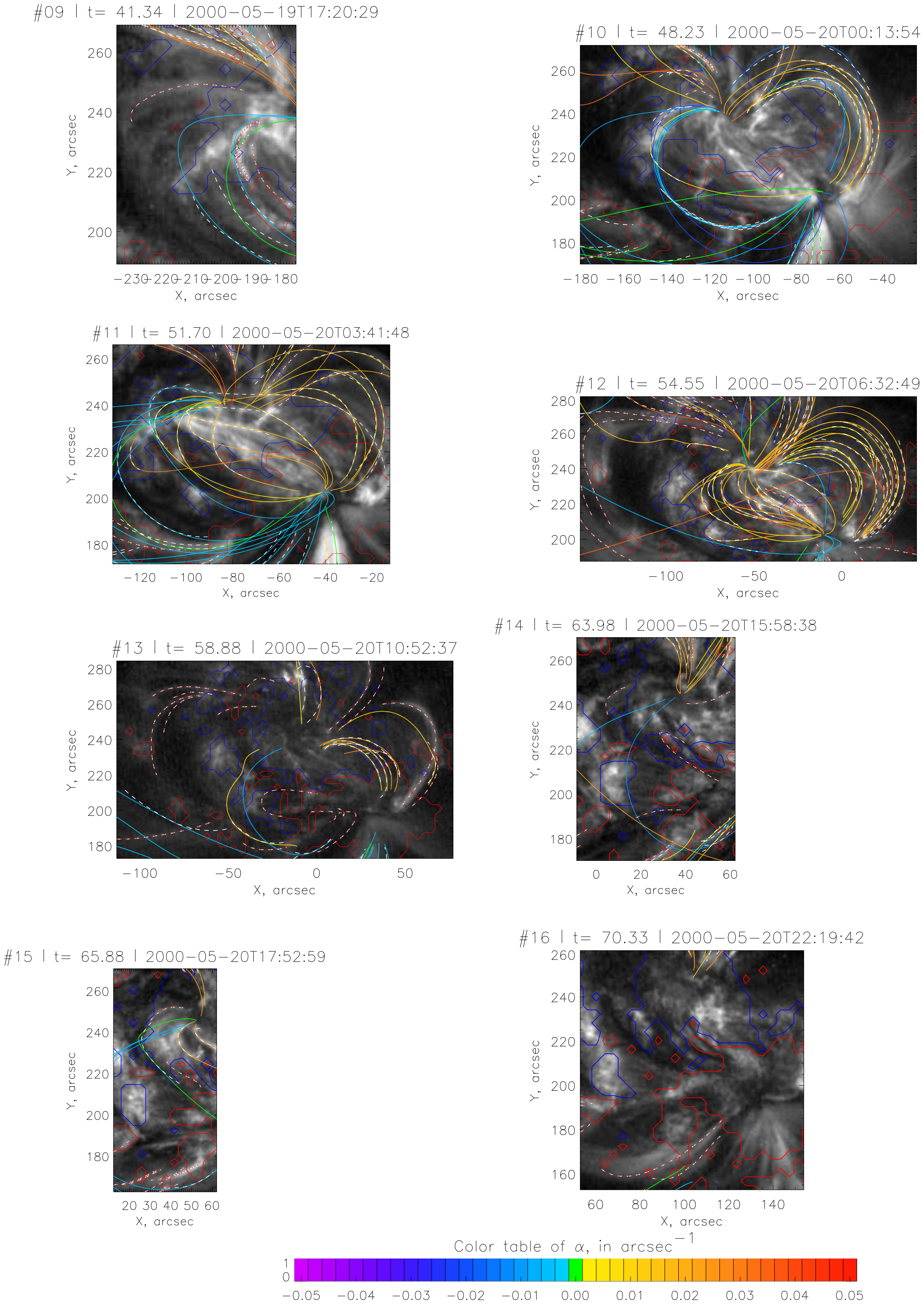

Figure 54. Continuation of Figure 53.

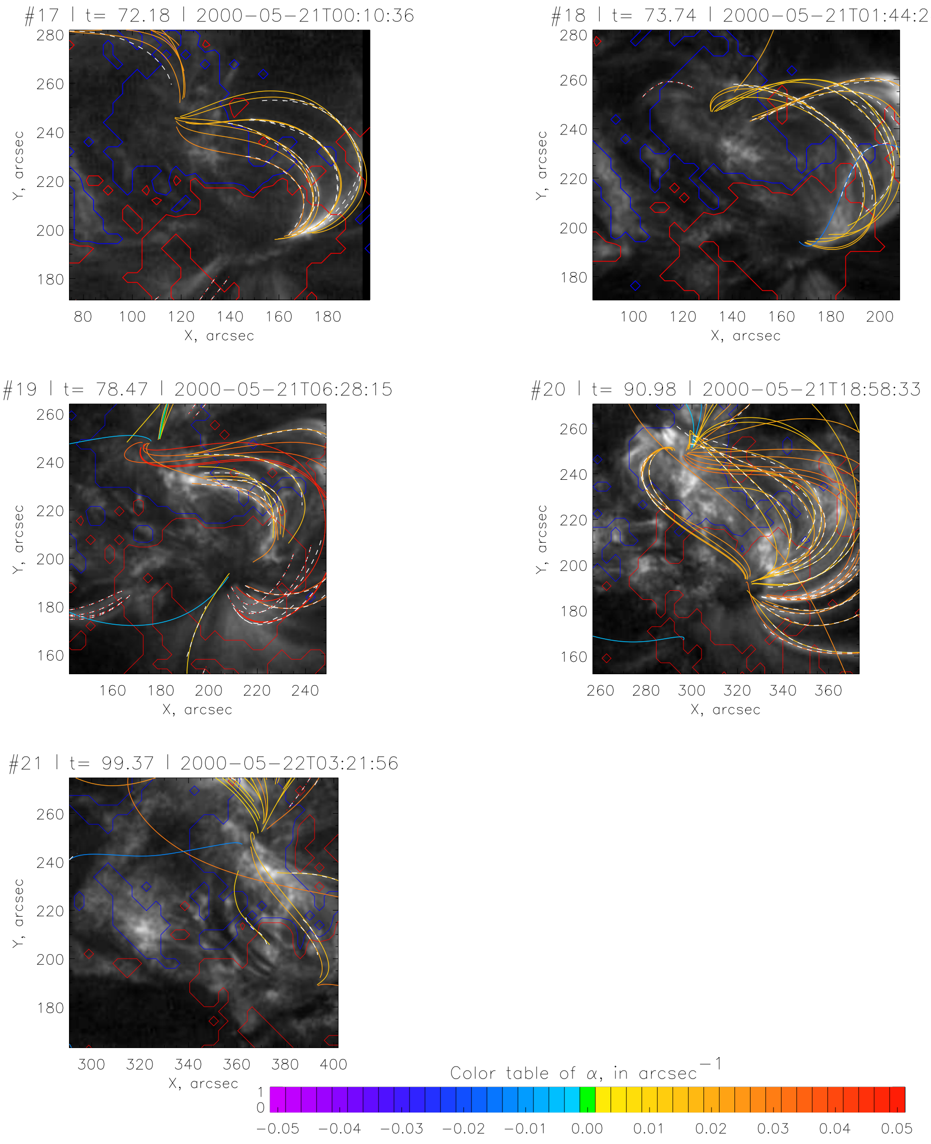

Figure 55. Continuation of Figure 53.

5. CONCLUSIONS

Novel results. Applications to Solar Physics.

Possible improvements of the methods.

In this dissertation I was able to systematize and verify several *generalizations* of important topological quantities developed for a thin flux tube. In particular, a generalization of Tw via H_A for structures of arbitrary shape was found to have practical applications for studies of kink instabilities. Another generalization that was verified is the relation of $\langle \alpha L/2 \rangle$ to Tw_{gen} in a structure of arbitrary shape in the similar manner as $\alpha L/2$ is related to Tw in a thin axisymmetric structure. It is not entirely clear, what would be the threshold value, similar to Equation (1.17), for an equilibrium of an arbitrary shape. The numerical methods developed within this thesis make such studies possible.

In the course of this work, an extremely promising tool was developed and carefully tested. This tool allows for a three-dimensional reconstruction of coronal loops based on as little information as a line-of-sight magnetogram and one projected image of the solar corona in the EUV or Soft X-Ray.

While many of the individual parts of this method were presented in earlier works, as shown in Table 3, (N)LFFF is novel in several aspects. This includes tests on analytic data, nontrivial improvements of the fitting algorithm and the use of unconfined magnetic fields[1].

There is one more aspect of (N)LFFF that makes it novel. The whole method is based on the following statement:

> *For a field line of a NLFFF, there would be a field line of a LFFF that is close in shape; this LFFF has α similar to the one of the field line of the NLFFF.*

This is not true in general, as was explained in Chapter 1. But there are some arguments of why in some cases it might be approximately true in the solar corona. The tests on analytic cases support this hypothesis. The first study of twist in solar corona made with (N)LFFF is in agreement with the theoretical predictions. The success of (N)LFFF is strong evidence in favor of the highlighted statement.

(N)LFFF reconstruction has a wide range of possible applications within Solar Physics. These include:

- Detailed information of coronal currents on a sparse set of curves in space. This might help to construct better NLFFF models and improve the results of [DeRosa et al., 2009].

---

[1] The latter are less popular because of the extensive computing time, however, are more rewarding as they lay no restrictions on the magnitude of α and are physically a better approximation to the coronal field. Recent development of powerful computers makes such computations possible.

- An improved knowledge of three-dimensional geometry of the coronal loops. This might be applicable to the problem of expansion of magnetic flux tubes [Lopez Fuentes et al., 2006].
- A potential for better studies of intensity profile along optically thin loops. This might aid in tackling the problem of heating of coronal loops [Klimchuk, 2009].
- The estimates of magnetic energy could be performed directly from the output of (N)LFFF using Monte-Carlo method. A manuscript on this topic is currently in preparation [Longcope and Malanushenko, 2010, in preparation]. Such estimates could aid in studies of energy storage and release in the solar corona.
- α of the magnetic field lines could be used to estimate Tw_{gen} from available observations. This might allow the study of magnetic instabilities in the solar corona in addition to the numeric simulations.

The developed methods and ideas have received one immediate application, described in Chapter 4. The evolution of Tw_{gen} was observed in the solar corona and compared to the evolution of photospheric field. The latter is believed to inject helicity and thus twist to the corona. Chapter 4 presents good observational evidence of this fact.

As with most new methods, (N)LFFF could be greatly improved. At the present stage it has several steps that require a human intervention. For the method to be easier to use, these steps should be automated. The visual selection of coronal loops could be replaced with an automatic detection using, for example, one of the algorithms from [Aschwanden et al., 2008]. The visual selection of the region in (α, h) space where the minimum is found to correlate with the real parameters of the loop, should also be automated, possibly, using one of the image recognition algorithms.

References	α-fit	LOS-fit	Numerical Fit	Error Analysis	Comment
[Nakagawa & Raadu, 1972, Pevtsov et al., 2003, Burnette et al., 2004]	+	−	−	−	Fit to footpoints; fit of all loops to one LFFF.
[van Ballegooijen, 2004]	−	+	+	−	Fit to a single NLFFF.
[Green et al., 2002, Lopez Fuentes et al., 2006, Lim et al., 2007]	+	−	+	−	Fit to footpoints; fit of all loops to one LFFF.
[Malanushenko et al., 2009b]	+	+	+	+	(N)LFFF. Chapter 3 of this dissertation.

Table 3. Comparison of the (N)LFFF reconstruction to some of the preceding methods.

APPENDIX A

ON LOW & LOW FIELDS.

[Low & Lou, 1990] constructed a class of non-linear force-free magnetic fields beginning with an axi-symmetric field. An axi-symmetric, divergence-free magnetic field can be written, in all generality, as

$$\mathbf{B} = \nabla A \times \nabla\phi \ + \ Q\nabla\phi = \frac{1}{r\sin\theta}\left(\frac{1}{r}\frac{\partial A}{\partial\theta}\hat{\mathbf{r}} - \frac{\partial A}{\partial r}\hat{\theta} + Q\hat{\phi}\right) \quad , \tag{5.1}$$

where $A(r,\theta)$ is the flux function and the azimuthal component is $B_\phi(r,\theta) = Q(r,\theta)/r\sin\theta$. The poloidal components of the force-free condition, $\nabla \times \mathbf{B} = \alpha\mathbf{B}$, are satisfied only if Q and α are each functions of the flux function alone

$$Q(r,\theta) = Q[A(r,\theta)] \ \ , \ \ \alpha[A(r,\theta)] = \frac{dQ}{dA} \quad . \tag{5.2}$$

The azimuthal component of the force-free condition

$$r^2\sin^2\theta \ \nabla \cdot \left(\frac{\nabla A}{r^2\sin^2\theta}\right) = -\alpha Q\frac{dQ}{dA} = -\frac{1}{2}\frac{dQ^2}{dA} \quad , \tag{5.3}$$

is known as the Grad-Shafranov equation for flux function A.

The Grad-Shafranov equation contains one free function $Q^2(A)$ for which Low and Lou took a particular form. We generalize their choice to

$$Q^2(A) = a^2\,|A|^{2+2/n} \quad , \tag{5.4}$$

where a and n are free constants. The absolute value signs, absent from the original formulation, are introduced here so that Q^2 is real, and non-negative, even where the flux function is negative. Equation (5.3) can then be made homogeneous in r by proposing a solution

$$A(r,\theta) = P(\cos\theta)\,r^{-n} \quad , \tag{5.5}$$

for a still-unknown function $P(\mu)$. Using this in the Grad-Shafranov equation, and defining $\mu = \cos\theta$, leads to the non-linear equation

$$(1-\mu^2)\frac{d^2P}{d\mu^2} + n(n+1)P = -a^2\left(1+\frac{1}{n}\right)|P|^{2/n}\,P \quad , \tag{5.6}$$

for the unknown function $P(\mu)$.

Equation (5.6) has real solutions for any a and any $n > -2$; n need not be an integer. Boundary conditions, similar to those of [Low & Lou, 1990], are $P'(1) = -10$ and $P(1) = 0$, so the solution is regular along the positive z axis. The solution will be regular along the negative z axis only when the solution satisfies the additional condition $P(-1) = 0$. For a given value of n this condition will be satisfied only for certain choices of the eigenvalue a. (Integer choices of n always have one eigenvalue, $a = 0$, for which $P(\mu)$ is $\sin^2\theta$ times the Legendre polynomial of order n.)

The final magnetic field, defined for $z \geq 0$, is constructed by rotating the axisymmetric field by angle Φ about the y axis and translating it downward a distance ℓ. For rotation angles $\Phi \leq \pi/2$ and non-vanishing displacement, $\ell > 0$, the origin and what had been the negative z axis lie in $z < 0$, outside our domain. This means the regularity condition, $P(-1) = 0$, is not needed to assure a regular magnetic field. We therefore make no restriction on $P(-1)$ and consider both n and a to be free parameters.

The function $Q(A)$, required for the final field of eq. (5.1), is found from the square root of eq. (5.4). When the solution $P(\mu)$ changes sign there can be more than one choice of square root for which $Q(A)$ is a continuous real function.[2] We focus on two such choices, we call signed and unsigned

$$Q_U(A) = aA|A|^{1/n} \quad , \tag{5.7}$$

$$Q_S(A) = a|A|^{1+1/n} \quad , \tag{5.8}$$

both of which satisfy eq. (5.4) when $A(r,\mu) = P(\mu)/r^n$ is real. Taking the derivative of these functions gives the twist parameters for the two cases

$$\alpha_U(A) = a\left(1+\frac{1}{n}\right)|A|^{1/n} \quad , \tag{5.9}$$

$$\alpha_S(A) = a\left(1+\frac{1}{n}\right)|A|^{1/n}\mathrm{sgn}(A) \quad . \tag{5.10}$$

The unsigned case has a single sense of twist determined by the sign of the constant a; the signed case has both senses provided A changes sign.

---

[2] There will be 2^m distinct choices when $P(\mu)$ changes sign m times over $-1 < \mu < 1$.

APPENDIX B

ON TANGENT PLANE PROJECTION

A tangent plane projection is an orthographic projection onto a plane, tangent to the Sun at the point which is called the center of the projection and the projection of the solar North directly upwards. It could easily be obtained from the plane of sky using the following transformations. In the starting plane of sky the coordinate system is assumed to be heliographic-cartesian [Thompson, 2006]. That is, Cartesian, with the origin at the Sun's center, x axis directed towards solar West in the plane of sky, y axis directed towards solar North in the plane of sky and z axis directed towards the observer. The image plane is then rotated as described by Equation 5.11: first, by $-b_0$ (where b_0 is solar B-angle) about x-axis, then by $-\phi_c$ (where ϕ_c is the longitude of the desired projection center) about the new y-axis, then by $-\theta_c$ (where θ_c is the latitude of the desired projection center) about the new x-axis. After this sequence of rotations solar North would lie on the new y-axis and solar West would lie on the new x-axis. The last step is to perform the orthographic projection in the new z direction, that is, simply to set z coordinate to 0 for all points in the visible hemisphere.

$$A_x(\theta) = \begin{pmatrix} 1 & 0 & 0 \\ 0 & \cos(\theta) & -\sin(\theta) \\ 0 & \sin(\theta) & \cos(\theta) \end{pmatrix}$$

$$A_y(\phi) = \begin{pmatrix} \cos(\phi) & 0 & \sin(\phi) \\ 0 & 1 & 0 \\ -\sin(\phi) & 0 & \cos(\phi) \end{pmatrix}$$

$$A = A_x(b_0)A_x(-\theta_c)A_y(-\phi_c)A_x(-b_0) \tag{5.11}$$

This projection is non-conformal (it does distort local shape) and distorts the distances. But those distortions are independent of the location of the point of tangency and only increase with the size of the desired box. For example (see Figure 56), if one considers a point on the sphere, which radius-vector from Sun's center $\mathbf{r}$ makes an angle γ with the radius-vector from Sun's center to the projection center, $\mathbf{r}_0$, then the distance on the sphere between $\mathbf{r}$ and $\mathbf{r}_0$ is $R\gamma$ and the distance between the projections of these two points on the tangent plane is $R\sin\gamma$. For $\gamma = 30^\circ$ (or the box of 60°, which is enough to fit most active regions), the foreshortening factor would be about 5%.

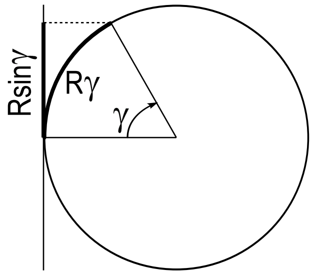

Figure 56. Distortions of distance on tangent plane projection are small if the size of the extracted region is small. For example, if a distance between the point of tangency and another point on the Sun is $R\gamma$, then (if $\gamma \leq \pi/2$) the distance between the center of the projection and the projection of that point is $R\sin\gamma$.

For purposes of tracking long time sequences and dealing with off-center solar images, heliographic coordinates (with longitude ϕ along horizontal axis and latitude θ along vertical) are often used, with the longitude either either equally spaced along the vertical axis [Thompson, 2006] or with spacing that changes with the distance from the equator [Welsch et al., 2009]. The first one is commonly referred in cartography as plate Carrée projection and a particular case of the second one frequently used in Solar Physics is called Mercator projection [Frederick Pearson, 1990].

A tangent plane projection that we use is somewhat less common. The first reason why we chose it is that the distortions are independent of latitude (unlike for Mercator or plate Carrée projections, which have systematic latitude-dependent errors), as explained above. The second reason why we choose the tangent plane projection is that it is distorts global shapes less than cylindrical projections. Since the shape of a coronal loop is crucial for determining its α, we believe it is more important to conserve shapes globally rather than locally, and orthographic projections are better in this sense than the cylindrical ones. For example, let us consider a $30^\circ \times 30^\circ$ "square" $ABCD$, centered at 0°W, 15°N (roughly the size and position of ARs 9002 and 9004 when they pass through the central meridian), as shown in Figure 57. The lengths of the arches on the sphere are $AB = BC = AD = \frac{\pi}{6}R_\odot \approx 0.524R_\odot$ and $CD = \frac{\pi}{6}\cos\frac{\pi}{6}R_\odot \approx 0.454R_\odot$, so $CD/AB \approx 0.86$. In a cylindrical projection $CD/AB = 1$ and on a tangent plane centered at 0°W, 15°N, $CD/AB \approx 0.87$ (the latter is obtained by writing parametric equations for the projections of the box's sides and computing their length using standard methods). The foreshortening factors on the tangent plane are about the same for all four sides and are about 0.99. We thus believe that by using tangent plane projection in this particular case we make about 1% error due to the projection effect, as opposed to about 15% error in a cylindrical projection (given for CD/AB; the ratio AB/BC would differ depending on the particular type of the cylindrical projection).

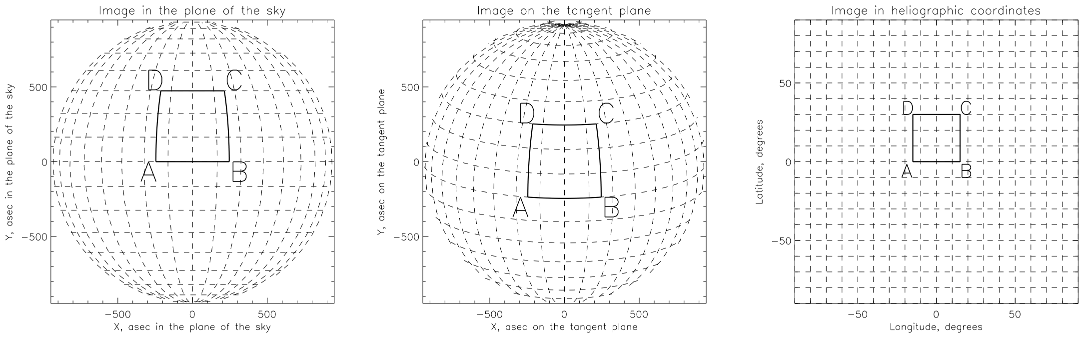

Figure 57. Illustration of heliocentric-cartesian (orthographic) and heliographic projections. $ABCD$ is a $30° \times 30°$ "square", centered at 0°W, 15°N (roughly the size and position of ARs 9002 and 9004 when they pass through the central meridian) in three different projections. *(Left)* – in the plane of the sky (orthographic projection, centered at 0°W, 0°N and neglecting the b-angle for illustrative purposes), *(middle)* – in the tangent plane (orthographic projection, centered in the middle of $ABCD$, i.e., 0°W, 15°N), *(right)* – in heliographic coordinates (plate Carrée projection). Dashed lines are lines of constant latitude and longitude.

REFERENCES CITED

[Alissandrakis, 1981] Alissandrakis, C. E. (1981). A&A 100, 197–200.

[Altschuler & Newkirk, 1969] Altschuler, M. D. & Newkirk, G. (1969). Solar Phys. 9, 131–149.

[Aly, 1992] Aly, J. J. (1992). Solar Phys. 138, 133–162.

[Aschwanden, 2006] Aschwanden, M. (2006). Physics of The Solar Corona, An Introduction with Problems and Solutions. Springer.

[Aschwanden et al., 2008] Aschwanden, M. J., Lee, J. K., Gary, G. A., Smith, M. & Inhester, B. (2008). Solar Phys. 248, 359–377.

[Baty, 2001] Baty, H. (2001). A&A 367, 321–325.

[Berger, 1984] Berger, M. A. (1984). Geophys. Astrophys. Fluid Dynamics 30, 79–104.

[Berger & Field, 1984] Berger, M. A. & Field, G. B. (1984). JFM 147, 133–148.

[Bernstein et al., 1958] Bernstein, I. B., Frieman, E. A., Kruskal, M. D. & Kulsrud, R. M. (1958). Proc. Roy. Soc. Lond. A244, 17–40.

[Brown et al., 2003] Brown, D. S., Nightingale, R. W., Alexander, D., Schrijver, C. J., Metcalf, T. R., Shine, R. A., Title, A. M. & Wolfson, C. J. (2003). Solar Phys. 216, 79–108.

[Burnette et al., 2004] Burnette, A. B., Canfield, R. C. & Pevtsov, A. A. (2004). ApJ 606, 565–570.

[Canfield et al., 1999] Canfield, R. C., Hudson, H. S. & McKenzie, D. E. (1999). GRL 26, 627.

[Canfield et al., 2000] Canfield, R. C., Hudson, H. S. & Pevtsov, A. A. (2000). IEEE Transactions on Plasma Science 28, 1786–1794.

[Chae, 2001] Chae, J. (2001). ApJ 560, L95–L98.

[Chiu & Hilton, 1977] Chiu, Y. T. & Hilton, H. H. (1977). ApJ 212, 873–885.

[Choudhuri, 1998] Choudhuri, A. R. (1998). The physics of fluids and plasmas: an introduction for astrophysicists.

[Démoulin, 2007] Démoulin, P. (2007). Advances in Space Research 39, 1674–1693.

[Démoulin & Berger, 2003] Démoulin, P. & Berger, M. A. (2003). Solar Phys. 215, 203–215.

[Demoulin et al., 1997] Demoulin, P., Henoux, J. C., Mandrini, C. H. & Priest, E. R. (1997). Solar Phys. 174, 73–89.

[DeRosa et al., 2009] DeRosa, M. L., Schrijver, C. J., Barnes, G., Leka, K. D., Lites, B. W., Aschwanden, M. J., Amari, T., Canou, A., McTiernan, J. M., Régnier, S., Thalmann, J. K., Valori, G., Wheatland, M. S., Wiegelmann, T., Cheung, M. C. M., Conlon, P. A., Fuhrmann, M., Inhester, B. & Tadesse, T. (2009). ApJ 696, 1780–1791.

[DeVore, 2000] DeVore, C. R. (2000). ApJ 539, 944–953.

[Fan & Gibson, 2003] Fan, Y. & Gibson, S. E. (2003). ApJ 589, L105–L108.

[Fan & Gibson, 2004] Fan, Y. & Gibson, S. E. (2004). ApJ 609, 1123–1133.

[Finn & Antonsen, 1985] Finn, J. & Antonsen, Jr., T. M. (1985). Comments Plasma Phys. Controlled Fusion 9, 111–126.

[Frederick Pearson, 1990] Frederick Pearson, I. (1990). Map Projections: Theory and Applications. CRC Press.

[Gallagher et al., 2002] Gallagher, P. T., Moon, Y. & Wang, H. (2002). Solar Phys. 209, 171–183.

[Gary, 2001] Gary, G. A. (2001). Solar Phys. 203, 71–86.

[Gibson & Fan, 2008] Gibson, S. E. & Fan, Y. (2008). Journal of Geophysical Research (Space Physics) 113, 9103–+.

[Gold & Hoyle, 1960] Gold, T. & Hoyle, F. (1960). MNRAS 120, 89–105.

[Golub et al., 2007] Golub, L., Deluca, E., Austin, G., Bookbinder, J., Caldwell, D., Cheimets, P., Cirtain, J., Cosmo, M., Reid, P., Sette, A., Weber, M., Sakao, T., Kano, R., Shibasaki, K., Hara, H., Tsuneta, S., Kumagai, K., Tamura, T., Shimojo, M., McCracken, J., Carpenter, J., Haight, H., Siler, R., Wright, E., Tucker, J., Rutledge, H., Barbera, M., Peres, G. & Varisco, S. (2007). Solar Phys. 243, 63–86.

[Green et al., 2002] Green, L. M., López Fuentes, M. C., Mandrini, C. H., Démoulin, P., Van Driel-Gesztelyi, L. & Culhane, J. L. (2002). Solar Phys. 208, 43–68.

[Handy et al., 1999] Handy, B. N., Acton, L. W., Kankelborg, C. C., Wolfson, C. J., Akin, D. J., Bruner, M. E., Caravalho, R., Catura, R. C., Chevalier, R., Duncan, D. W., Edwards, C. G., Feinstein, C. N., Freeland, S. L., Friedlaender, F. M., Hoffmann, C. H., Hurlburt, N. E., Jurcevich, B. K., Katz, N. L., Kelly, G. A., Lemen, J. R., Levay, M., Lindgren, R. W., Mathur, D. P., Meyer, S. B., Morrison, S. J., Morrison, M. D., Nightingale, R. W., Pope, T. P., Rehse, R. A., Schrijver, C. J., Shine, R. A., Shing, L., Strong, K. T., Tarbell, T. D., Title, A. M., Torgerson, D. D., Golub, L., Bookbinder, J. A., Caldwell, D., Cheimets, P. N., Davis, W. N., Deluca, E. E., McMullen, R. A., Warren, H. P., Amato, D., Fisher, R., Maldonado, H. & Parkinson, C. (1999). Solar Phys. 187, 229–260.

[Hood & Priest, 1979] Hood, A. W. & Priest, E. R. (1979). Solar Phys. 64, 303–321.

[Hood & Priest, 1981] Hood, A. W. & Priest, E. R. (1981). Geophys. Astrophys. Fluid Dynamics 17, 297.

[Ireland et al., 1992] Ireland, R. C., van der Linden, R. A. M., Hood, A. W. & Goossens, M. (1992). Solar Phys. 142, 265–289.

[Jackson, 1975] Jackson, J. D. (1975). Classical Electrodynamics. Wiley, New York.

[Ji et al., 2003] Ji, H., Wang, H., Schmahl, E. J., Moon, Y. & Jiang, Y. (2003). ApJ 595, L135–L138.

[Kano et al., 2008] Kano, R., Sakao, T., Hara, H., Tsuneta, S., Matsuzaki, K., Kumagai, K., Shimojo, M., Minesugi, K., Shibasaki, K., Deluca, E. E., Golub, L., Bookbinder, J., Caldwell, D., Cheimets, P., Cirtain, J., Dennis, E., Kent, T. & Weber, M. (2008). Solar Phys. 249, 263–279.

[Klimchuk, 2009] Klimchuk, J. A. (2009). ArXiv e-prints .

[Kosugi et al., 2007] Kosugi, T., Matsuzaki, K., Sakao, T., Shimizu, T., Sone, Y., Tachikawa, S., Hashimoto, T., Minesugi, K., Ohnishi, A., Yamada, T., Tsuneta, S., Hara, H., Ichimoto, K., Suematsu, Y., Shimojo, M., Watanabe, T., Shimada, S., Davis, J. M., Hill, L. D., Owens, J. K., Title, A. M., Culhane, J. L., Harra, L. K., Doschek, G. A. & Golub, L. (2007). Solar Phys. 243, 3–17.

[Kusano et al., 2003] Kusano, K., Yokoyama, T., Maeshiro, T. & Sakurai, T. (2003). Advances in Space Research 32, 1931–1936.

[LeVeque, 1955] LeVeque, R. J. (1955). Finite Difference Methods for Ordinary and Partial Differential Equations, Steady-State and Time-Dependent Problems. SIAM.

[Lim et al., 2007] Lim, E.-K., Hyewon, J., Chae, J. & Moon, Y.-J. (2007). ApJ 656, 1167–1172.

[Linton & Antiochos, 2002] Linton, M. G. & Antiochos, S. K. (2002). ApJ 581, 703–717.

[Longcope & Malanushenko, 2008] Longcope, D. W. & Malanushenko, A. (2008). ApJ 674, 1130–1143.

[Longcope et al., 2007] Longcope, D. W., Ravindra, B. & Barnes, G. (2007). ApJ 668, 571–585.

[Lopez Fuentes et al., 2006] Lopez Fuentes, M. C., Klimchuk, J. A. & Demoulin, P. (2006). ApJ 639, 459–474.

[Lothian & Browning, 1995] Lothian, R. M. & Browning, P. K. (1995). Solar Phys. 161, 289–316.

[Low & Lou, 1990] Low, B. & Lou, Y. (1990). ApJ 352, 343–352.

[Low, 1994] Low, B. C. (1994). Physics of Plasmas 1, 1684–1690.

[Malanushenko et al., 2009a] Malanushenko, A., Longcope, D. W., Fan, Y. & Gibson, S. E. (2009a). ApJ 702, 580–592.

[Malanushenko et al., 2009b] Malanushenko, A., Longcope, D. W. & McKenzie, D. E. (2009b). ApJ 707, 1044–1063.

[Mandrini et al., 2004] Mandrini, C. H., Démoulin, P., van Driel-Gesztelyi, L., van Driel-Gesztelyi, L., van Driel-Gesztelyi, L., van Driel-Gesztelyi, L. L. M. & López Fuentes, M. C. (2004). Ap&SS 290, 319–344.

[McKenzie & Canfield, 2008] McKenzie, D. E. & Canfield, R. C. (2008). A&A 481, L65–L68.

[Metcalf et al., 2008] Metcalf, T. R., De Rosa, M. L., Schrijver, C. J., Barnes, G., van Ballegooijen, A. A., Wiegelmann, T., Wheatland, M. S., Valori, G. & McTtiernan, J. M. (2008). Solar Phys. 247, 269–299.

[Moffatt & Ricca, 1992] Moffatt, H. K. & Ricca, R. L. (1992). Proc. Roy Soc. Lond. A 439, 411–429.

[Nakagawa & Raadu, 1972] Nakagawa, Y. & Raadu, M. A. (1972). Solar Phys. 25, 127–135.

[Nakagawa et al., 1971] Nakagawa, Y., Raadu, M. A., Billings, D. E. & McNamara, D. (1971). Solar Phys. 19, 72–85.

[Newcomb, 1960] Newcomb, W. A. (1960). Ann. Phys. 10, 232–267.

[Perot, 2000] Perot, B. (2000). Journal of Computational Physics 159, 58–89.

[Pevtsov et al., 2003] Pevtsov, A. A., Maleev, V. & Longcope, D. W. (2003). ApJ 593, 1217–1225.

[Prautzsch et al., 2002] Prautzsch, H., Boehm, W. & Paluszny, M. (2002). Bezier and B-Spline Techniques. Springer.

[Press et al., 1986] Press, W. H., Flannery, B. P., Teukolsky, S. A. & Vetterling, W. T. (1986). Numerical Recipes: The art of scientific computing. Cambridge University Press, Cambridge.

[Priest & Forbes, 2000] Priest, E. & Forbes, T. (2000). Magnetic Reconnection. "Cambridge University Press".

[Rachmeler et al., 2009] Rachmeler, L. A., DeForest, C. E. & Kankelborg, C. C. (2009). ApJ 693, 1431–1436.

[Régnier et al., 2005] Régnier, S., Amari, T. & Canfield, R. C. (2005). A&A 442, 345–349.

[Rosner et al., 1978] Rosner, R., Tucker, W. H. & Vaiana, G. S. (1978). ApJ 220, 643–655.

[Rust, 2003] Rust, D. M. (2003). Advances in Space Research 32, 1895–1903.

[Rust & LaBonte, 2005] Rust, D. M. & LaBonte, B. J. (2005). ApJ 622, L69–L72.

[Scherrer et al., 1995] Scherrer, P. H., Bogart, R. S., Bush, R. I., Hoeksema, J. T., Kosovichev, A. G., Schou, J., Rosenberg, W., Springer, L., Tarbell, T. D., Title, A., Wolfson, C. J., Zayer, I. & MDI Engineering Team (1995). Solar Phys. 162, 129–188.

[Schrijver et al., 2008] Schrijver, C. J., DeRosa, M. L., Metcalf, T., Barnes, G., Lites, B., Tarbell, T., McTiernan, J., Valori, G., Wiegelmann, T., Wheatland, M. S., Amari, T., Aulanier, G., Démoulin, P., Fuhrmann, M., Kusano, K., Régnier, S. & Thalmann, J. K. (2008). ApJ 675, 1637–1644.

[Taylor, 1974] Taylor, J. B. (1974). Phys. Rev. Lett. 33, 1139–1141.

[Thompson, 2006] Thompson, W. T. (2006). A&A 449, 791–803.

[Török & Kliem, 2004] Török, T. & Kliem, B. (2004). In SOHO 15 Coronal Heating, (R. W. Walsh, J. Ireland, D. Danesy, & B. Fleck, ed.), vol. 575, of ESA Special Publication pp. 56–+,.

[Török et al., 2004] Török, T., Kliem, B. & Titov, V. S. (2004). A&A 413, L27–L30.

[van Ballegooijen, 2004] van Ballegooijen, A. A. (2004). ApJ 612, 519–529.

[Welsch et al., 2009] Welsch, B. T., Li, Y., Schuck, P. W. & Fisher, G. H. (2009). ApJ 705, 821–843.

[Woltjer, 1958] Woltjer, L. (1958). Proc. Nat. Acad. Sci. 44, 489–491.

[Yan et al., 2008] Yan, X., Qu, Z. & Kong, D. (2008). MNRAS 391, 1887–1892.

[Zhang et al., 2006] Zhang, M., Flyer, N. & Low, B. C. (2006). ApJ 644, 575–586.